RICE UNIVERSITY

Nanotribological and Nanomechanical Investigation of Nanomaterials

by

Jiangnan Zhang

A THESIS SUBMITTED
IN PARTIAL FULFILLMENT OF THE
REQUIREMENTS FOR THE DEGREE

Doctor of Philosophy

APPROVED, THESIS COMMITTEE

Dr. Jun Lou, Chair
Associate Professor of Mechanical
Engineering and Materials Science

Dr. Pulickel M. Ajayan
Benjamin M. and Mary Greenwood
Anderson Professor in Engineering
Materials Science and Nanotechnology

Dr. Qilin Li
Associate Professor of Civil and
Environmental Engineering

HOUSTON, TEXAS
2012

Success is not final, failure is not fatal. It is the courage to continue that counts.

-Winston Churchill

ABSTRACT

Nanotribological and Nanomechanical Investigation of Nanomaterials

by

Jiangnan Zhang

This dissertation primarily documents the quantification of the interfacial behavior of carbon based nanomaterials, which includes two categories, one is the nanofriction properties evaluation of aligned carbon nanotubes (CNTs) carpets, few-layer graphene as well as three types of functionalized graphene nanoribbons, the second is the mechanical characterization of individual functionalized carbon nanofibers (CNFs) and the interfacial fracture toughness quantification in CNTs/polymer derived ceramics nanocomposite. The aligned CNTs carpets have a highly anisotropic friction behavior, which means the friction force are lower for transversely aligned CNTs side than for vertically aligned CNTs surface. We can also tune the friction properties of graphene nanoribbons by grafting different functional groups. In addition, two narrow angular regions with high friction, separated by a wide angular interval with low friction, were identified between graphene and highly oriented pyrolytic graphite. The distance between the two friction peaks is 61◦, which corresponds well with the 60◦ symmetry of individual atomic layers in the graphite lattice. The technique that involves the usage of mcirodevices and nanoidenter was used to conduct tensile tests on pristine, fluorinated and amino-functionalized CNFs, which were found to exhibit varied load-bearing abilities and unique fracture modes. The technique was also used to perform single fiber pullout experiments to study CNTs/polymer derived ceramic interface.

Acknowledgments

I would like to extend my heartfelt thanks to my advisor, Professor Jun Lou. He has been the best teacher and role model I could hope for and someone who I felt always cared about my development as an academic. I will look back on my time as his student with great fondness and appreciation for many years to come. It is truly a privilege I can have him as my advisor and his mentoring will be a lifelong fortune for me.

I would also like to thank the other members, Prof. Pulickel M. Ajayan, Prof. Qilin Li, of my thesis committee for reviewing this work, and more importantly, for kindly supporting me over various stages of my study and research at Rice. Their interest and appreciation gave me incredible impetus and confidence to carry on this research.

During the four years at Rice, I have the opportunity to learn from many other distinguished scholars, including Prof. Enrique V. Barrera, Prof. Rex B. McLellan, Dr. Peter Loos, Dr. Robert Vajtai, Dr. Gang Liang, Dr. Angelo Benedetto and many more. I could not list them all, but I thank them all.

In addition, I feel very lucky to have the opportunity to collaborate with Dr. Valery Khabashesku at Department of Chemical and Biomolecular Engineering, University of Houston and Dr. Yanfei Gao of Department of Materials Science and Engineering, University of Tennessee, T.T. and W.F. Chao Prof. James Tour at Department of Chemistry, Rice University. Dr. Brain Sheldon of Brown University generously provides novel polymer derived ceramics precursor throughout this work. I benefit tremendously from their rich experience and unique insight and their help on my research is sincerely appreciated.

During the past four years, I would like to thank my colleagues in Lou research group, Yogeeswaran Ganesan, Hao Lu, Yang Lu, Yongjie Zhan, Zheng Liu, Cheng Peng, Pei Dong, Phillip E. Loya, Sina Najmaei, Jing Zhang, Peng Zhang and more, for your generous help in many ways. They assisted and collaborated with me in various aspects and there was so much fun to stay in the lab days and nights because of them.

Last but certainly not least, it is my family who has always been there for me with unconditional love and support. This dissertation is dedicated to them. My deepest acknowledgement goes to my wife, Nan Zhang. Her love and support through all the emotional ups and downs of the PhD has been unflagging. To my parents, I simply could not owe more. They bring me to the world and make me who I am. I am proud of them as they are proud of me, or maybe more.

Contents

List of Figures

List of Tables

List of Equations

Chapter 1

1. Introduction

1.1. Nanomaterials

Nanomaterials are of special interests to the materials-research community over the past couple of decades, due to their potential applications in catalysts[1-4], biomedicines[5, 6], and electronics[7, 8]. Probably unbeknownst to us, nanomaterials have become part of our everyday lives. For example, nanoparticles of metal oxide have been used in sun lotions to block ultraviolet lights and nanomaterial thin films have been applied in the central processing unit (CPU) of our computers[9], which have brought about real technological revolutions.

The research of nanomaterials concentrates on the creation and exploitation of materials which have morphological characteristics from atoms to bulk material and with at least one dimension in the nanoscale range. Figure 1.1 shows the typical ranges of some materials. Nanomaterials are not a simple extension of miniaturization from microscale down to nanoscale. Microscale materials mostly exhibit the same physical

properties as bulk materials. However, properties of nanomaterials are significantly different from those of bulk materials, such as the lower melting point, the enhanced mechanical strength, and the shift of absorption spectrum.

Therefore, the research on nanomaterials aims to obtain an in depth understanding of the new phenomena of nanomaterials, to further develop novel functional materials and to boost the invention of new devices. To achieve such goals, scientific areas such as physics, chemistry, materials science and biology have been integrated in the course of enquiry.

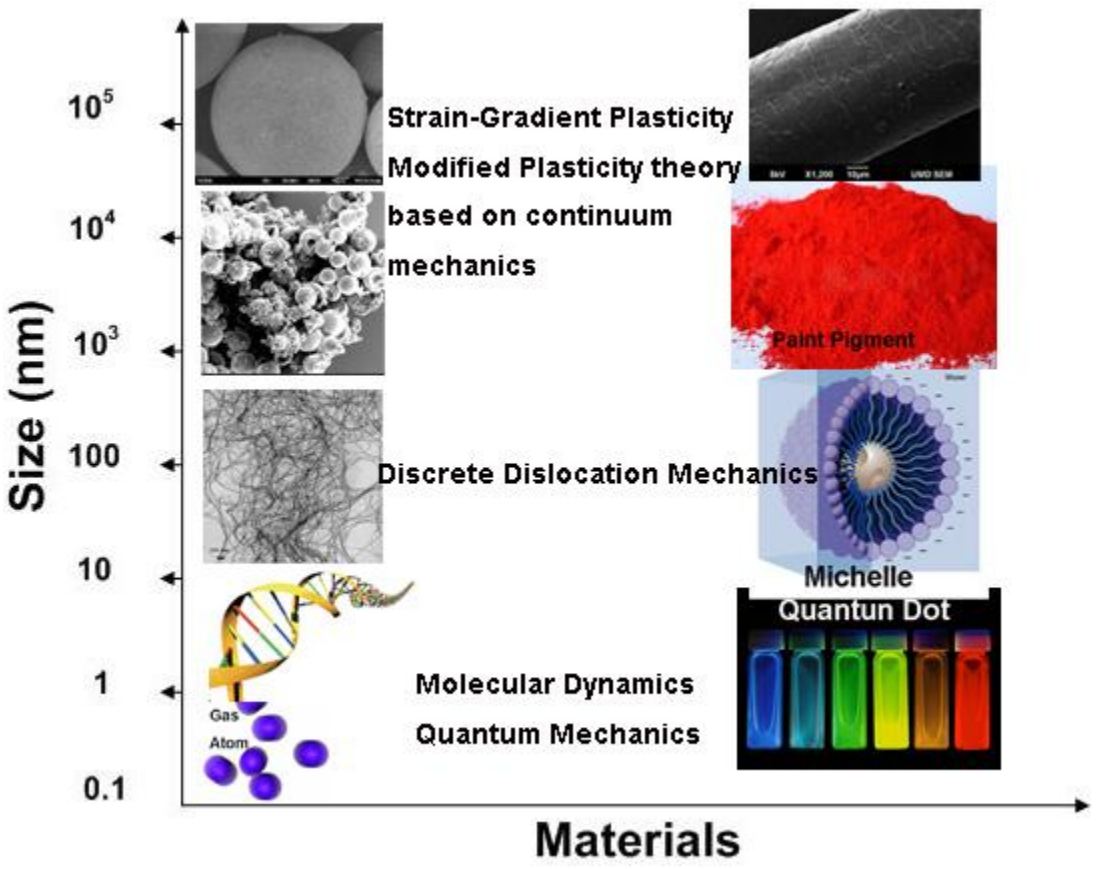

Figure 1.1 Illustration of length-scale effects on the mechanical properties of materials.

A great example of a (quasi) 1-D nanomaterial is a carbon nanotube (CNT), a molecular scale fibrous structure made of carbon atoms (see Figure 1.2). The simplest way to envision the structure of a CNT is to imagine a flat sheet of graphite (graphene) rolled into the form of a hollow cylinder. There are basically two structurally distinct classes. In 1991, S. Iijima of NEC in Japan discovered single walled carbon nanotubes (SWNTs), by adding transition-metal catalysts into carbon in an arc discharge[10]. SWNTs produced by most techniques are nearly uniform in diameter (generally between 0.5 to 2 nm) and have the tendency to self-organize into "rope" held together by van der Waals interaction. The second type of CNTs is multi-walled CNTs (MWNTs), which exhibits a Russian doll-like structure of nested concentric tubes. Their interlayer spacing can range from 0.342 to 0.375 nm, depending on the diameter and number of shells comprising the tube. Due to the excellent physical properties, CNTs and their nanocomposites have attracted more and more research attention in recent years.

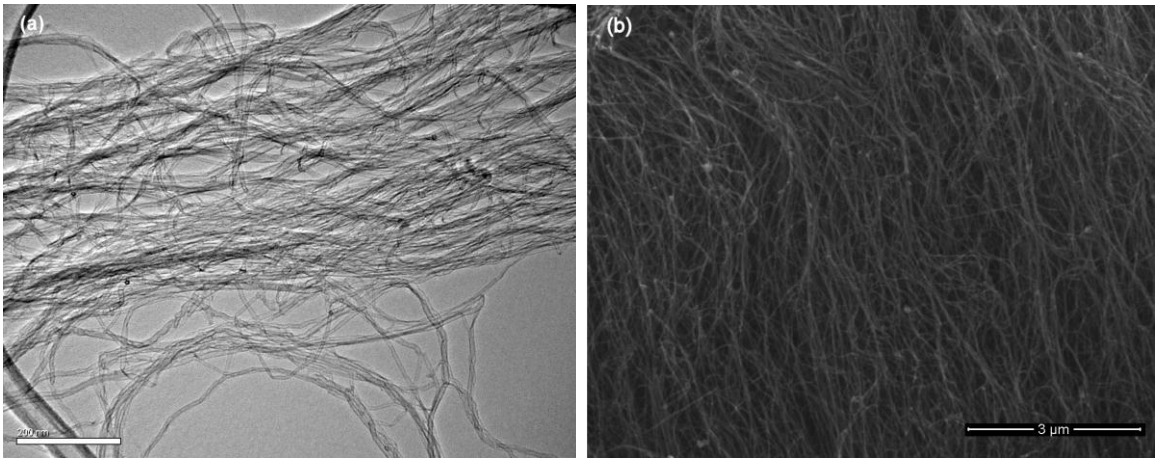

Figure 1.2 (a) TEM image of bundles of MWNTs, (b) SEM image of MWNTs carpet.

Very recently, another promising nanomaterial, graphene has drawn high interests from both academic research and industrial applications (see Figure 1.3). It is the firstly found real 2-D materials which is a monolayer of carbon atoms packed into a hexagonal lattice[11]. The sheet has ultrahigh mechanical strength, conductivity with high electron mobility and optical transparency[12]. These exceptional properties make it promising material for flexible or transparent electronics[13], micro/nano-electromechanical systems (M/NEMS), bio-sensors etc[14]. The most common method of graphene fabrication is the exfoliation which finds its roots with a technique that has been around for centuries-writing with a graphite pencil. Andre Geim's group successfully peeled few atomic layers of graphene; by gently rubbing or pressing a freshly cleaved graphite crystal on an oxidized silicon wafer graphene flakes with the correct thickness of oxide[11]. This technique simplifies the process of finding single graphene sheets but obviously limits this fabrication scheme to devices for research purposes. Several other attempts to improve the quality and yield of exfoliation technique have been employed. These include stamping methods which use silicon pillars to transfer graphene flakes[15] and electrostatic voltage assisted exfoliation which use electrostatic forces to controllably separate graphene from bulk crystals[16]. The technique which currently seems to have the greatest potential for mass production is the direct growth of graphene. Typically this is accomplished by heating a SiC wafer which results in the partial graphitization of the upper layer. Chemical vapor deposition (CVD)[17] and molecular beam epitaxy (MBE)[18] are two other potential routes to graphene growth. However, wide spread applicability of graphene is limited by the crude and time consuming methods currently used to fabricate and isolate single graphene sheets.

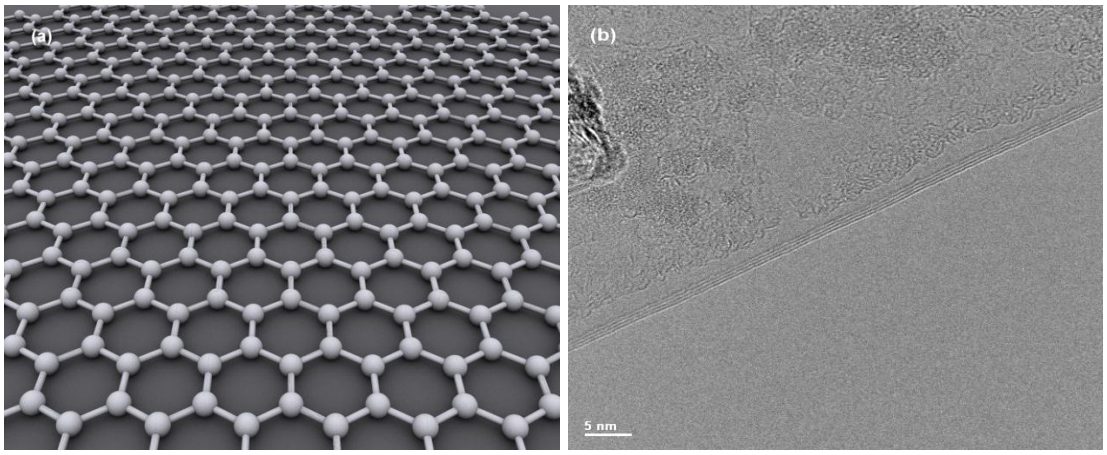

Figure 1.3 (a) Atomic-scale honeycomb lattice of graphene structure, (b) Transmission electron microscope image of few layer graphene.

1.2. Interfacial Characteristics of Nanomaterials

Due to the small size, the surface area of the nanomaterials is much larger than that of bulk materials, leading to a large fraction of surface atoms, large surface energy and reduced imperfections. Moreover, the nanoparticles can be assembled into various nanostructures and microstructures. These features give unique electrical, chemical, optical, and mechanical properties to nanomaterials, which would inspire the creation and fabrication of new devices and the invention of new technologies. For instance, nanomaterials have a significantly lower melting point than bulk materials, due to a large fraction of surface atoms in the total amount of atoms. The melting point of bulk silver is as high as 1234 K[19], however, it decreases rapidly to only 375 K for silver nanoparticles with sizes below 5 nm. Because silver nanoparticles can be annealed under 373 K to form silver wires, the silver nanoparticle dispersion can be used to print circuits onto plastics, films and textiles[20].

It is significant that compression and tensile testing of nanomaterials revealed different values of their strength and, in particular, ductility. The study of hardness, fracture stress and ductility of warm-compacted nanocrystalline iron powder compacts of a near theoretical density revealed that the values of hardness increased and those of fracture stress and elongation to failure decreased significantly with decreasing the grain size in the range from 33 to 8 nm[20]. This is connected with the dramatic effect of processing defects such as flaws, micropores, etc., on the tensile values of strength. The presence of processing defects was confirmed by the scanning electron microscope (SEM) examination. Hence there are many reasons for masking size effects in nanomaterials. The processing history has a critical effect on the structure of interfaces in these subjects and the detail characterization by several independent methods is very important. The different features of the grain size determination by the X-ray diffraction and transmission electron microscope (TEM) examination as applied to nanostructured Pd samples have been discussed in detail by Krill and Birringer[21]. The presence of impurities in nanomaterials and their possible segregation on the grain boundaries may also change the properties with reduction of the grain size. Especially as that, from general consideration and some calculations, the segregation effect must be intensified within the nanometer interval.

Some of the most important properties of materials in high-technology applications are strongly influenced or even controlled by the presence of the interfaces. For example, interfaces are the critical element in fiber-reinforced structural ceramics with mechanical properties not imagined a decade or two ago. Besides, the entire electronics industry is based on the fascinating electrical properties of semiconductor

interfaces, with ceramic-semiconductor, metal-semiconductor and metal-ceramic interfaces playing critical roles as well. Further examples are surface-modification techniques, designed to enhance the corrosion resistance of materials in hostile environments, or tailed for tribological or catalytic applications. In contrast to their enormous technological importance, our basic understanding of even the simplest interfaces is rudimentary at best. It is increasingly recognized, however, that truly significant technological advances can come from a better understanding and control of interfacial processes.

The interfacial phenomena between different phases with a planned structure and planned properties have become extremely important in recent years. This has provided opportunities to produce interfaces with promising surface structures and properties on various solid interfaces. Whenever different solid surfaces are brought into contact adhesion can occur at the solid interface; the different solid surfaces include the CNFs/CNTs reinforced composites, laminated plastics, coatings, and compounded and reinforced rubbers.

1.2.1. Friction

1.2.1.1. Introduction to Friction Study

Friction is defined as the resistance to motion. The fundamental comprehension of this phenomenon remains intriguingly incomplete, though seemingly simple and considered to be one of the oldest scientific subjects in human history. Friction inflicts an irretrievable loss of energy and a seriously reduction of the efficiency of the conversion and consumption of human's energy resources. The recognition that understanding and

controlling friction, lubrication and wear is very urgent and thus forms a highly relevant area of fundamental and application-oriented research has been achieved in view of the increasing need for energy and the decreasing resources of available energy.

Nanotribology involves adhesion, friction, wear, and lubrication phenomenon study. The Greek verb τριβος means 'to rub' and hence the term represents the study of rubbing. The pioneering documented research was traced back to five centuries ago, carried out by Leonardo da Vinci. However, until the 17th century when a French scientist, Guillaume Amontons, initially unveiled Leonardo's insights and generalized two basic, empirical laws of sliding friction, namely that (a) friction is proportional to the applied normal force and (b) friction is independent of the contact area of the sliding surfaces. A century later, Charles Augustin de Coulomb introduced the third empirical law, namely that the friction force is independent of the sliding velocity, once sliding has started. Together, these three 'laws' are known as the Da-Vinci-Amontons-Coulomb, or the Amontons-Coulomb laws of sliding friction.

The second friction law implies that the contact area should be of primary importance while friction is brought about by the interaction between surfaces. The reason lies in that friction is generated at the contacts between micro asperities of the two sliding surfaces; in fact, friction does depend on the real area of contact, but not on the apparent contact area of the sliding surfaces. As we will see later in this dissertation, experiments with atomically smooth graphene surfaces that can exhibit substantial friction have shown that the interlocking of micro-asperities is not a necessary element of the energy dissipation mechanism.

A more defined instrumentation with sensitivity for distances and forces down to the atomic scale has pushed the progress in this research field to a higher level. With the introduction of such techniques, only a few decades ago, the focus has shifted from large, multi-asperity contacts to the forces generated by individual, micron- and submicron sized asperities. One example of the more complex instrumentation with high precision for force measurements is the Surface Forces Apparatus (SFA), an ingenious instrument developed by Tabor and Winterton in 1968 enabled the detailed study of atomically smooth (mica) surfaces in contact[22]. This instrument is very popular for the study of the behavior of molecularly thin liquid films. Additionally, a very recent technique, based on the quartz crystal microbalance (QCM), permits sliding friction processes to studied at the angstrom level and at time scales in the nanosecond range. Krim *et al*. have employed this technique to quantify the behavior of smooth monolayers of molecules sliding over the surface on which they are adsorbed[23]. Though the field of nanoscale friction and lubrication was developing at that time, the term nanotribology was first used by Krim, in a publication that appeared in 1991[23].

Although the SFA and the QCM are accurate enough to measure forces down to the scale of atomic friction, they suffer from the limitation of comparatively large areas of contact, typically of several square micrometers and more. The need of comparatively small contact area led to the development, in the mid-1980, of the Atomic Force Microscope (AFM) by Binning, Quate, and Gerber that enabled the detection of atomic scale features on a wide range of surfaces. The AFM really allows for nanoscale force measurements, as it naturally limits the contact size to the nanometer regime. Mate and colleagues adapted the AFM to measure lateral forces and they demonstrated the atomic-

scale stick-slip motion of a sharp tungsten tip over a graphite surface. This experiment has initiated a new approach in nanotribology. An atomic force microscope used for measuring lateral forces is now referred to as a Lateral or Friction Force Microscope (FFM).

1.2.1.2. Friction at nanoscale

The understanding of friction at nanoscale is a current important problem from both a fundamental and a technological perspective in wide ranges of length and time scales. On the one hand the understanding of friction at nanoscale is fundamental for the manipulation of nanoparticles and the miniaturization of moving devices as NEMS, for instance. On the other hand friction is complex nonlinear phenomenon of fundamental interest in many scientific areas. The development of new experimental techniques such as the force friction microscope and the surface force apparatus, experimental and theoretical studies of friction at the atomic scale has received a significant attention.

Two categories of theories were proposed in order to explain the friction phenomenon at the small scales. The first one is based on continuum contact mechanics theories such as classic Hertz's theory, Johnson-Kendall-Roberts (JKR), Derjagin-Muller-Toropov (DMT) models, which relate friction with normal load through constant shear strength and a varying contact surface area with respect to the normal load[24-27]. The other category was based on Tomlinson's model[28], which assumes atomically flat contacting surfaces and has a fluctuating potential field related to the arrangement of surface atoms.

The Hertz theory to predict the deformed profile of two spheres in contact is shown in Figure 1.4 where the arrows indicate the applied compressive load *P*. This theory has shown great success to accurately describe the contact between elastic bodies in the absence of adhesion. However, JKR theory predicts the relationship between contact area and normal load for relatively compliant materials and strong adhesive forces where DMT theory works for relatively stiff materials and weak adhesive forces.

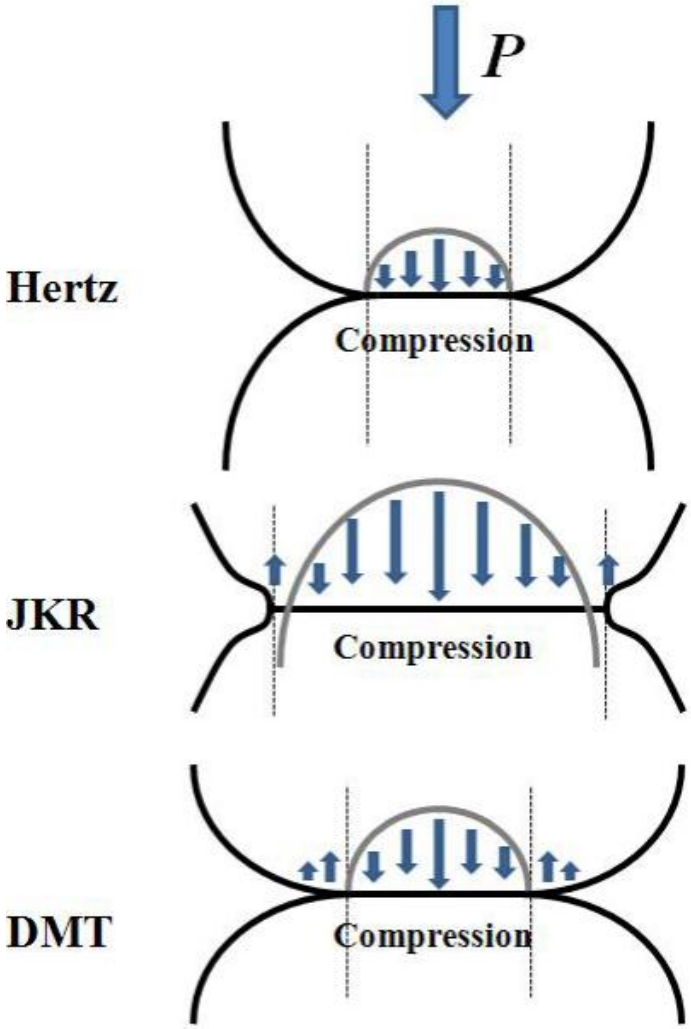

Figure 1.4 Comparison of different friction models. Normal load *P* is applied to compress two spheres.

Friction has been proposed to be a phenomenon caused only by the surfaces of the sliding bodies. The proposal by Zhong *et al* was that the friction is related to the bonding energy between the surfaces, so that the friction coefficient is related to the adsorption energy of the sliding surfaces on each other[29]. The authors showed that if a monolayer of Pd atoms slides over a graphite lattice, the coefficient of friction is very low because the adsorption energy of Pd on graphite is low. This theory neglects all effects of the atomic layers underlying the sliding surfaces.

To investigate the force of adhesion between a surface and a nano-asperity, atomic force microscopes are widely used. But it is extremely difficult to identify the precise contact area, especially in this case when the tip snaps away from the surface. This makes it difficult to quantify the relation between the contact area of the nano-asperity and friction at the nanoscale. Another selection is to employ different sized nanoclustered materials deposited on a well-defined surface and drag them along the surface with an AFM tip. Nanoclusters of different sizes on the surface provide different areas of contact, which can be used to quantify the area-dependence of friction. Quantified frictional properties of antimony nanoparticles grown on highly oriented pyrolytic graphite (HOPG) and pushed with the tip of an AFM have been described recently. These experiments indicate the linear dependence of friction force on the contact area and the main feature found is that islands with area less than 10^4 nm^2 are much easier to move than the ones with larger contact areas. In fact, it was not long before that the origin of lubrication of graphite was revealed, which involves the atomic-scale geometrical details of the contacting surfaces.

The interfacial behavior of carbon based nanomaterials, especially friction and adhesion, has been dramatically investigated before. Hirano *et al.* predicted that friction would vanish when two contacting surfaces are laterally stiff and incommensurate[30]. Socoliuc *et al*. showed that friction could be reduced dramatically at nanoscale by introducing a small vibrating force to the interface[31]. Additionally, Hirata and Yoshioka studied sliding friction properties of microwave-plasma-enhanced chemical vapor deposition (MPCVD) deposited CNTs on different substrates by means of steel ball-on-disk type of testing[32]. Based on friction coefficient measurements, they found that friction force was reduced when CNTs had less defects and higher crystallinity, and also when tests were conducted in vacuum. Tu *et al*. used both atomic force microscope (AFM) and a ball-on-disk tribometer for friction study of carbon nanotubes embedded in anodic aluminum oxide template[33]. They found a linear relationship between friction force and normal load in their nanoscale AFM based tests, and a decrease of friction coefficient with increasing sliding velocity from 0.04 m/s to 0.16 m/s in their ball-on-disk based tests.

1.2.2. Mechanics at small scales

As materials become smaller and smaller, the surface-to-volume ratio increases significantly, the mechanical performance changes dramatically. For instance, when a thin film's dimensions begin to approach that of its microstructural features, mechanical properties such as plasticity, fracture toughness and fatigue resistance begin to exhibit size effects. The strength of materials with pre-existing dislocations can be increased by reducing systems' characteristic length scales. For carbon based nanomaterials such as CNFs/CNTs, graphene, dislocations also play an important role in the relaxation and

intramolecular plasticity[34]. Specifically, the formation of 5-7 Stone-Wales (SW) defects which depends upon strain, symmetry, time and temperature greatly effect CNTs relaxation under tension. Elastic properties are dependent on the nature of bonding and only exhibit size effects at the atomic scale. However, as the grain size or structural dimension fall below 50 nm, mechanical behavior control is transitioned from dislocation based mechanisms to surface and intermolecular mechanisms.

CNFs/CNTs have received major attention as composite material fillers due to their immense specific surface area. The high tensile strength of CNFs and CNTs supports polymer matrix strengthening and stiffening assuming good interfacial adhesion and nanofiber alignment. The realization of the traits of nanoscale fillers relies on the specific condition that their interfaces are loaded near their maximum strength, which results in significant energy stored at the interface. The mechanism to release this energy controls the composite toughness, and it is dependent on local parameters, such as the interfacial shear strength, the clamping force that controls frictional nanofiber pull-out, and the matrix yield strength. In this regard, the interface properties of CNFs/CNTs are key in improving interfacial adhesion and load transfer. Over the last two decades, a number of testing methods have developed to assess the interfacial properties between nanofibers and matrices, and the validity of those methods has also been discussed extensively. Micro-mechanical testing methods, including single fiber fragmentation[35], single fiber pull-out[36], micro-bond and micro-indentation tests[37], can provide direct measurement of fiber-matrix interfacial properties.

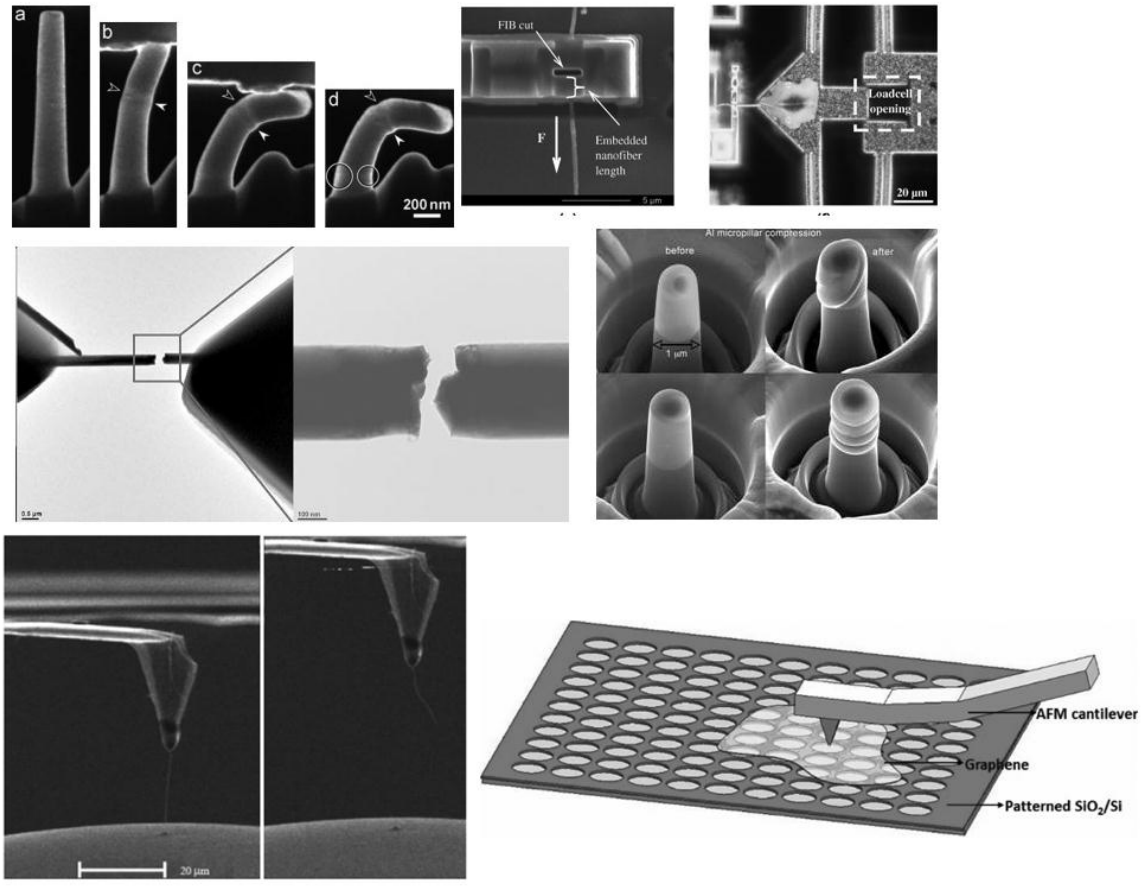

Figure 1.5 Collage shows a few representative in situ mechanical testing techniques that are currently being used by researchers to study the mechanical properties of small scale materials.

1.2.2.1. Mechanical Testing of Individual Carbon Nanotube/Carbon Nanofiber

CNTs/CNFs has a distinct alliance of small size (diameter ranging from approx. 1 to 100 nm and lengths up to several mm), low density, high stiffness, high strength (reported values vary between 30 and 110 GPa for MWNTs and between 13 and 53 GPa for SWNTs) and a broad range of electronic properties from metallic to p- and n-doped semiconducting. The Young's modulus of a CNT has been theoretically estimated to be equal to 0.97 TPa (assuming the interlayer separation of graphite, 0.34 nm, to be equal to

the nanotube's thickness), a value which is in good agreement with the C_{11} elastic constant of graphite. This value has been known to be practically independent of the tube's chirality and diameter (in the range 0.68-27 nm).

The mechanical properties quantification of individual CNTs can be extremely challenging due to their small scale and low magnitude of the forces and deformation involved. The pioneering quantifications of the mechanical properties of CNTs were thus indirect, based on measuring the amplitude of their thermally induced vibration inside a transmission electron microscope. The nanotubes were modeled as stochastically driven resonators and their Young's moduli were estimated from their Gaussian vibrational profiles. From a series of measurements performed as a function of temperature an average Young's modulus value of 1.8 GPa was obtained. A similar method, that involved the direct excitation of MWNTs using an AC electric field, was used subsequently by researchers to calculate the bending modulus. For nanotube diameters below 10 nm, a typical bending modulus value of 1 TPa was obtained, a value which reduced to 100 GPa for thicker tubes. Lateral and vertical bending of MWNTs, using an AFM prober to apply a known force, has also been employed in the past to investigate CNTs. The first quantitative measurement of Young's modulus of MWNTs using an AFM-based set-up was reported by Wong et al. MWNTs were randomly dispersed on MoS2 single crystal and pinned on one side to this substrate by deposition of an array of square pads. Nanotubes were deformed laterally by an AFM tip and lateral force-distance curves were acquired, which were in turn used to deduce the mean value for MWNT Young's modulus. Salvetat *et al*. measured Young's modulus of isolated SWNTs, SWNT ropes and MWNTs produced using different methods as well as the shear modulus of

SWNT ropes. Their technique involved measuring the vertical deflection of CNTs bridging holes on an anodized alumina template. Young's modulus of the order of 1 TPa for both isolated SWNTs and MWNTs (arc discharge grown) were reported, and no dependence of the mechanical response on the tube diameter was observed. However, they did observe that the mechanical properties of CNTs were dictated by the synthesis technique i.e. the extent of the degradation of the graphitic structure brought about by the introduction of defects during production.

The initial measurement of the mechanical properties of CNTs via tensile testing relied on the application of axial strain using an AFM tip within a SEM chamber. One end of each nanotube was attached to a rigid AFM cantilever, driven using a linear piezo-motor. The other end was attached to a compliant cantilever which acted as the load sensor. The technique was used to successfully test 7 MWNT specimens and their stress vs. strain curves were used to estimate MWNT Young's moduli (value ranging from 270 to 950 GPa were found). Examination of broken tubes revealed that nanotubes fractured via a 'sword-in-sheath' mechanism, wherein only the outer layer was found to be load-bearing. Also, an average bending strength of 14 GPa and axial strength values up to 63 GPa were observed for the arc discharge grown MWNTs. The authors were also able to measure the tensile properties of SWNT bundles using the same method they used for MWNTs study. They observed Young's moduli in the range 0.32-1.47 TPa and strength between 10 and 52 GPa. Failure was found to occur only for the nanotubes on the perimeter of the bundle with the rest of the tubes simply slipping apart.

A more recent work described tensile testing of individual MWNTs within a transmission electron microscope using a MEMS material testing system. The usage of

the MEMS device allowed the accurate measurement of both load and displacement simultaneously with TEM imaging. Load was applied using a thermal actuator on one side of the mobile testing stage, and displacement was measured using a MEMS differential capacitive sensor on the opposite end. The experimental measurement of single shell failure in multiwalled carbon nanotubes displayed fracture strength values as high as 100 GPa and fracture strains that are very close to theoretical prediction. Young's Modulus values close to 1 TPa were reported. Interestingly, the authors also found that electron irradiation-induced crosslinking of multiwalled carbon nanotubes resulted in dramatic increase in sustainable loads.

1.3. Organization of Thesis

In summary, with our AFM platform and micro mechanical device, we are now able to perform *in situ* mechanical tests for carbon based nanomaterials (CNFs/CNTs, graphene nanoribbons, CNTs reinforced nanocomposite), which allows the systematic study on tribological properties, tensile strength, and interfacial fracture strength. The organization of the thesis will be:

In Chapter 2, we will present the anisotropic friction behavior of aligned CNTs carpets and frictional characteristics of various graphene nanoribbons by the AFM platform.

In Chapter 3, we will mainly explore the friction behavior at the atomic level, which includes size dependent, thermally activated atomic friction and the angle dependence friction between graphene and highly ordered pyrolytic graphite (HOPG).

In Chapter 4, we will present the interfacial fracture toughness measurement of CNTs reinforced polymer derived ceramics (PDC) composite.

In Chapter 5, we will show the development and usage of the micro mechanical devices for *in situ* tensile testing of individual functionalized CNFs inside the SEM chamber.

In Chapter 6, we will summarize some of our experiment results and make few conclusions for the whole thesis work. In addition, we will propose some possible future works.

Chapter 2

2.Quantitatively Study of Nanofriction Behavior of Carbon Materials

2.1. Anisotropic Nanofriction Behavior of Aligned Carbon Nanotube Carpet

CNTs that possess many unique properties, such as high tensile and flexural strength, high elastic modulus and high aspect ratio[38], has made them attractive for use in applications where friction is important, such as NEMS system and composite[39].

Only a few theoretical and experimental studies on CNTs friction properties have been reported despite their exciting prospects in nanotribological applications. Ni *et al.* [40]simulated the friction between SWNTs bundles and hydrogen terminated diamond surfaces, and concluded that the responses to the applied shear forces depend on the orientation. Specifically, bundles that were oriented vertically to the sliding surfaces had higher friction coefficients than transversally aligned bundles. The tribological properties

of carbon nanotube arrays were also examined in experiments. Kionshita *et al.* showed very high friction coefficients of 1.0-2.2 for vertically aligned carbon nanotube forests with 6 μm length against gold tips of different radii[41]. Additionally, Dickrell *et al.* found the extremely high friction coefficient (μ=0.795) for vertically aligned CNTs films grown on rigid substrates and the very low friction coefficient (μ=0.090) for CNTs dispersed transversely on the same substrate[42, 43]. Moreover, they demonstrated the strong effects of surface chemistry and temperature on friction behaviors of both vertically and transversely oriented CNTs films. However, they claimed that the frictional anisotropy was insensitive to humidity, a finding with which we disagreed. The friction force in our system was found to be critically influenced by the relative humidity; with decreasing relative humidity the friction force drops. One of the drawbacks for lateral force microscopy is the small tip-sample contact area by using traditional AFM tips. Therefore Lou and Kim employed bare and aluminum coated colloidal probes to quantify effects of interfaces on friction behavior of vertically aligned carbon nanotube arrays and found much higher friction forces for aluminum coated colloidal probes compared to bare borosilicate colloidal probes[44]. Besides CNTs arrays, the tribological properties of the individual nanotube were also examined using MD simulation[45], AFM[46, 47] and TEM with manipulator[48].

Using AFM, we quantitatively evaluated the adhesion and frictional properties of carbon nanotube carpet with two different tube orientations. Effects of relative humidity on friction and adhesion were thoroughly quantified in a chamber with well-controlled environment for both vertically aligned surface and transversely aligned surface. The

friction force drop on both sides of the aligned carbon nanotube carpet as the relative humidity decreases.

2.1.1. Aligned Carbon Nanotube Carpet

The multi-walled carbon nanotubes carpets with two different orientations were prepared by a xylene-ferrocene CVD method. Typically, a xylene solution with a ferrocene concentration of 0.01 g/cm^3 was used as carbon and catalyst precursors. During CVD process, Ar/H_2 gas mixture (15vol% H_2) was flowed through the reactor tube at a rate of 300 sccm. The xylene solution was fed to a preheating zone of 453 K by a flux pump continuously at a feeding rate of 0.11 cm^3/min, which became vapor and then was carried by Ar/H_2 gas (100 sccm) into the 1043 K growth zone. Several millimeter-thick carbon nanotube blocks could be prepared easily in few hours (1 to 4 hours). The morphology and individual diameter of CNTs arrays were characterized by SEM and TEM. Raman spectra were recorded using a Reni Shaw Raman scope equipped with a 514.5 nm excitation source to confirm that the carbon nanotubes in the transversely aligned surface retained their character after regrowth. Static contact angles were measured by placing droplets of de-ionized water on both surfaces of the vertically-aligned multi-walled carbon nanotubes (VAMWCNTs) and the transversely-aligned multi-walled carbon nanotubes (TAMWCNTs).

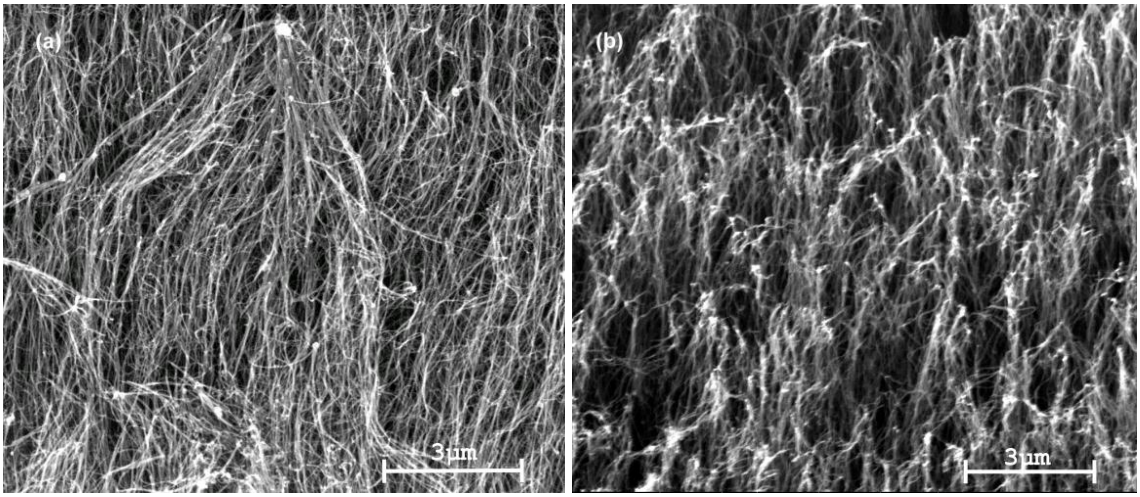

Figure 2.1 SEM images of: (a) Top view of TAMWCNT, (b) VAMWCNT, and the image was taken at a 43 ° tilt.

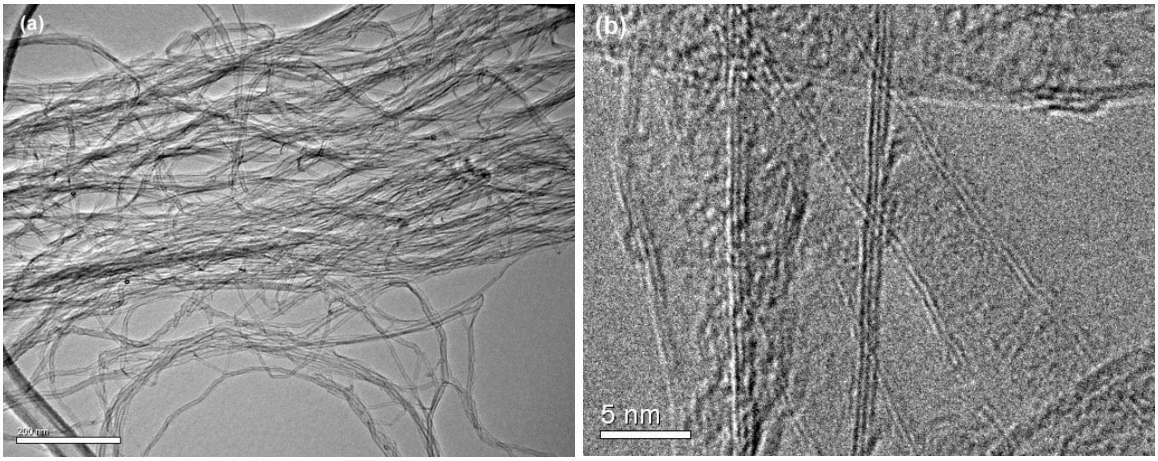

Figure 2.2 TEM images of carbon nanotube: the diameter of CNTs is around 10 nm while the length is over a couple of micron.

SEM images of the transversally and vertically aligned carbon carpet are shown in Figure 2.1. The TAMWCNT carpet was comprised of a distributed ensemble of entangled nanotubes oriented randomly in horizontal plane. The upright carbon nanotube

carpet was vertically aligned, with the last few micrometers of the top surface entangled and intertwined. The diameter of the individual nanotube was about 10 nm as shown in Figure 2.2. Because of the high anisotropy of geometric structure, mechanical, electrical and thermal properties of individual CNTs[49-51], it is expected that the frictional behavior of nanotubes is orientation dependent. The Raman spectra of both surfaces have been displayed in Figure 2.3, which had pronounced features at 1355 cm^{-1} (D mode), ~1580 cm^{-1} (G mode), and ~2683 cm^{-1} (2D mode) for VAMWCNT while features at 1354 cm^{-1} (D mode), ~1586 cm^{-1} (G mode), and ~2706 cm^{-1} (2D mode) for TAMWCNT. The intensity ratio of the D to G bands was 0.89 for both spectra. The shift in the disorder induced second order Raman peak is due to the residue compression strain [52, 53] which would not influence the tribological properties of multi-walled carbon nanotubes.

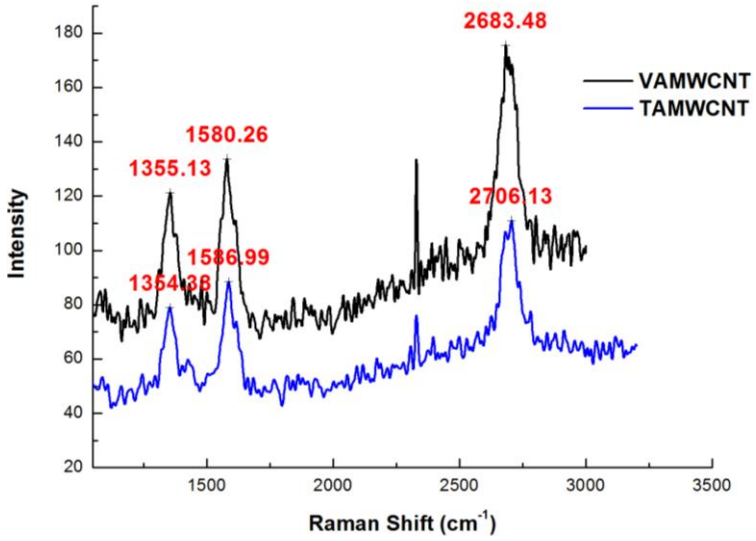

Figure 2.3 Raman spectrums of both surfaces, the shifts in CNTs characteristic Raman peaks due to the compression strain would not affect the tribological behavior of CNTs arrays.

2.1.2. Colloidal Probe Preparation and Friction Testing Procedure

A stable AFM signal cannot be obtained by sharp AFM probe because the nano-sharp probe penetrates deeply into soft CNTs carpet. Thus, a colloidal probe with a tip radius of 10 μm was employed to investigate the friction behavior of this CNTs carpet (See Figure 2.4). Borosilicate glass microspheres (Duke Scientific Corporation, diameter of 10.0±1.0 μm) were attached, with the aid of a micromanipulator Model No. 6200 to regular AFM cantilevers using Devcon 5-Minute® Epoxy adhesive. It was verified that bead was free of contamination from the epoxy from lateral image of the prepared probe as shown in Figure 2.4(a). Finally, while it was relatively easy to understand the penetration of nanoscale AFM tips into nanotube arrays, it may not be straightforward to imagine a 10 μm sized bead penetrating into nano-valleys. Although the glass bead appears smooth under optical microscope, its surface is not atomically flat. When scanned with the bead cantilever on calibration sharp arrays, it was revealed that the bead surface has nanometer roughness as shown in Figure 2.4(b). The nano-bumps on the surface play the same role as ordinary sharp AFM probes. Among all nano-bumps on the bead, only the longest one is in contact with the sample surface.

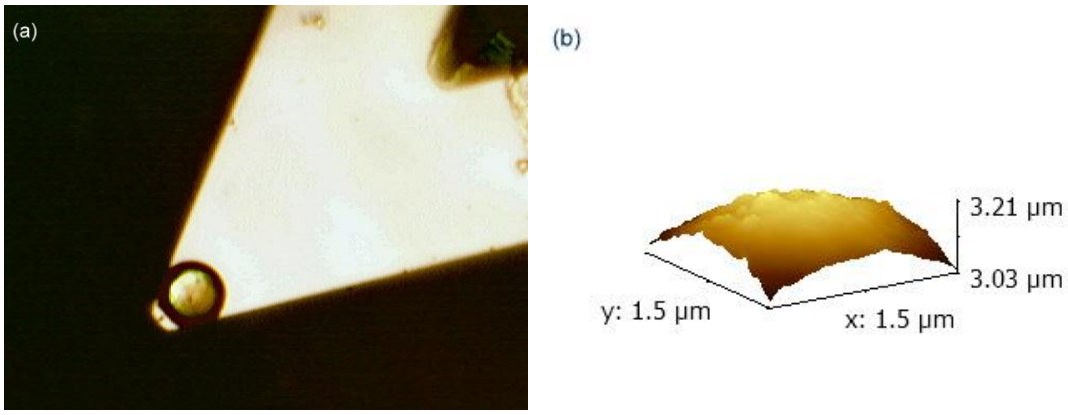

Figure 2.4 (a) Colloidal bead AFM probe, (b) Three-dimensional profile of bead AFM probe.

Lateral Force Microscopy (LFM, Pico plus, Agilent) evaluation were made on both the VAMWCNTs side and the TAMWCNTs side. The LFM scans were performed with progressively decreasing normal load for every 16 scans or so to measure the friction force as a function of the applied normal load. Both VAMWCNTs and TAMWCNTs sides were scanned at three different locations to ensure the proper representation of the sample surfaces. Scans were also repeated over the exact same location to check the reproducibility of the experiment. The test was run with a scan size of 10 μm at scan speed of 12 μm/s.

To quantify the adhesion forces between the nanotubes surfaces and the AFM probe, force versus distance spectroscopy was run on both sides and the amount of adhesion was calculated. The adhesion forces were repeated 3 times at each location and at 3 different locations on each side. Humidity of the testing environment was controlled using an environmental isolation chamber. Controlled flow of nitrogen gas was used to create dry environment with RH less than 5% and around 10%. Both relative humidity and temperature were monitored using a digital hygrometer/thermometer before, during and after the actual testing. The testing conditions are summarized in Table 2.1.

Samples	RH% (Ambient)	RH% (Mild)	RH% (Dry)
TAMWNTs Arrays	47.2~51.3	~10	0.9~3.0
VAMWNTs Arrays	26.1~41.3	~10	0.1~3.3

Table 2.1 – Relative humidity conditions for experiment.

2.1.3. Test Results and Discussion

The variation of friction force with applied normal load for the TAMWCNTs array in the ambient environment (RH 47.2~51.3%) and for the VAMWCNTs array in the ambient condition (RH 26.1~41.3%) are displayed in Figure 2.5(a). Data from multiple tests overlap closer on the transversely aligned surface compared to the vertically aligned surface. This data overlap on the transversal surface reflects the more homogeneous local surface characteristics. Clearly, the friction force is higher on a vertically aligned CNTs surface than on a horizontally aligned CNTs surface, as predicted by MD simulations[40]. The frictional coefficient values of each test are calculated and shown in Figure 2.5(b). In air, the frictional coefficient values are obviously larger for VAMWCNTs than those of TAMWCNTs. The average value is μ=0.545 with a deviation of σ=0.057 for the vertically oriented side and μ=0.167 with σ=0.015 for the transversely aligned side. Nevertheless, it was considered that these results do not really reflect the origin of the frictional behavior of CNTs against their

sliding counterparts because the bending and local buckling of the CNTs could have substantially influenced the force variation in the sliding direction in tests.

We consider that the lower friction on transversely aligned side could be due to the rolling of CNTs during contact sliding similar to a suggested mechanism of the low friction of graphite, because the CNTs in the films synthesized in this dissertation were loosely stacked and they could roll or slip under lateral sliding forces. In previous, Dickrell *et al*. performed a series of tribological experiment on both films using a borosilicate glass encounter surface at a normal load of 2mN, sliding speed of 300 μm/s and a tract length of 600 μm, while varying the film temperature. They found that the friction coefficient of the vertically-aligned film was approximately 10 times higher than the transversely distributed film and the friction coefficient monotonically decreased with the increase in temperature. They explained the anisotropy of friction through the contact area variation with CNTs orientation. Our investigations have clarified that the low friction phenomenon can be explained by the atomically smooth surface of a CNT as detailed below. A CNT is rolled from a graphite sheet. Hence, similar to a graphite sheet, a CNT is composed of planar sp2 hybridized carbon atoms, which gives an atomically smooth surface to the CNT. Because of the cylindrical shell structure of CNTs and their significantly large aspect ratio of length to diameter, transversely oriented CNT films always maintain the same smoothness advantage across any length scale from nano to microscopic dimensions. Hence, when a sliding is conducted to transversely oriented CNTs, the friction can be relatively low regardless of the dimensional scale of the sliding test.

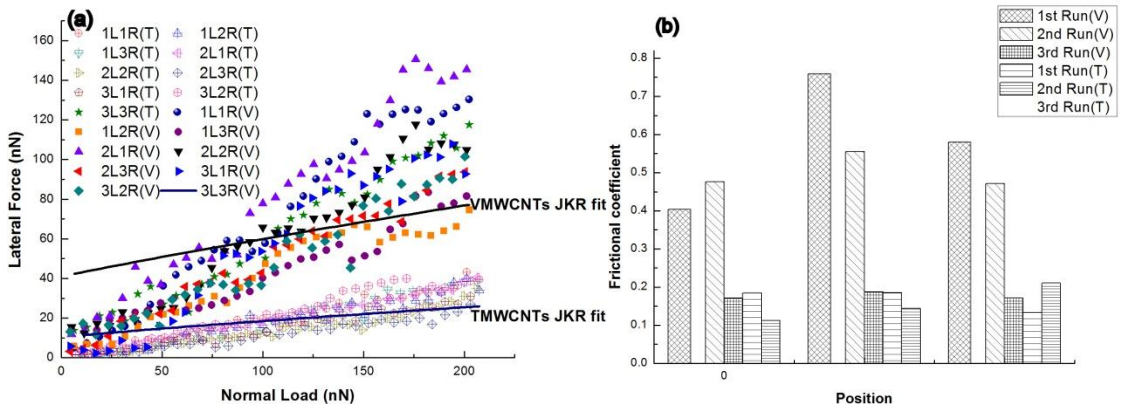

Figure 2.5 (a) Friction force vs. applied normal load in ambient condition for TAMWCNTs and VAWCNTs. Solid lines: JKR fit. Legends marked with (T) means TAMWCNTs while marker (V) means VAWCNTs. (b) Friction coefficients summary. The friction forces (frictional coefficients) on the vertically aligned CNTs surface are much higher than those on the transversely aligned CNTs surface in ambient condition (26%~52% RH).

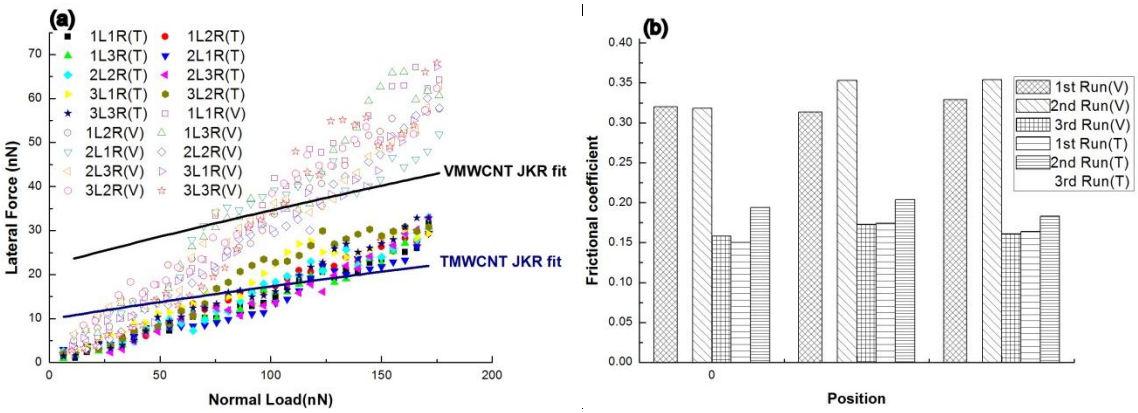

Figure 2.6 (a) Friction force vs. applied normal load in dry condition for TAMWCNTs and VAMWCNTs. Solid lines: JKR fit (b) Friction coefficients summary. The friction forces (frictional coefficients) on the vertically aligned CNTs surface are slightly higher than those on the transversely aligned CNTs surface in dry condition (RH<3.3%).

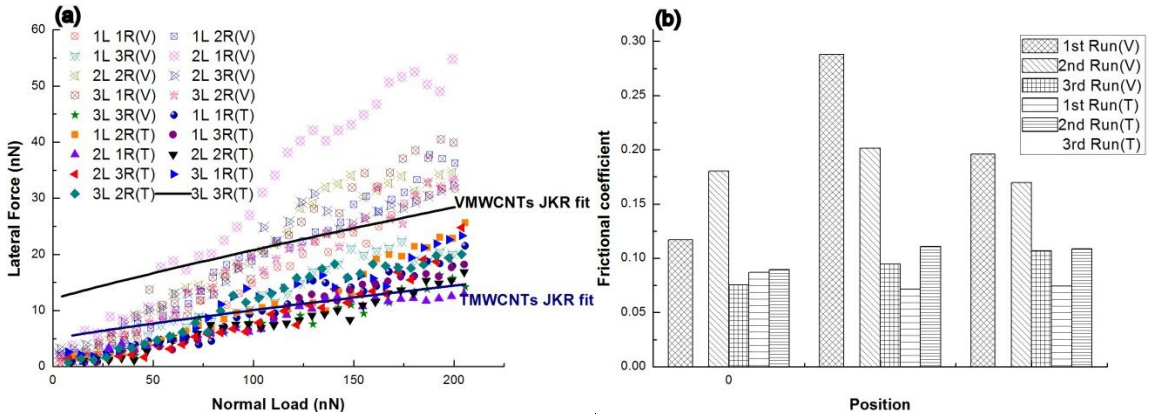

Figure 2.7 (a) Friction force vs. applied normal load in mild condition for TAMWCNTs and VAMWCNTs. Solid lines: JKR fit. (b) Friction coefficients summary. The friction forces (frictional coefficients) on the vertically aligned CNTs surface are higher than those on the transversely aligned CNTs surface in dry condition (RH around 10%).

To better understand the relationship between humidity and frictional properties, scans were also done at the other two different humidity levels. Friction forces of VAMWCNTs and TAMWCNTs plotted against normal load are shown in Figure 2.6(a) and Figure 2.7 (a) for both dry and mild condition. The variation of humidity is found to have a strong effect on friction force. Observed from Figure 2.6(a), the scattering of data from various tests on both surfaces is not distinct for the dry condition. Moreover, friction is apparently higher on the VAMWCNTs side than on the TAMWCNTs side. Similarly, the friction force dominates on the VAMWCNTs surface over the TAMWCNTs surface in Figure 2.7(a) when the relative humidity is around 10%. Although some researchers have demonstrated that humidity had an insignificant effect on the vertically aligned CNTs due to their highly hydrophobic characteristics[54-56], we draw a different conclusion: The friction forces are dependent upon the relative humidity levels based on Figure 2.5 to Figure 2.7, regardless of the orientation of the sample. Figure 2.6(b) and

Figure 2.7(b) show the coefficient of friction values of each orientation for both dry and mild conditions. In the dry condition, μ=0.184 with σ=0.013 for the vertically aligned side and μ=0.091 with σ=0.018 for the transversely aligned side. Analogously, in the mild condition, μ=0.342 with σ=0.029 for the vertically aligned surface and μ=0.173 with σ=0.025 for the transversely aligned surface.

For the sake of quantitatively studying the relative humidity as well as the orientation effects on the friction forces, the average friction forces are calculated and plotted against the applied load (Figure 2.8) for both orientations. In all cases, the humidity dependence on the frictional forces is present, but with characteristic differences depending on the CNTs orientations. For vertically aligned CNTs, the average frictional forces increase significantly with rising relative humidity, for transversely aligned CNTs, the average frictional forces difference is not evident when the relative humidity is increased to the mild level (RH~10%). Formation of a very thin water film at these interfaces was thought to decrease the effect contact area and serve as a very good lubricant to reduce friction. However, the existence of the water film would naturally cause a strong dependence of adhesion as a function of humidity level. The slight difference on transversal surface may be ascribed to TAMWCNT's surface geometry which attains water molecule saturation more easily.

Another plausible explanation could be saturation of the carbon dangling bonds at active sites on sample surfaces by chemisorption of water molecules. We think roughness of the sample surface and the extent of adhesion present between the sample surface and the AFM probe are two important factors affecting nano-scale friction behavior studied in current work. More active sites with dangling bonds (which normally cause high

adhesion between AFM probes and surfaces) result in high friction for surfaces with same roughness. Specifically, for each orientation, in ambient conditions, an active water molecule can be easily dissociated into H^+ and OH^-, and the H^+ can be easily attracted to an active site of the surfaces and passivizes it. On the other hand, in pure nitrogen conditions, due to the lack of active water molecules, the unpassivated sites will decrease the friction.

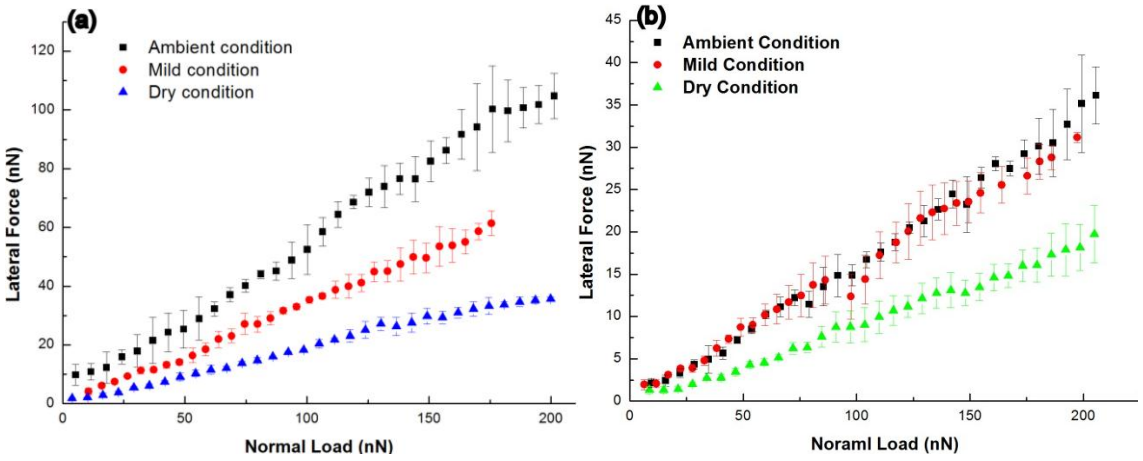

Figure 2.8 Average friction force vs. applied load as a function of humidity for (a): VAMWCNTs and (b): TAMWCNTs. The friction forces on the vertically aligned surface are more sensitive in relative humidity than those on the transversely aligned surface.

In order to evaluate the hydrophilicity of CNTs arrays, we measured and compared the static contact angles of water droplets on both CNTs surfaces. Images of water droplets sitting on these surfaces are shown in Figure 2.9. The contact angle of water on VAMWCNTs array was measured to be 131 ° (Figure 2.9(a)), whereas that on the TAMWCNTs array was 145 ° (Figure 2.9(b)). This contact angle differences indicate

that the differences of water molecule adsorption capability in the two orientations, by which it can explain the frictional properties discrepancy.

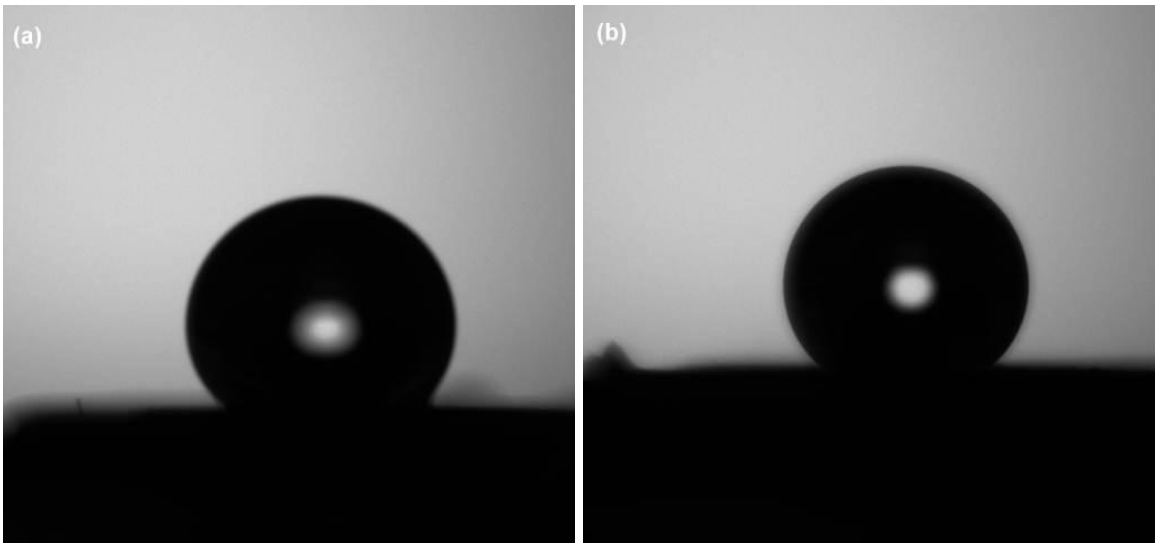

Figure 2.9 Images of water droplets sitting on the surface of the top layer (a) vertically aligned carbon nanotube array (b) transversely aligned carbon nanotube array.

Adhesion measurements were made using force calibration mode to capture cantilever deflection versus probe displacement curves. A typical deflection versus displacement curve of the colloidal tip on the vertically aligned carbon nanotube carpet is shown in Figure 2.10. The adhesion force (or the critical pulling off force) was obtained from the withdrawal part of this curve. The adhesion force is defined as the deflection without contact (the plateau of the deflection vs. displacement plot below) minus the minimum value of the deflection.

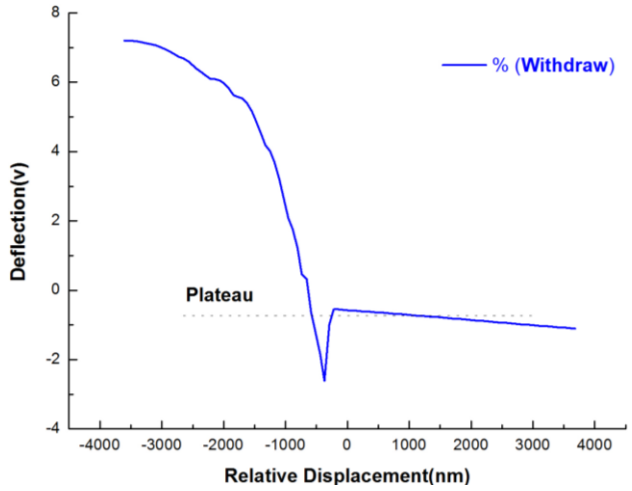

Figure 2.10 A typical case of critical pulling force measurement.

The adhesive forces of VAMWCNTs and TAMWCNTs in different environments are summarized in Table 2.2. The average adhesive forces of TAMWCNTs are lower than those of VAMWCNTs. For adhesion data of TAMWCNTs, no significant distinctions were observed among different relative humidity levels. The adhesion difference is in agreement with the previous assumption that friction would be greater due to stronger adhesive force induced by the surface water layer in the ambient condition, when the adhesive forces in VAMWCNTs dropped as the RH was decreased. Another interesting phenomenon is that the standard deviations of the adhesive force on both sides were high, which might relate to the surface roughness of MWCNTs.

Sample and Testing Condition	Average adhesion (nN)	Standard deviation (nN)
VAMWCNTs dry condition[a]	61.33	10.51
VAMWCNTs mild condition[b]	79.75	9.56
VAMWCNTs ambient condition[c]	99.32	16.75
TAMWCNTs dry condition	42.12	7.29
TAMWCNTs mild condition	57.35	8.80
TAMWCNTs ambient condition	57.84	13.59

Table 2.2 Adhesive force for VAMWCNTs and TAMWCNTs under different relative humidity levels, a. dry condition means relative humidity below 5%, b. mild condition means relative humidity around 10%, and c. ambient condition means relative humidity between 26% ~ 52%.

The assumption that the 'lateral' friction force F_L is proportional to the real contact area, A, and to a mean lateral force per unit area, the shear strength τ:

$$F_L = \tau A$$

Equation 2.1 Friction force equation.

was proposed by Bowden and Tabor in 1950[57].

The variation of friction force in different orientations is probably due to the fact that nanotubes are flexible in the direction perpendicular to the axis direction and stiff in the direction of the axis. The transversely aligned CNTs exhibited sliding and mixed sliding and rolling motions, while the CNTs that were oriented vertically buckled in response to compression, and leaned in the direction of sliding[40]. In addition, our experiments showed a dependence of friction on the relative humidity. A humidity increase can provoke the formation of water layers on surfaces, which causes capillary interaction with the tip[58]. Therefore, the presence of water molecules has a significant effect on friction.

Adhesion is of great importance, especially when measurements are done under relatively high humidity. Derjaguin[27] proposed the following modified version of Amontons' equation for adhering surfaces:

$$F = \mu(Lc + L) = Fc + \mu L$$

Equation 2.2 Modified Friction force equation.

where a constant "internal" load *Lc* is added to the external load *L* to account for the absolute value of intermolecular adhesive forces as shown in Table 2.2.

If the elastic deformation caused by adhesive forces is large compared to their range of action, the contact area as well as the critical pull-off forces can be expressed in JKR theory Equations in the following way:

$$A = \pi(\frac{R}{K}(L - 2Lc + \sqrt{4Lc(Lc - L)}))^{2/3} \quad \text{(a)}$$

$$Lc(JKR) = -\frac{3}{2}\pi R\omega_a \qquad \text{(b)}$$

Equation 2.3 (a) and (b) JKR theory equations.

where R is tip radius, ω is the work of adhesion (interface energy), and K is the contact modulus, defined as

$$K = \frac{4}{3}\left(\frac{1-\nu_{tip}^2}{E_{tip}} + \frac{1-\nu_{sample}^2}{E_{sample}}\right)^{-1}$$

Equation 2.4 Contact modulus calculation equation.

In contrast, if the elastic deformation is small compared to the range of adhesive forces, the contact area and the critical pull-off forces can employ DMT theory Equations to describe:

$$A = \pi\left(\frac{R}{K}(L + Lc)\right)^{2/3} \qquad \text{(a)}$$

$$Lc(DMT) = -2\pi R\omega_a \qquad \text{(b)}$$

Equation 2.5 (a) and (b) DMT theory equations.

If the shear strength τ is assumed to be constant, then the above solutions for contact area can be directly fitted to the friction data obtained earlier in Figure 2.5, 2.6 and 2.7. We let the radius of the AFM tip and the contact moduli are free parameters.

Both the JKR and the DMT theories were used to fit the result gained from VAMWCNTs and TAMWCNTs surfaces. Generally, both the JKR and the DMT theories work well for transversely aligned nanotubes in ambient condition. However, neither theory fit well the result for VAMWCNTs in highly relative humidity. While for samples tested under other conditions (Figure 2.6 and 2.7), the JKR and the DMT theories seem to work reasonably well.

We assume that the total, dispersive, and polar components of the liquid surface free energy (γ_l , γ_l^d and γ_l^p , respectively) are known and the contact angles are measured, as shown in Table 2.3. Insights into the interactions between liquid and solid surface are demonstrated in terms of the dispersive and polar energy contributions in the equation of Owens and Wendt[59]. This is a linear equation, Y = mX+b, in which the slope m and intercept b are given by the square root of polar and dispersive components of the solid surface free energy [$(\gamma_s^p)^{1/2}$ and $(\gamma_s^d)^{1/2}$, respectively], such as

$$Y = \frac{\gamma_l(1+\cos\theta)}{2\sqrt{\gamma_l^d}} = \sqrt{\gamma_s^p}\,X + \sqrt{\gamma_s^d}$$

Equation 2.6 Surface free energy equation.

Where X= $(\gamma_l^p)^{1/2}/(\gamma_l^d)^{1/2}$. Then X values are given by X=0.805 for PEG, 0.94 for glycerol and 1.53 for water.

Two plots according to Eq. (2.6) using the contact angles of three testing liquids measured in this study are shown in Figure 2.11. We estimated the polar (γ_l^p) and

dispersive (γ_l^d) components of the surface free energy of each carpet surface from the slope and the intercept of the linear fit in Figure 2.11. The total surface free energy, $\gamma_s^p + \gamma_s^d$, for TAMWCNTs was calculated to be 0.739 mJ/m^2, for VAMWCNTs is 2.16 mJ/m^2. Applying silicon oxide for glass, γsio_2 ~115 mJ/m^2, so the work of adhesion for glass-TAMWCNTs interface can be estimated by $\omega_a = 2\sqrt{\gamma_{TAMWCNT}\gamma sio_2}$ ~18.5 mJ/m^2, while the work of glass-VAMWCNTs interface is $\omega_a = 2\sqrt{\gamma_{VAMWCNT}\gamma sio_2}$ ~31.5 mJ/m^2. Both Eq. (2.3b) and Eq. (2.5b) were employed to calculate the pulling forces. One thing that should be mentioned is that the local contact radius of curvature is smaller than radius of curvature of the attached bead (Figure 2.4(b)). 1000 nm as the representative radius of curvature is applied here, gives the critical pulling forces of TAMWCNTs to be 87 nN for JKR and 116 nN for DMT, while VAMWCNTs has 148 nN for JKR and 198 nN for DMT. Based on those values, the JKR estimation seems to be more consistent with the experimental value (Table 2.2), which indicates that the JKR theory works better for both VAMWCNTs and TAMWCNTs.

According to the Amonton's law, the friction force between two bodies at macroscale is linearly proportional to the applied load L and independently of the macroscopic contact area. Later, the friction force was shown to be proportional to the real contact area, due to the macroscopic area is rough and consists of a large number of asperities. Some researchers argued that the breakdown of the single-asperity theories is due to the fact that at this length scale the real contact area A_r is different from A_{asp} and the friction force should be defined in terms of A_r. A nonlinear fitting with two free parameters has been used in this series of fitting. After fitting, two free parameters P_1 and

P_2 were obtained. Using P_1 and K, we can calculate the shear strength τ, then by using A=F/ τ, we can back up the contact area.

1) **The contact modulus K is calculated from data in Table 2.3 by using Equation. (2.4), where τ is shear strength.**

   $$\boldsymbol{F = A * \tau},$$

2) **We use two free parameter nonlinear fitting to do JKR fitting, $P_1 = \tau * \pi(\frac{R}{K})^{2/3}$, P_2=Lc.**
3) **The fitting equation is $F=P_1*\{L-2P_2 + [4P_2*(P_2-L)]^{1/2}\}^{2/3}$, the x axis is normal load L and the y axis is friction force F.**
4) **After fitting, we will get those free parameters P_1 and P_2.**
5) **Using $P_1$and K, we will get the shear strength τ, then by using A=F/ τ, we can get contact area or contact size.**

Materials	Poisson's ratio	Young's modulus (GPa)
Silicon Oxide	0.17	70
Carbon Nanotube	0.06	800

Table 2.3 Material Properties of Contacting Surfaces.

The contact area information for both transversely and vertically aligned CNTs surfaces were listed in Figure 2.11(b). Essentially, the contact area for vertically aligned surface is relatively larger than that on transversely aligned surface for the similar normal

load. But apparently, the real contact area increases with the increasing normal load, although there is no significant difference for different relatively humidity level for each orientation.

Probe Liquid	$\gamma_l\ (mJ/m^2)$	$\gamma_l^d\ (mJ/m^2)$	$\gamma_l^p\ (mJ/m^2)$	**Contact angle(°) TAMWCNTs**	**Contact angle(°) VAMWCNTs**
PEG	48.3	29.3	19.0	147	127
Glycerol	64.0	34.0	30.0	144	130
Water	72.8	21.8	51.0	145	131

Table 2.4 Surface energy parameters of the probe liquids used in the experiment and the contact angles measured experimentally.

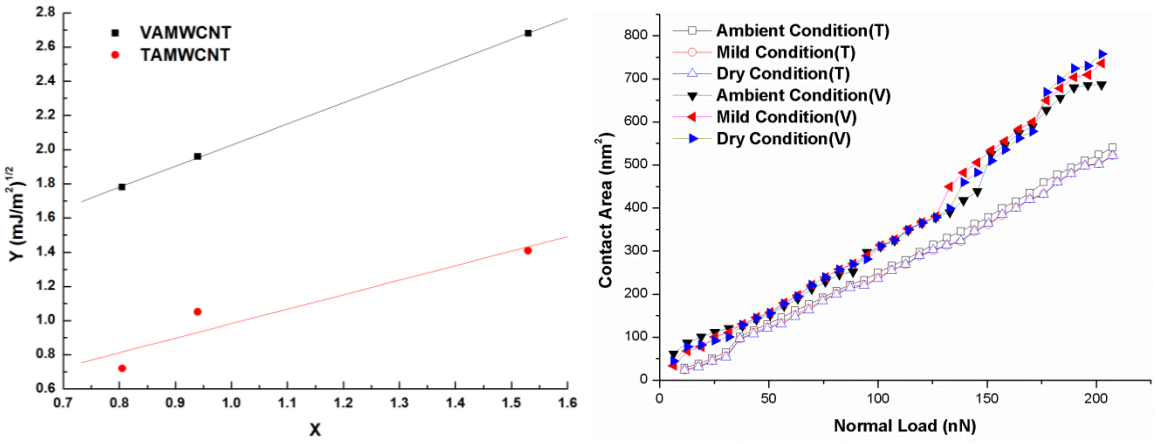

(a) (b)

Figure 2.11 (a) The Owens and Wendt plot for CNTs Carpet surfaces according to Eq. (3.6), (b) Fitted Contact Area bwteen CNTs Carpet and AFM Probe.

2.2. Nanoscale Frictional Characteristics of Graphene Nanoribbons (GNRs)

GNRs are emerging as promising candidates for a wide range of device applications, from field-effect transistor (FETs) and sensors to memory device, due to their unique properties[60-62]. Specifically, a GNR with a width < 10 nm is semiconducting[63]. The transport measurement on GNRs shows remarkably high electron mobility at room temperature, with a reported value in excess of 3,150 $cm^2V^{-1}s^{-1}$[64]. Murali *et al.* have recently found that the average resistivity of GNRs at a given line-width (18 nm<W<52 nm) is comparable to that of copper[65]. In addition, graphene appears to be one of the strongest materials ever tested, with a breaking strength 200 times > steel, demonstrating a tensile strength up to 130 GPa[66]. The spring constant and the Young's modulus of suspended graphene sheets have been measured using AFM. The measured spring constant was in the range of 1-5 N/m and the Young's modulus was ~0.5 TPa. These are all desired attributes for GNRs applications in NEMS devices.

Typical GNRs fabrication methods include micro-fabrication on graphite surfaces[67], exfoliation of bulk graphite in the presence of surfactants[68], solution-based oxidative methods[69], and plasma etching of MWNTs partially imbedded in a layer of protective polymer[70]. Surface interaction forces, such as adhesion and friction forces between relevant contacting surfaces during fabrication and subsequent device integration processes are crucial at the nanoscale because of the high surface-to-volume ratio of GNRs. Therefore, careful evaluation of the tribological properties of various GNRs could have important implications for efficient fabrication and reliable operation

of GNRs-based devices. Additionally, GNRs or graphene oxide nanoribbon (GONR) reinforced polymer nanocomposites have recently shown great promise due to the existence of abundant interfacial interactions of the polymers with the covalently bonded functional groups of the GNRs and GONRs, and the outstanding mechanical properties of GNRs and GONRs[71, 72]. It is thus imperative to understand the tribological behavior of GNRs with different chemical functionalization addends before successfully utilizing these unique graphene nanostructures reliably in structural nanocomposite and device applications.

In this section, we evaluate the nanoscale tribological behaviors of three different GNRs including GONRs[69], GNRs[73] derived from potassium splitting (K-GNRs)[74] and nitrobenzene functionalized GNRs (N-GNRs) by AFM. The surface topography was characterized by SEM and AFM while X-ray photoelectron spectroscope (XPS) was used to analyze the chemical functionalization of GNRs. The frictional responses of three different GNRs at different normal loads, as well as the effect of relative humidity were then carefully quantified. Adhesion forces were also collected from multiple force-displacement measurements.

2.2.1. Functionalized Graphene Nanoribbons and Testing Procedure

In order to probe the effects of chemical functional groups on frictional properties and their potential implications in various applications, N-GNRs prepared by diazonium chemistry (N-GNRs)[74], K-GNRs[73] as well as GONRs[75] were selected for this study. GNRs were suspended in ethanol (at a concentration of ~ 0.1 mg/cm^3). A droplet of each GNRs solution was spin coated onto a silica substrate using an EC101DT-R790

photoresist spin coater (Headway Research, Inc.) at 500 RPM for 30 s. The sample was dried at ambient conditions for 300 s. The Picoplus 5500 AFM (Agilent Technologies) was used to obtain both the topographical image and the corresponding friction force mapping of the different GNR samples. The humidity of the testing environment was controlled using an environmental isolation chamber that separates the AFM from the ambient conditions (i.e., relative humidity recorded at 45%). A controlled flow of nitrogen gas was employed to create dry environment with a relative humidity level < 5%[76]. Silicon cantilevers (NanoScience, Phoenix, AZ, USA) were used for the subsequent adhesion and friction measurements. The force versus distance (FD) curve was collected after each scan at least five times at different locations, in order to obtain corresponding adhesion forces between the AFM tip and different GNRs.

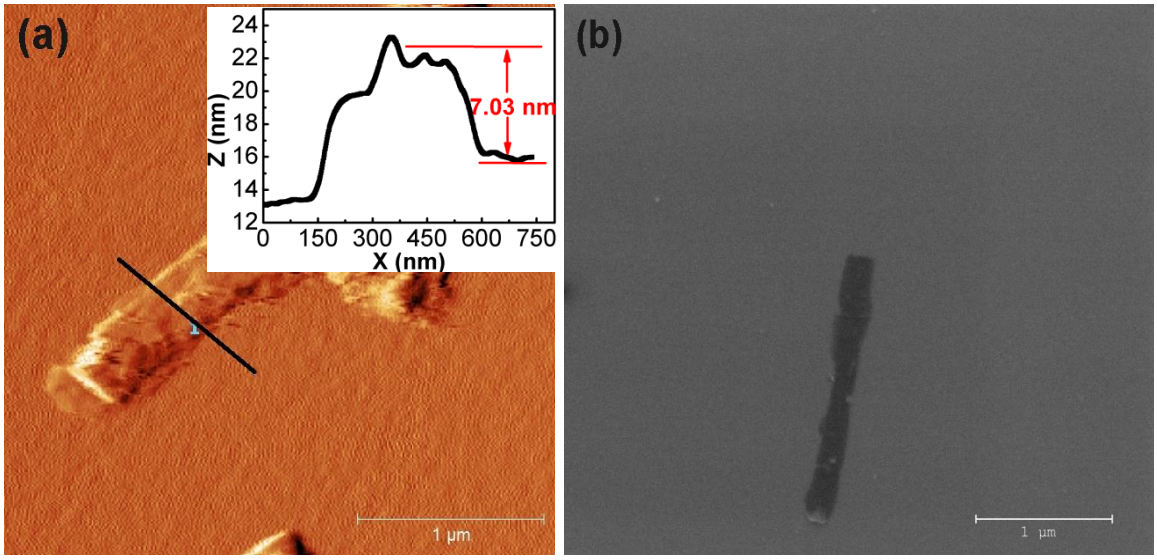

Figure 2.12 (a) A typical contact-mode AFM topography image of a GONR, the height measurement details shown in the inset, the height indicates a stack of ~7 layers. (b) A characteristic SEM image of a GONR stack on a SiO_2 surface.

The general morphological and surface structures of the N-GNRs, K-GNRs and GONRs were found to be similar as surveyed by a FEI Quanta 400 SEM and a Agilent Picoplus AFM. A representative contact-mode AFM topographical image of GONRs is shown in Figure 2.12(a). The typical height of this GONRs, estimated from AFM height profile, was ~ 7 nm (the inset of Figure 2.12(a)), which corresponds to a few layers of GONR sheets. A characteristic SEM image (Figure 2.12(b)) of a GONR on a SiO_2 surface revealed the few-layered ribbons was several micrometers in length, with straight edges and relatively uniform widths of < 200 nm. The thickness measurements for all three GNRs are summarized in Table 2.4.

Sample	N-GNRs	K-GNRs	GONRs
Thickness (nm)	6.45 ±1.93	7.87 ±2.31	8.91 ±3.72

Table 2.4 The thickness measurement of GNRs.

XPS was used to verify the chemical functionalization level and atomic composition of the resulting GNRs. For N-GNRs, high-resolution XPS of Figure 2.13(a) shows a strong signal for the N 1s peak, O 1s as well as O 2s peaks. The signal at 400 eV in the inset of Figure 2.13(a) can be attributed to the nitro group[74]. The remaining edge carboxyl groups would go through little reductive loss for N-GNRs, with 25% surface oxygen atoms detected (Table 2.5). The K-GNRs were produced through non-oxidation methods, resulting in only 4.5% physisorbed oxygen atoms detected, while the excess potassium salt were consumed by ethanol and water during the quenching process[73]. The high oxidation content of the GONRs was substantiated by XPS analysis. As shown

in Figure 2.13(c), the XPS spectrum of C1s for GONRs exhibits a high intensity oxygen peak and the content of oxygen is 44%. A small portion of nitrogen content is present in GONRs, which can be attributed to the hydrazones formed during the oxidation[74, 77]. The signals (inset of Figure 2.13(c)) at 285.8 eV correspond to the C-O bond, the intensity of which correlates to the level of oxidation within the sample while the signal at 284.9 eV corresponds to C-C bonds[73]. The complete XPS results of the three GNRs are summarized in Table 2.5.

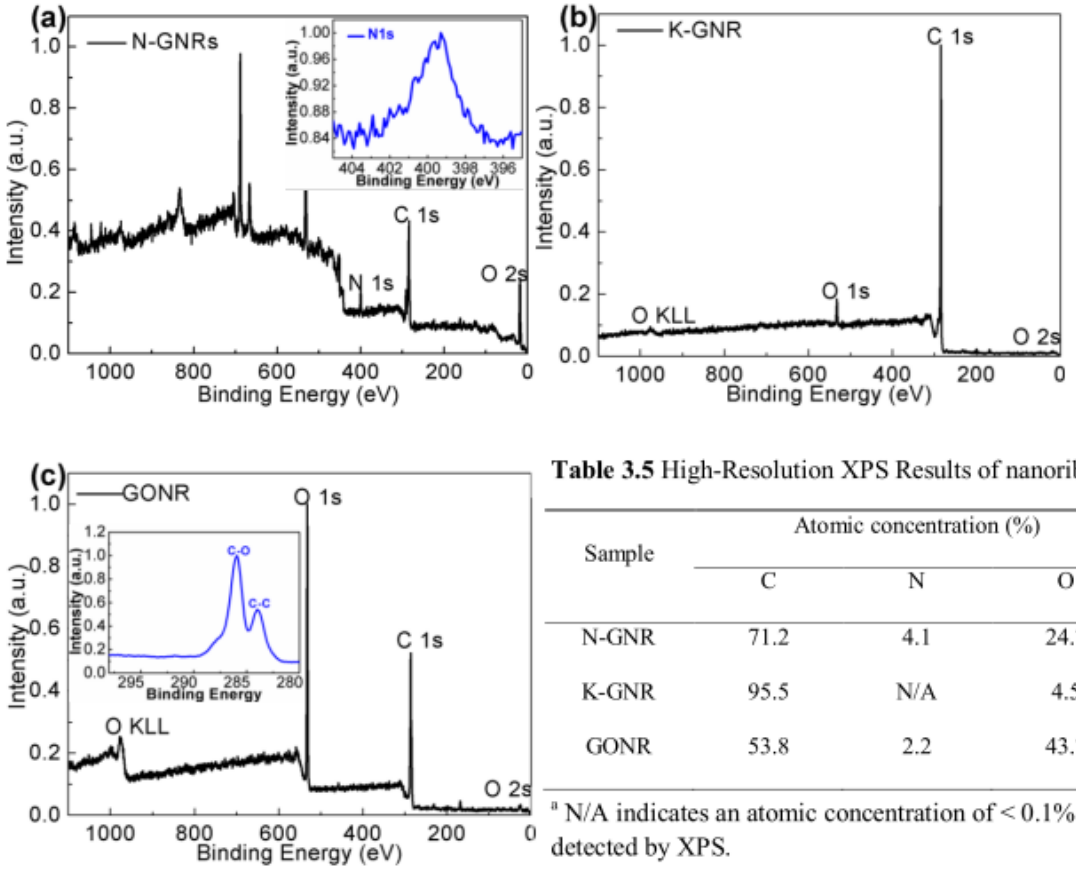

Table 3.5 High-Resolution XPS Results of nanoribbons[a]

Sample	Atomic concentration (%)		
	C	N	O
N-GNR	71.2	4.1	24.7
K-GNR	95.5	N/A	4.5
GONR	53.8	2.2	43.7

[a] N/A indicates an atomic concentration of < 0.1% was detected by XPS.

Figure 2.13 (a) High-resolution XPS spectra of N-GNRs, (b) K-GNRs and (c) GONRs; the top inset in (c) is the XPS C1s spectrum of the GONRs.

2.2.2. Tests Results and Discussion

The frictional behavior of the nanoribbons was carefully evaluated using an AFM in both ambient and dry nitrogen environments (Figure 2.14). Scan areas were set to 100 × 100 nm^2, and the scan rate was 0.6 Hz. We employed the reference cantilever method[78] to calibrate the AFM tip's normal spring constant and the diamagnetic lateral force calibrator approach to calibrate the AFM lateral force output[44, 79]. The friction force versus normal load curves were collected at three different positions at least three times and average values were calculated. For GONRs, N-GNRs and K-GNRs, the friction response was observed to increase in an almost linear fashion as the normal load was raised (Figure 2.14(a)-(c)). Out of the three types of GNRs quantified, the friction force of GONRs was the highest at different levels of normal loads, those of N-GNRs were the next, and those of K-GNRs were the least in ambient conditions as shown in Figure 2.14 (a). In the dry nitrogen enviroment, the same trend persisted but the differences in friction were insignificant for normal loads under 20 nN. It is worth noting that the reported thickness dependent friction behavior in the mechanically exfoliated graphene[80] was thought not to play a big role here, since the GNRs investigated in this work were all over 5 nm in thickness (Table 2.4) and their friction characteristics should therefore approach the thickness-independent bulk behaviors. To further confirm this, three representive friction vs. normal load curves collected from different GONRs samples with different thicknesses are shown in Figure 2.14 (c), clearly demonstrating that the friction responses were independent of sample thickness. According to the curves, the nominal friction coefficients for different nanoribbon samples were fitted to be ~ 0.5-1.2. Although a much lower friction coefficient (0.004 for HOPG) was reported

by Buzio *et al.*[81], the relative friction coefficient (RCF) of reduced graphene oxide is about 0.86 and RCF for graphene oxide is as high as 2.11[82]. Furthermore, the wear phenomenon has been rarely observed in graphene nanoribbons though the applied normal load were relatively high. The topography images before and after friction tetsing have shown that no noticeable wear scar was generated.

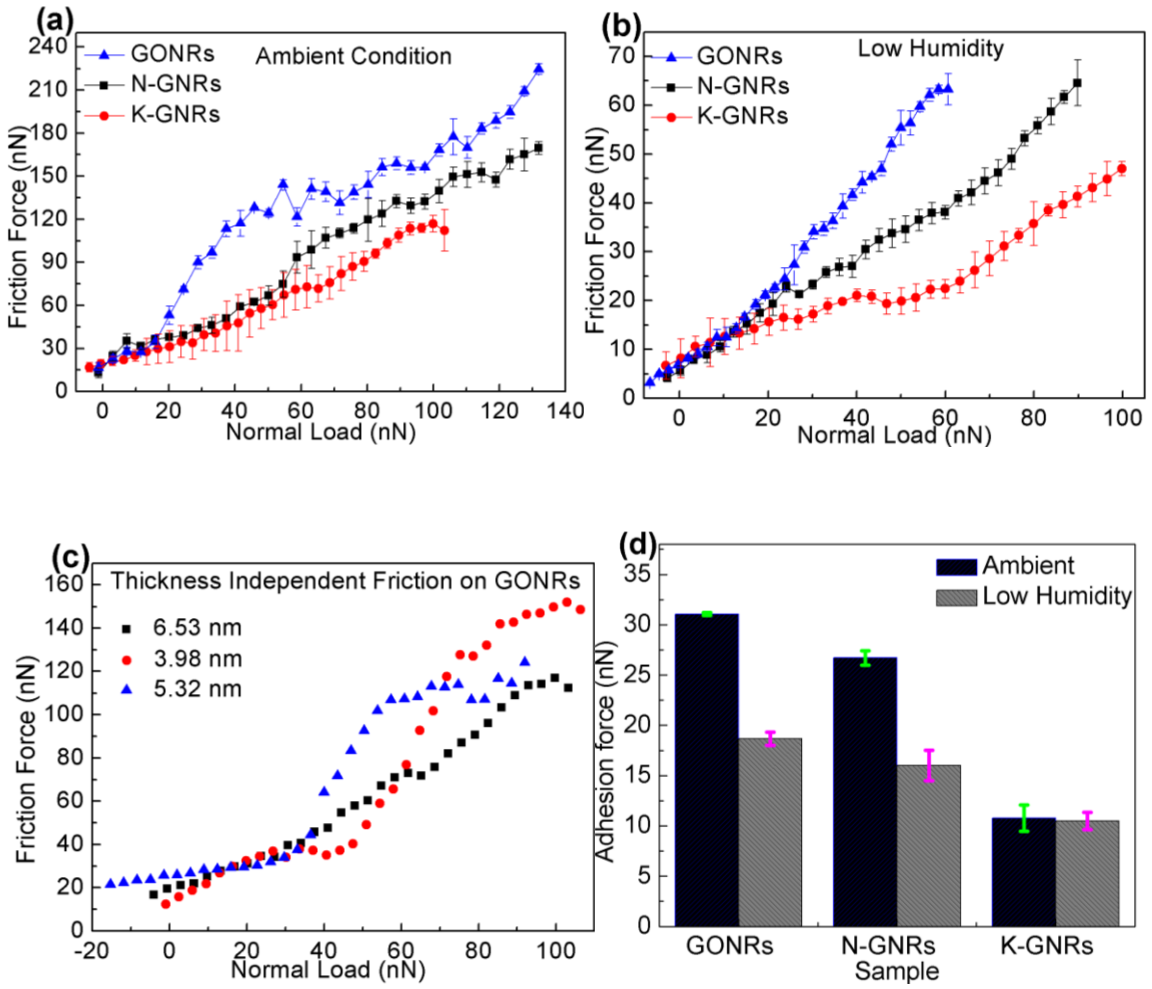

Figure 2.14 Normal force dependences of friction on GONRs, N-GNRs and K-GNRs in (a) ambient condition, (b) dry nitrogen condition. (c) Thickness independent friction on GONRs in the ambient condition, 3 random data set with different sample thickness. (d) Adhesion force for all types of graphene nanoribbons in ambient and low humidity conditions.

It is generally believed that the radius of curvature of the AFM probe has a effect on the magnitude of frictional forces. In order to exclude the tip radius effect on frictional response of graphenen based nanoribbon, the AFM probe was scanned on a standard unltra-sharp gratings provided by NT-MDT company (Santa Clara, CA,USA). The obtained topography images are the convolution of the AFM tip and sample surface, which represents the profile of the AFM tip, as shown in Figure 2.15. The tip radius was measured at a height of 10 nm away from the apex of the tip and a circular cross section was surveyed. It was demonstrated that the tip radius did not change significantly, while the tip radius is 14.3 nm before scanning and 15.6 nm after testing.

Since the observed difference in friction is not a result of sample thickness, as stated earlier, the effect of chemical interaction-induced adhesion between the AFM tip and GNRs due to different surface functional groups[83] was further carefully assessed. This is because the friction force can generally be described by the dependence of true contact area and the interfacial shear strength for nanoscale single asperity contact as in the case of AFM based nanofriction studies. From contact mechanics theories considering adhesion forces, such as JKR theory (describing the relationship between contact area and normal load, including adhesive forces for relatively compliant materials and strong adhesive forces) and DMT theory (generally works for relatively stiff materials and weak adhesive forces), adhesion has a strong direct correlation with friction when the interfacial shear strength is assumed to be a constant. The chemical effects on adhesion are well-documented in the literature; Noy *et al*.[84] used chemical force microscopy to measure adhesion and friction between probe tips and substrates covalently modified with self-assembled monolayers that terminate in distinct functional groups. They

demonstrated that the magnitude of friction force decreased in the following manner with different tip/sample functionalities: COOH/COOH > CH_3/CH_3 > COOH/CH_3. Poggi *et al*.[85] examined the adhesion between thiolated AFM cantilever tips and SWNTs paper, and then observed a direct correlation of adhesion force with respect to the thiol terminal group (NH_2 > CH_3 > OH). Most recently, Lu *et al.*[86] developed and implemented an AFM based adhesive force mapping technique combined with a statistical analysis method to study adhesive interactions of small SWNT bundles functionalized by amino, epoxide, and hydroperoxide groups as compared to sodium dodecylsulphate (SDS) treated SWNTs in an controlled environment, and it was found that the adhesion forces of amino functionalized SWNTs and SDS-wrapped SWNTs were larger than those of epoxide group terminated and hydroperoxide terminated SWNTs.

The adhesion forces for both ambient and low humidity conditions obtained from regular AFM FD curves are summarized in Figure 2.14(d). The measured adhesion forces for GONRs and N-GNRs were much higher than those of K-GNRs. The difference in measured adhesion forces is attributed to the abundant existence of nitrophenyl and carboxyl groups available on these two nanoribbons, while almost no functional groups were detected on K-GNRs. Another possible reason could be due to the increased hydrophilicity of GNR surfaces with increasing oxygen content (Table 2.5), giving rise to an enhanced adhesive interactions between the AFM tip and the water layer covered surfaces predicted by classical meniscus theory. Friction forces between different GNRs thus correlate directly with the adhesion forces for these same functional groups in the ambient enviroment. Specifically, higher friction is observed between the tip and the nanoribbons that adhere strongly, while low friction is observed bewteen the weakly

interacting tip and GNRs. In the low humidity condition, the friction forces of GNRs follow the same order: GONRs > N-GNRs > K-GNRs especially when the normal load is larger than 20 nN. Interestingly, the magnitude of the friction forces are dramatically smaller than those measured in the ambient condition (Figure 2.14(a) and (b)). As the relative humidity decreased, the adhesion forces for N-GNRs and GONRs dropped almost half compared to the ambient condition, but the adhesion force remained constant for K-GNRs. It is worth noting that K-GNRs are less sensitive to humidity because of few surface functional groups, producing a highly hydrophobic surface. Sumant *et al*.[87] have drawn the similar conclusion that the friction was substantially reduced by eliminating the reactive, polar and π-bonded surface groups and grafting fully saturated hydrogen-terminated surface bonds. The hydrophilic nitrophenyl groups boosted the adsorption of water molecules on N-GNRs surfaces, and then the friction force of N-GNRs was shown to be suppressed by the low relative humidty. It is thought that the oxygen containing groups, especially caboxyl groups also, contributed to this humidity sensitive friction. Specifically, the hydrophilic carboxyl groups played a significant role in reducing friction force under low relative humidty.

Wear scars could be possibly generated on the surface by scanning the sample under high normal loads. However, in this experiment, although the friction force and normal loads are relatively high, the wear phenomenon has very rarely been observed. The sample surface was re-scanned right after the friction testing. The topography comparisons (before and after friction testing) have shown that no noticeable wear scar was generated after the friction testing, as shown in Figure 2.16. The slight difference in the topography image is due to the sample drift.

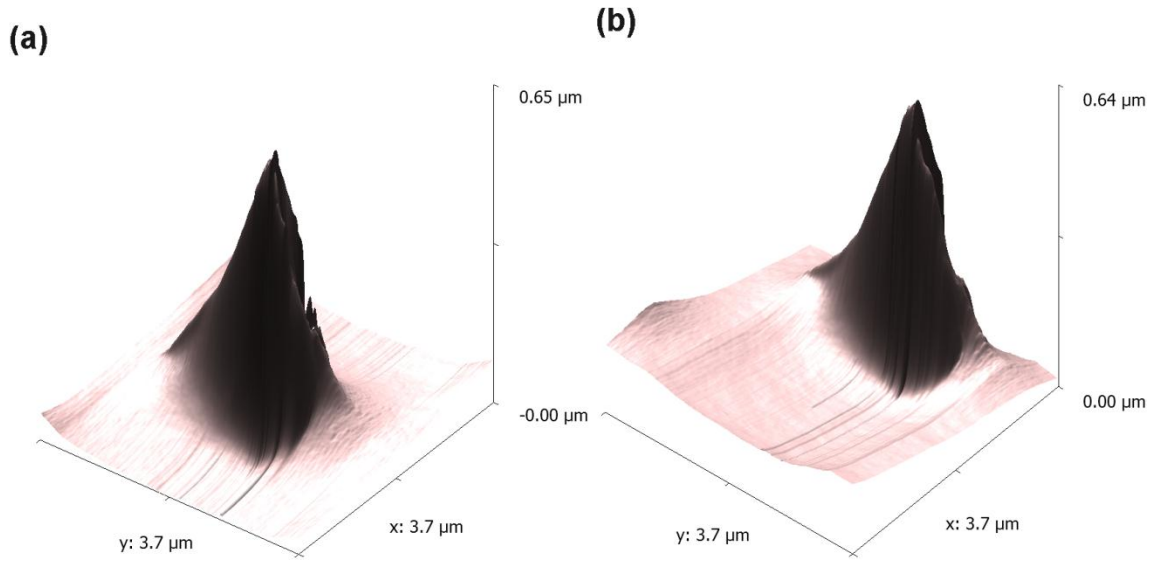

Figure 2.15 The AFM tip profile before (a) and after (b) friction testing in a typical experiment.

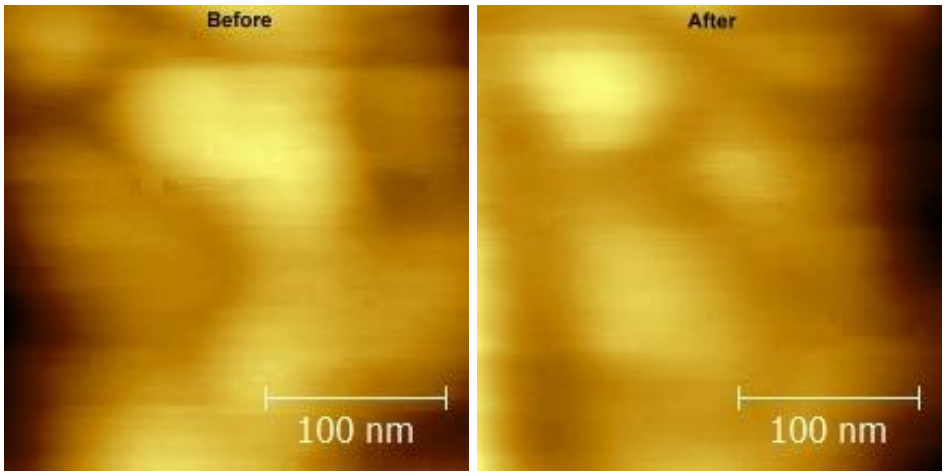

Figure 2.16 Topography images before and after high load applications.

2.3. Conclusion

The tribological behavior of three different GNRs were carefully studied by AFM. The covalently functionalized N-GNRs and oxidized GONRs have higher friction force compared to K-GNRs split by potassium vapor, both in ambient and dry nitrogen conditions. The adhesion force difference among GNRs as well as the different surface hydrophilicity were considerd to explain the observed friction differences of GNRs. By delineating the friction merits of different GNRs, this study could offer some insights into future efforts to utilize graphene nanoribbons in fundamental studies and emerging practical applications.

Chapter 3

3.Friction Study at the nanometer scale

3.1. Size Dependent, Thermally Activated Friction

3.1.1. Introduction

The recent development of new experimental tools such as the friction force microscopy (FFM, i.e., AFM equipped with lateral force measurements) has enabled a quantitative examination of frictional behavior for well-defined contacts with sizes ranging from a few nanometers to micrometers[88-90]. A representative measurement by FFM exhibits the stick-slip behavior as the cantilever tip slides on a crystalline surface, from which one can deduce the lattice spacing, lateral contact stiffness, and friction force. The atomic stick-slip behavior critically depends on lattice structures of the two contacting surfaces, sliding direction, contact size, sliding velocity, temperature, etc. The force-displacement curves obtained from the FFM measurements represent an integral measure of the collective behavior of atoms and defects on and near the interface. It is

therefore a difficult task to unambiguously extract from this integral measurement the governing atomic mechanisms for frictional sliding.

Existing modeling work in the study of atomic frictional behavior has generally focused on either semi-continuum Tomlinson-type models or molecular simulations. In the Tomlinson model, a virtual contact point is connected to the faraway reference point by a spring and moves on top of a periodic potential which mimics the tip-substrate interaction. For a compliant spring or high potential amplitude, the stable solution after the friction force reaches maximum will be a sudden jump to the contact in the next period, leading to the stick-slip behavior. Socoliuc *et al.*[91] found the transition from a smooth sliding to the stick-slip behavior as the contact load increases. Their explanation based on the Tomlinson model showed that the potential amplitude is roughly proportional to the normal load and may vary by orders of magnitude. It should be noted that this 1-degree-of-freedom model is equivalent to assuming a uniform lateral motion of all atoms on the contacting interface, while we believe that surface atoms of the two contacting solids will prefer to shear/slide non-uniformly in a completely different manner, i.e., some atoms on the interface will break the bonds earlier while the rest do so later – the boundary between them is a dislocation. In our recent Peierls-type model[92], we view the atomic frictional process as the initiation and gliding passage of dislocations with diffused cores on the interface. Experimental observations on contact size dependence can thus be explained as a transition of homogeneous to inhomogeneous slip characteristics with the increase of contact size.

Stick-slip curves have been found to depend on the sliding velocity and temperature – characteristics of the stress-assisted, thermally activated process[93-96].

The understanding of the thermally activated frictional behavior can be obtained by the transition state theory. From the kinetics standpoint, the system may be thermally activated and jump from one metastable state to another, and the activation energy is the potential-energy difference between the initial metastable state and the saddle point configuration when the applied lateral force is lower than the athermal friction force. At low temperatures, the thermal energy is low so that it is less probable for this thermally activated process to occur. A large sliding velocity indicates a short total time, and therefore the total activation probability is also low. In these conditions, the measured friction force will be close to the athermal limit. In Tomlinson model, the saddle-point configuration is apparently a uniform slip. Therefore, the application in experiments that studied both contact-size and sliding-velocity dependence again relies on a contact-size dependence derived from the amplitude of tip-substrate interaction potential[91]. The Peierls framework permits the solution of a spatially inhomogeneous saddle point configuration, which, in principle, leads to a coupled size- and velocity-dependence of the friction force.

3.1.2. Experimental Methods

FFM experiments were conducted on freshly cleaved and atomically smooth mica samples. Different scan dimension were employed in order to obtain varied scanning velocities, as summarized in Table 3.1. The friction forces and the surface topography of the mica surface were investigated at room temperature (295.5 ± 0.4 K) and under relative low humidity level (<4%) by means of an atmosphere control chamber. We used a monolitic silicon FFM probe with nominal radius of 10 nm. Normal force constant is *in situ* calibrated by a standard pre-calibrated cantilever with known stiffness[97]. A simple

and reliable way for AFM based friction force calibration with high accuracy and effectiveness was carefully performed *in situ* before experiment[98]. The normal and lateral stiffness obtained in this experiment are K_N=0.096 N/m and K_L=1.14 N/m.

Scan Velocity (nm/s)	**4**	**6**	**12**	**16**	**20**	**28**	**40**	**200**	**600**	**1600**	**3200**	**$4*10^3$**	**4800**	**$6*10^3$**	**$8*10^3$**	**10^4**
Scan Size (nm)	10	10	10	10	10	10	10	500	500	500	10^3	$2*10^3$	$3*10^3$	$3*10^3$	$5*10^3$	$5*10^3$

Table 3.1 The Scanning conditions of FFM probe over fresh cleaved mica surface.

The normal loads were set by the "Force Setpoint" parameter of the AFM. During each scan, 512x512 data points were collected. Friction force for a normal load is the average value which contains the entire scan. For each scan line in both directions, we could plot a friction loop using measurements of the lateral deflection of the AFM cantilever. The procedure to calculate the friction force from a friction loop is as follows (Figure 3.1):

1. **Truncate the static friction data (left to right scan, to the first local maximum. Right to left scan, to the first local minimum).**
2. **Find the maximum of left to right scan line F_{max} , and the minimum of right to left scan line F_{min}**
3. **The friction force in volts unit is given by $F=(F_{max} - F_{min})/2$**

Multiply locations of samples were scanned to ensure statistical significance. The sliding friction results are exhibited in Figure 3.2 showing F_L vs lnV for different normal

loads F_N. A plateau of friction force F_L was obtained at a characteristic velocity V_0 following a coarsely logarithmic increase of F_L with V. These two limiting cases are indeed predicted by Eq. (3.7). It is a significant discovery that the equation prediction is in accord with the experiment of the plateau for $V > V_0$.

The roughly linear increase of the activation energy reported in Figure 3.6 (a) is consistent with previous report[95]. It is clearly observed that V_0 increases from 3200 nm/s to 6000 nm/s if we consider the transition point of logarithm to plateau as the characteristic velocity in Figure 3.2. The fitted characteristic velocities V_0 under different normal loads have been exhibited in Figure 3.6 (b). Compared with the experimental data, the characteristic velocities increase linearly with normal load and are of the same magnitude.

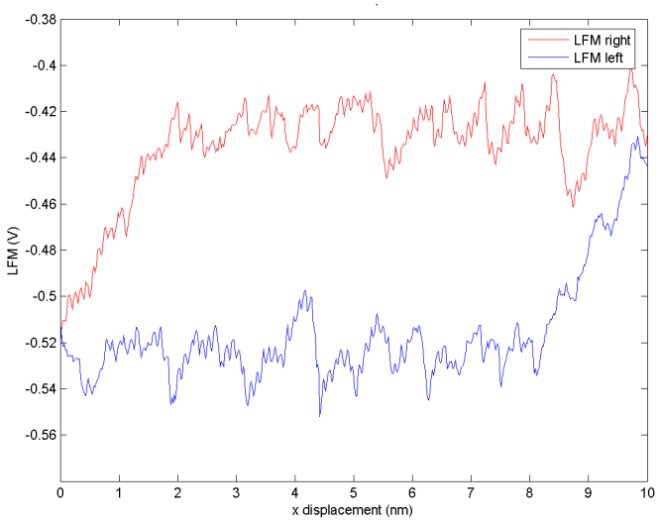

Figure 3.1 A Typical Friction Loop on Mica sample.

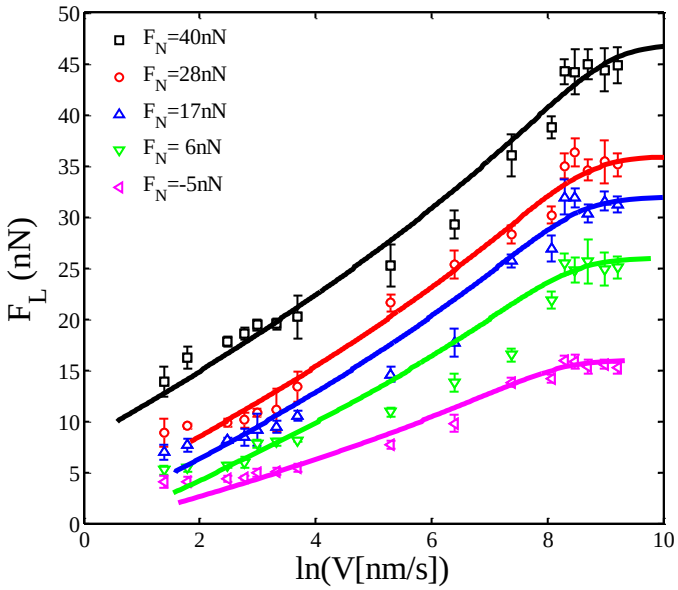

Figure 3.2 Friction force (extracted as the half value of the bounds of the stick-slip curves) increases as a function of sliding velocity. Solid lines are fitting results from theoretical model in Eq.(3.7).

3.1.3. JKR Fitting

If the elastic deformation caused by adhesive forces is large compared to their range of action, the contact area as well as the critical pull-off forces can be expressed in JKR theory Equations in the following way:

$$A = \pi\left(\frac{R}{K}(L - 2Lc + \sqrt{4Lc(Lc - L)})\right)^{2/3}$$

Equation 3.1 JKR Theory Equation.

where R is tip radius, ω_a is the work of adhesion (interface energy), and K is the contact modulus, defined as:

$$K = \frac{4}{3}\left(\frac{1-\nu_{tip}^{2}}{E_{tip}} + \frac{1-\nu_{sample}^{2}}{E_{sample}}\right)^{-1}$$

Equation 3.2 Contact Modulus Calculation Equation.

Materials	Poisson's ratio	Young's modulus (GPa)
Silicon Oxide	0.17	70
Mica	0.25	60

Table 3.2 Material Properties of Contacting Surfaces.

In this series of experiment, the radius of AFM contact mode tip is 10 nm.

1) **The contact modulus K is calculated from data in Table 3.2 by using Equation. (3.2), where τ is shear strength.**

$$\boldsymbol{F = A * \tau},$$

Equation 3.3 Friction Calculation Equation.

2) **We use two free parameter nonlinear fitting to do JKR fitting, $P_1 = \tau * \pi\left(\frac{R}{K}\right)^{2/3}$, P_2=Lc.**
3) **The fitting equation is $F = P_1*\{L - 2P_2 + [4P_2*(P_2 - L)]^{1/2}\}^{2/3}$, the x axis is normal load L and the y axis is friction force F.**

4) **After fitting, we will get those free parameters P_1 and P_2.**

5) **Using $P_1$and K, we will get the shear strength τ, then by using A=F/ τ, we can get contact area or contact size.**

A nonlinear fitting with two free parameters has been used in this series of fitting. After fitting, we will get those two free parameters P_1 and P_2. Using P_1 and K, we will get the shear strength τ, then by using A=F/ τ, we can back up the contact area, a typical JKR fitting curve has been shown in Figure 3.3.

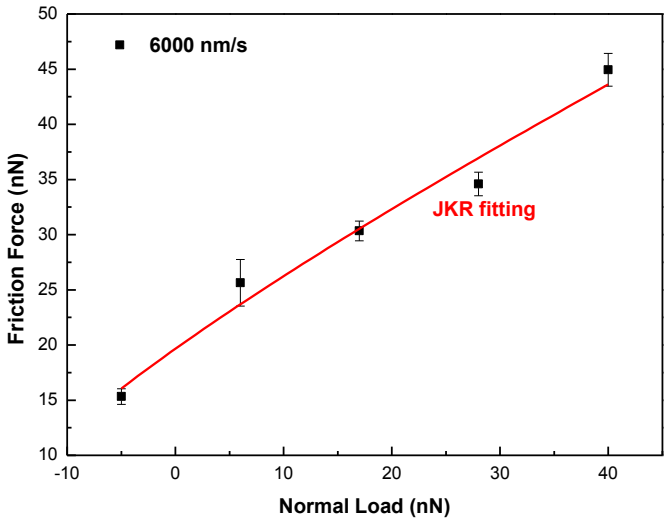

Figure 3.3 A typical JKR fitting curve which shows the relationship between friction force and normal load at 6000 nm/s.

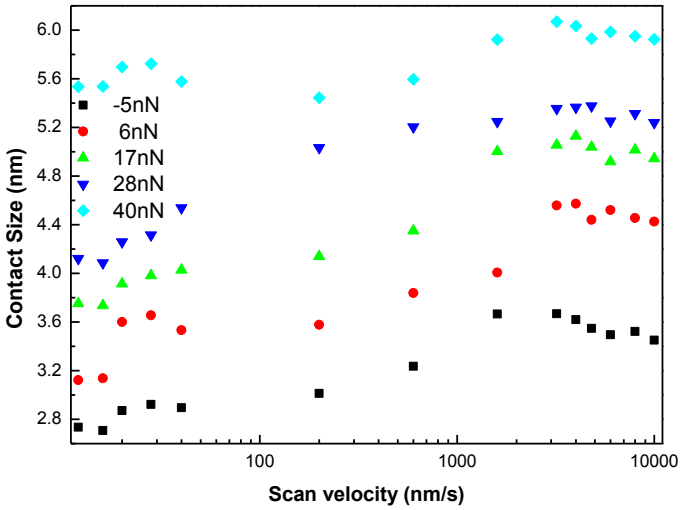

Figure 3.4 Contact size (calculated from the fitted free parameter P_1) fluctuates as a function of sliding velocity.

3.1.4. Modeling

During sliding contact, the two adjacent atomic planes have a spatially nonuniform distribution of relative lattice slip (or called disregistry field), Δ_α, with α =1,2 (i.e., the in-plane coordinates). The total potential energy Π is given as a functional of the interface slip field

$$\Pi = \Pi_0 + \int_S \Gamma\left(\Delta_\alpha\right) dS + \frac{1}{2}\int_S n_i \tilde{\sigma}_{i\alpha}\Delta_\alpha dS - \int_S n_i \sigma_{ia}^{elastic}\Delta_\alpha dS$$

Equation 3.4 The total potential energy equation.

where Π_0 is the potential energy of the elastic system when $\Delta_\alpha = 0$. The second term is the energy gained on the contacting interface S (with surface normal n_i) when slip develops, i.e., the γ surface. The interface constitutive law is defined by $\tau_\alpha = \partial\Gamma/\partial\Delta_\alpha$, e.g., $\tau_\alpha = \tau_{\max}\sin\left(2\pi\Delta_\alpha/b\right)$ with $\tau_{\max}$ being the theoretical shear strength of the interface. The third term is the energy change of the elastic solids outside the contacting interface due to the introduction of a nontrivial Δ_α (where the self stress $\tilde{\boldsymbol{\sigma}}$ arises from the nonuniform Δ_α when the externally applied force is zero). The last term is the interaction energy between the elastic stress field (when Δ_α =0) and the interface slip field. The equilibrium condition is attained when the total potential energy reaches a minimum, $\delta\Pi = 0$. As shown previously[92], the frictional behavior depends on the ratio of the contact radius *a* to the dislocation core size that scales as $\mu b/\tau_{\max}$. If $\tau_{\max}a/\mu b >> 1$, the sliding proceeds in the following manner: a dislocation loop nucleates at the contact edge, propagates towards and annihilates at the center, and then the indenter moves laterally by *b*. For a very large contact, dislocation nucleation from the contact edge is the same as that from a straight-front crack[99]. If the dislocation core size is larger than the contact size, $\mu b/\tau_{\max} > a$, there will not be sufficient space on the interface to develop the inhomogeneous slip, and thus the slip is uniform as assumed in the Tomlinson model. Between these two limits, sliding is thus facilitated by the gliding passage of dislocations with diffused cores on the interface – this corresponds to the friction force microscopy measurements.

The dependence of maximum friction force,

$$F_{fric} = F_L^{\max} = \pi a^2 \tau_{fric}$$

Equation 3.5 Frition force calculation equation.

on the applied normal force, F_N, arises primarily from the size dependence of τ_{fric} and the relationship between a and F_N. As a comparison, the contact size dependence of friction force is explained in the Tomlinson model by assuming a dependence of the potential amplitude on the normal load[91, 95]. In our model, the stick-slip behavior, as an instability phenomenon, can be observed regardless of a virtual point contact or multiple atoms in contact, as long as the interface stiffness, $2\pi\tau_{\max} a^2/b$, is noticeably larger than the stiffness $k_{eff} = \left(dF_L/d\delta_x\right)\big|_{\Delta_\alpha = 0}$, and the load drop, $\Delta F_{lateral} \approx k_{eff} b$, on the stick-slip curve is detectable on the $F_{lateral} \sim \delta_x$ curve. If the cantilever stiffness in lateral direction, $k_{lateral}^{cantilever}$ is comparable to the contact stiffness, then the friction stiffness is $k_{eff} = \left[1/k_{lateral}^{cantilever} + (2-\nu)/8a\mu\right]^{-1}$. Consequently, the transition from a smooth sliding to the stick-slip behavior observed in Socoliuc *et al*.[91] is believed to be primarily governed by $\tau_{\max} a/\mu b$ if cantilever stiffness is ignored, or by $\tau_{\max} a^2/k_{eff} b$, but not by the dependence of $\tau_{\max}$ on a.

A quantitative comparison to the temperature- and sliding-velocity-dependent experiments requires a mechanistic description of the rate-limiting processes and an accurate determination of the activation energy. In principle, the thermally activated process can be assessed by molecular simulations, which, however, spend most of the

calculation time on tracing the unimportant fluctuations near the metastable states since the jump between metastable states is a rare event. Analyses based on the Tomlinson framework implicitly assume a uniform slip, so that the dependence of the activation energy on the contact size and normal load cannot be determined. In our model, the energy functional in Eq. (3.6) allows a quantitative determination of the energy landscape with respect to the inhomogeneous interface slip field, and thus enables us to connect the macroscopic observations of velocity- and temperature-dependent frictional behavior to the detailed atomistic rate-limiting processes.

The activation energy is the difference in potential energy between the initial metastable (minimum energy) slip distribution $\Delta_\alpha^{\min}(x,y)$ and the saddle point slip distribution $\Delta_\alpha^{saddle}(x,y)$, $\Delta\Pi = \Pi\left(\Delta_\alpha^{saddle}\right) - \Pi\left(\Delta_\alpha^{\min}\right)$. Details on the simulation methodology can be found in our previous publications[92, 100]. In Gao's paper (2010), the following representation of activation energy is suggested,

$$\frac{\Delta\Pi}{\mu b^3} = \beta^* \left(1 - \frac{F_L}{A\tau_{fric}}\right)^{3/2}$$

Equation 3.6 Activation energy calculation equation.

When the contact size is small, we can assume a uniform interface slip, so that $\beta^* \approx 0.96\left(1 - F_L / \pi a^2 \tau_{\max}\right)^{3/2}$. At very large contact size, the activation energy required to thermally activate an incomplete dislocation loop from a straight-front crack. According to Rice and Beltz, we have $\beta^* \approx 10$. Numerical results in Figure 3.5 illustrate examples

of metastable and saddle point configurations on the *x*-*y* plane surface. Figure 3.6 gives the normalized activation energy, $(1-\nu)\Delta\Pi/\mu b^3$, as a function of $F_L/\pi a^2\tau_{\max}$ with $\tau_{\max}/\mu = 0.1$, and several representative values of a/b. These detailed calculations do not agree with the power-law form in Eq. (3.7); even when the contact size is small, the metastable configuration still exhibits spatial variation. Nevertheless, as the overall trend, with the increase of the contact size, the athermal friction stress decreases and the slope of the activation energy curve becomes significantly large.

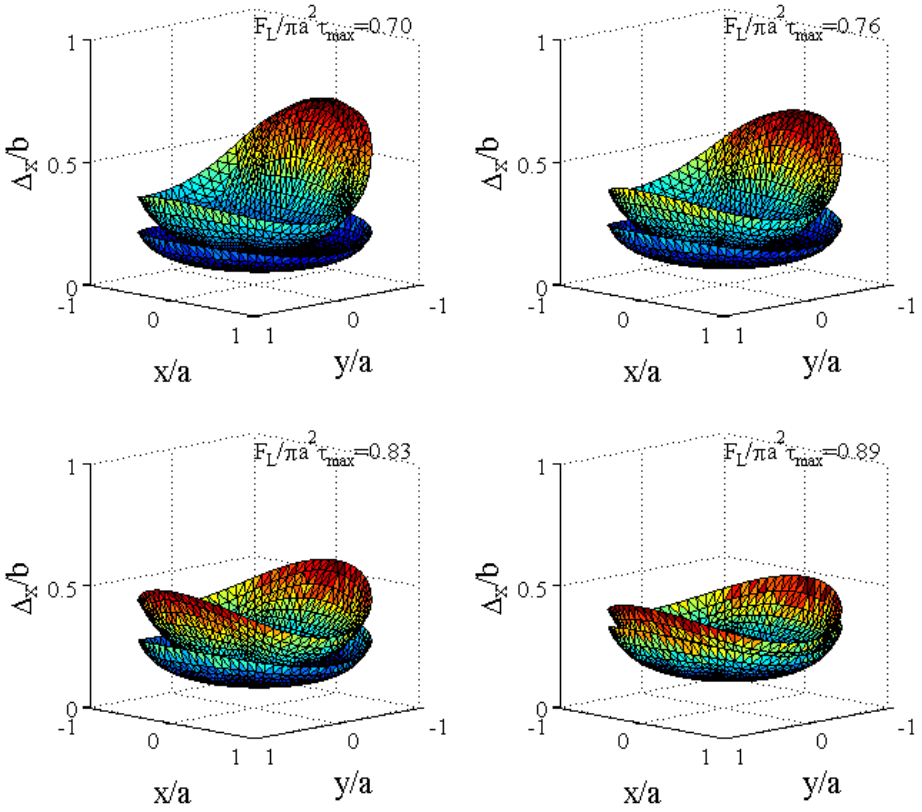

Figure 3.5 Stationary and saddle point configurations for $a/b = 10$, $\tau_{\max}/\mu = 0.1$, and several values of applied lateral force.

Assuming an Arrhenius law gives the transition rate $\dot{n}$ (i.e., the number of transitions per unit time per unit area on the interface), $\dot{n} = \dot{n}_0 \exp\left[-\Delta\Pi\left(F_L\right)/k_B T\right]$, where $\dot{n}_0$ is an attempt frequency per unit interface area, k_B is the Boltzmann constant, and T is the absolute temperature. In the transition state theory, the cumulative transition probability, *f*, obeys $\dot{f} = \pi a^2 \dot{n}\left(1-f\right)$. The measured friction force will have a Gaussian distribution, and the mean value corresponds to $d^2 f / dF_L^2 = 0$, given by

$$\frac{\mu b^3 \beta^*}{k_B T}\left(1-\frac{F_L}{F_{fric}}\right)^{3/2} + \frac{1}{2}\ln\left(1-\frac{F_L}{F_{fric}}\right) = \ln\frac{V_0}{V}$$

Equation 3.7 Friction V.S. scanning velocity.

where the scanning velocity is $V = d\delta_x / dt$ and $V_0 = \frac{2\pi^2 \dot{n}_0 k_B T \tau_{fric} a^4}{3 k_{eff} \beta^* \mu b^3}$. Note that $\dot{n}_0\left(a\right)$ may also be dependent on the contact size, consequently, besides the contact size dependence of $\tau_{fric}\left(a\right)$ in the Tomlinson-Rice transition, the thermally activated friction has additional area dependence from the activation energy $\Delta\Pi\left(F_L; a\right)$ and the availability of attempt sites.

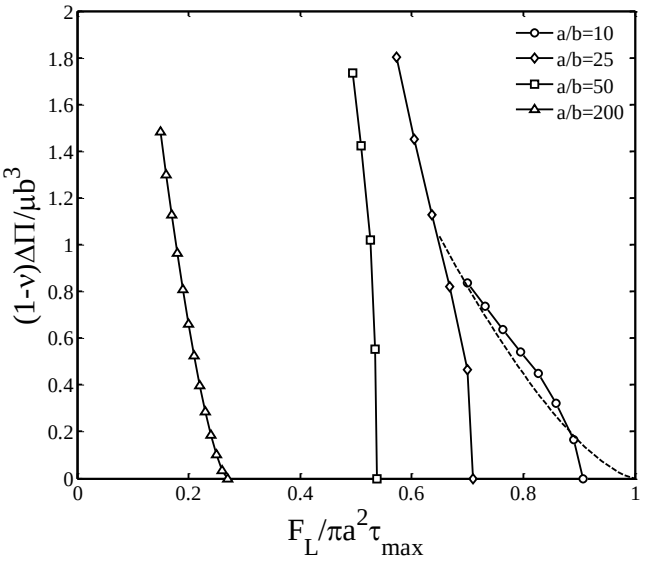

Figure 3.6 Activation energy as a function of the applied shear stress, with the increase of contact size, the activation energy increases rapidly as the applied shear force is lower than the athermal limit.

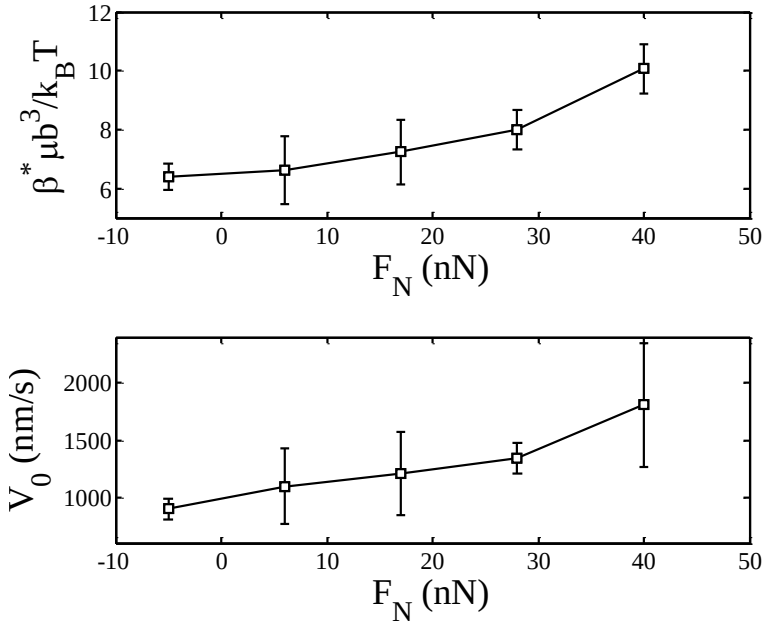

Figure 3.7 Fitted prefactor of the activation energy and characteristic velocity from experimental data in Fig. 1. Despite the lack of the relationship between F_N and

contact size, it is found that the activation energy increases rapidly as the contact size increases.

3.1.5. Conclusion

In summary, we have developed a Peierls-type mechanistic study to elucidate the atomic frictional behavior from the initiation and spatiotemporal evolution of interface defects and lattice slip. Particularly, we find the temperature- and velocity-dependence of frictional behavior from the connection between activation energy calculations and spatially nonuniform rate-limiting processes.

3.2. Tunable Friction between Graphene Layers

3.2.1. Introduction

Graphene, as a two dimensional (2D) hexagonal lattice of carbon atoms, is the building block for the formation of 3D graphite. Graphene can thus be expected to inherit the excellent friction properties from graphite which is a widely used solid lubrication materials[101]. Graphene is also considered as a potential candidate for next generation applications in nanoelectronics and miniaturized devices due to its fabulous electronic transport properties[102]. However, due to their large surface area to volume ratio, most nanoelectronics devices are susceptible to stiction and wear. Therefore, an effective approach to tune the friction at the nanoscale is highly demanded in order to integrate graphene into nanoelectronic devices.

It is not surprising that a number of ways to tune the friction have been proposed over the last few decades. The ultralow friction was revealed by shearing atomically sharp tips over an atomically flat surface[103]. When the normal load acting on the tip decreases below a critical threshold, the characteristic stick-slip instabilities cease to exist and sliding occurs smoothly without abrupt jumps. A second way to obtain nearly vanishing friction has been demonstrated: dry friction decreases when the sliding speed is reduced below a critical velocity that increases with temperature[104]. This effect is called ‘thermolubricity’ which is related to thermally activated jumps occurring in the contact area[105]. In addition, a term called ‘superlubricity’ that means sliding with negligible friction was coined by Hirano *et al*.[30], who started it from Aubry’s original ideas. This prediction describes that the friction would vanish when two surfaces in

contact are laterally stiff and incommensurate. Mate *et al*. performed the first atomic-scale friction experiment by sliding a tungsten tip over a HOPG surface under ambient conditions[106, 107]. They found the friction coefficients between 0.005-0.015 and an almost linear dependence of the friction force on the normal load. By controlling the relative angles of individual nanoflakes to achieve a suitable lattice mismatch, thus incommensurate contact, an almost frictionless sliding was demonstrated for dry and wearless tip-surface contact. Besides, Dienwiebel *et al*. have observed that the ultra-low friction coefficients of graphite, discovered in FFM experiments are also caused by 'superlubricity' between graphite surfaces[108].

3.2.2. Experimental Details

In order to study the friction force between graphene and graphite, we have developed a novel AFM probe, which enables tracking of the real contact between two graphene layers. A few layers of graphene were grown on nickel microspheres by CVD method[109]. Specifically, the commercially available nickel microspheres were placed dispersed onto an oxidized Si substrate (300 nm oxide thickness). The prepared samples were placed on an aluminum oxide boat in a CVD chamber filled with a 1:2 mixture of H_2 and Ar at a total gas flow rate of 200 sccm at a pressure of 2660 Pa. As the Ni microspheres have been exposed to the environment in the course of experimentation, a native oxide layer would invariably by present. The native oxide sheath was first reduced by heating the sample in this ambience at 1023 k for 600 s, before introducing a timed burst (flow rate of 1sccm) of ethylene (C_2H_4) as the carbon containing precursor, in addition to the H_2/Ar flow. The precursor feeing time, typically in the order of a few to tens of seconds, determines the number of layers of graphene grown. The sample was

then cooled to room temperature within 300 s in a flow of 133 sccm Ar at 2660 Pa chamber pressure. The 1023 K annealing/growth temperature had been optimized to avoid morphological changes to the nickel microsphere at higher temperatures while maintaining the growth of highly crystalline graphene layers that is not achievable at lower temperatures.

A graphene wrapped nickel microsphere was glued on a tipless Si_3N_4 AFM probe using epoxy under micromanipulator. The schematic diagram of our experiment is depicted in Figure 3.8. We determined the lateral spring constants of the Ni microsphere probe to be k_L= 0.017 N/m and the normal spring constant of 0.21 N/m. The friction measurements were performed on HOPG, which possesses a lateral grain size of up to 5 mm. The graphite was freshly cleaved using scotch tape. A cross was carved on the freshly cleaved HOPG surface by a razor blade as the reference line. A series of angle change in small step were accomplished in a small region in the HOPG. The angle change was tuned in the almost same position by identifying the surface geometry, which was to make sure the angle dependence friction testing occurred in the same grain. Two representative images with different relative scanning angles in the similar scanning region were shown in Figure 3.9, while the white angle illustrates the angle between the scanning direction and the HOPG surface reference line. The AFM (Pico-plus, Agilent AFM, Tempe, Arizona) scans were performed with progressively decreasing normal load for every 20 scans or so, this was done to measure the encountered friction force as a function of the applied normal load. The scanning directions were tuned in small steps with respect to AFM probe during the measurement. For each orientation, we measured the friction forces at a range of constant normal load (20 nN to 32 nN). The test was run

with a scan size of 10 nm at scan speed of 12 nm/s. Raman spectroscopy was performed on a Reinshaw Raman microscope using a 633 nm HeNe Laser on AFM graphene/nickel microsphere right before and after friction test in order to confirm the survival of graphene layers. SEM imaging was performed on FEI Quanta 400 ESEM FEG microscope.

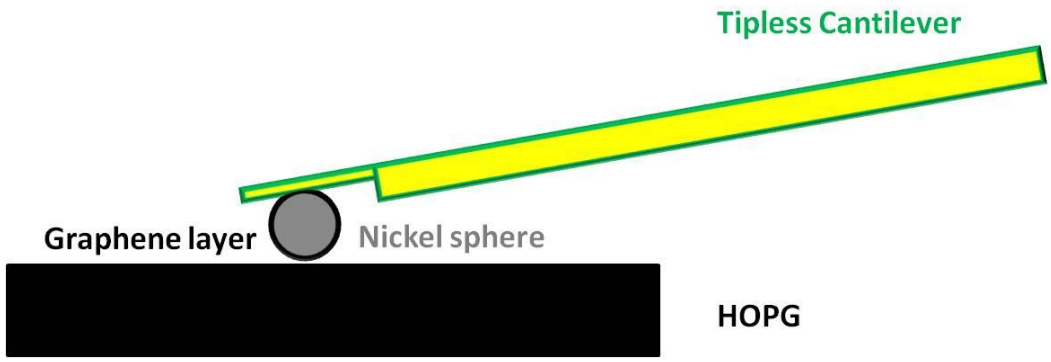

Figure 3.8 Schematic diagram of graphene layers sliding on graphite surface.

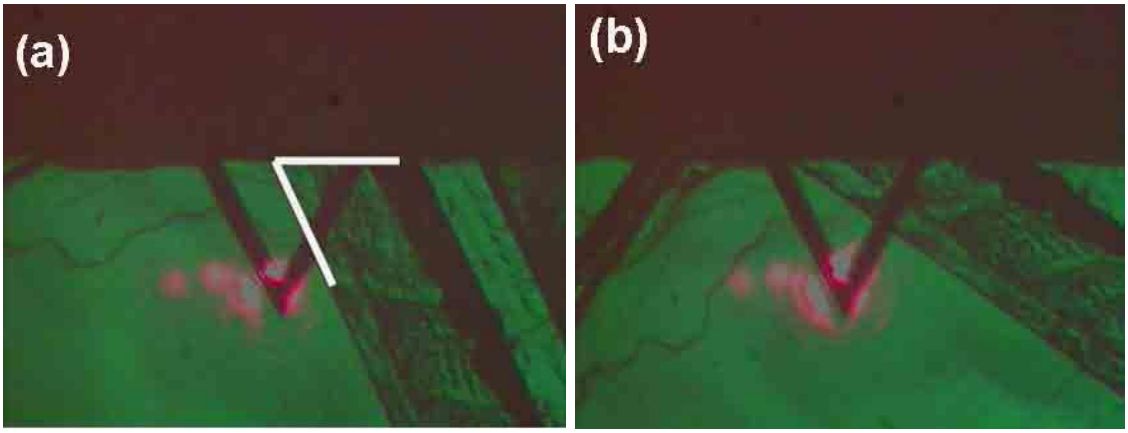

Figure 3.9 Representative optical images of scanning direction relative to the surface reference line.

3.2.3. Results and Discussion

SEM was employed to image the AFM probe structure and graphene wrapped nickel microsphere morphology (Figure 3.10(a)). The diameter of the microsphere is estimated to be 7.5 μm as shown in Figure 3.10(a) inset. It is worthy to notice that there are some bumps under high magnification though it looks smooth under optical microscopy. The high resolution SEM image in Figure 3.10(b) shows that the grain size of graphene ranging from 400 nm to a few microns in diameter, which is dictated by the grain size of nickel sphere. Raman spectra has been accomplished on the probe surface right after the microsphere attachment in Figure 3.11, which reveals the successful graphene growth on the nickel surface. In order to demonstrate the survival of the graphene layers after the friction experiment, another round of Raman spectrum was collected on the exact same position. It was found that the characteristic peaks remain in the same position except for a little change in G band (1580 cm^{-1}) intensity.

The frictional behavior as a function of applied normal load obtained from the friction force microcopy experiment for graphene sliding over HOPG surface was shown in Figure 3.12. The friction force shows an almost linear load dependence on these two graphene surface with the ultralow nominal friction coefficient estimated to be 0.02. Although the data do not point clearly in the direction of a power-law behavior $F_{friction} \propto F_{\alpha N}$, it is clear that if any such law was to be estimated, it would have $\alpha<1$. This is at variance with previous findings for a sharp undeformable tip-surface contact, and with recent studies of the sliding of hydrogen-passivated carbon. In the similar normal load range, the measured average friction force is about one order of magnitude higher than the other superlubricious graphite[30]. The proposed reason for this discrepancy is the

contact size difference. According to Hertzian contact theory, the mathematical relationship between indenter load P, indenter radius R, contact area a, and the maximum tensile stress σ_{max}. The contact radius depends upon the load, the indenter radius, and the elastic properties of both the specimen and the indenter according to Eq. (3.8):

$$a^3 = \frac{3PR}{4E*}$$

Equation 3.8 The contact radius calculation equation.

where E* is the combined modulus of the indenter and the specimen given by Equation (3.9):

$$\frac{1}{E*} = \frac{(1-\nu^2)}{E} + \frac{(1-\nu'^2)}{E'}$$

Equation 3.9 The combined modulus calculation equation.

Material	Poisson's ratio	Young's modulus (GPa)
HOPG	0.012	36.5
Nickel	0.31	200

Table 3.3 Material properties of contacting surface between HOPG and Nickel sphere.

The elastic modulus was calculated to be 31. 3 GPa, according to Eq. (3.9) and Table 3.3. In our experiment, the tip-surface contact area estimated from the Hertz model is 300 to 1000 nm^2 within the range of loads applied in the experiments (10 nN to 70 nN) because 7.5 μm microsphere in diameter was used, while the tungsten tip merely has a contact area ranged from 13 to 44 nm^2 because of the tip radius of 80 nm. In our opinion, the friction between graphene layers originates from the interlayer interaction. Based on previous theoretical studies, the interlayer friction properties between a graphene flake and an infinite graphene sheet is described by an empirical registry-dependent potential, which demonstrates the friction between graphene sheets with commensurate or incommensurate interlayer stacking increases with decreasing interlayer distance. It is partially support that the friction force increases with the increasing normal load.

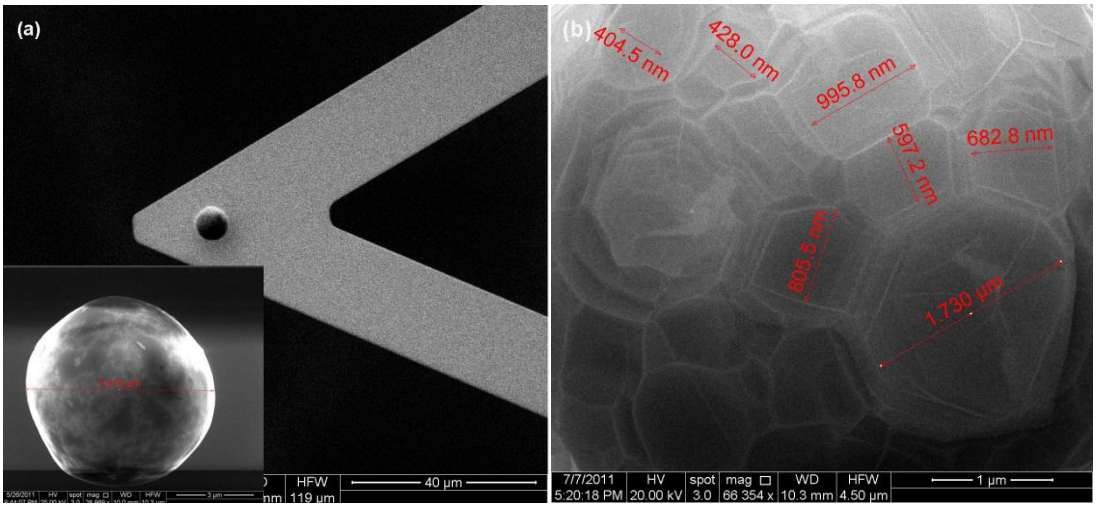

Figure 3.10 (a) SEM image of graphene wrapped nickel microsphere AFM probe, the bottom inset shows the size of microsphere and surface morphology, (b) high resolution SEM image of the grain size measurement of graphene on nickel sphere.

The periodicity of the graphite substrate lattice cannot be recognized in the force variations due to the bluntness of probe as shown in Figure 3.13(d)-(f). The FFM measurements were made under precisely the same conditions for Figures 3.13(a), (b) and Figure 3.13(c), but the graphite rotated 6° anticlockwise and 25◦ clockwise. The rotation has induced the average friction force to reduce one order of magnitude to 1.00 ± 0.28 nN. This variation was repeated when rotating the graphite sample in the opposite direction reduced the average friction force to 3.80 ± 0.66 nN. The area enclosed in the complete loop corresponds to the energy dissipated irreversibly during the loop, and the area divided by twice the loop width is the average, dissipative friction force. Several experiments and calculations have been probing the effects of lattice mismatch on friction, showing that incommensuracy often prevent global ingraining of large areas, thus attenuating the consequent strongly dissipative stick-slip motion. Theoretically, atomic-scale friction on ideal solid surfaces is often described by simple balls-and-springs models such as the Tomlinson model, where a single atom, or a more structured tip, is dragged through a spring along a static periodic potential energy surface.

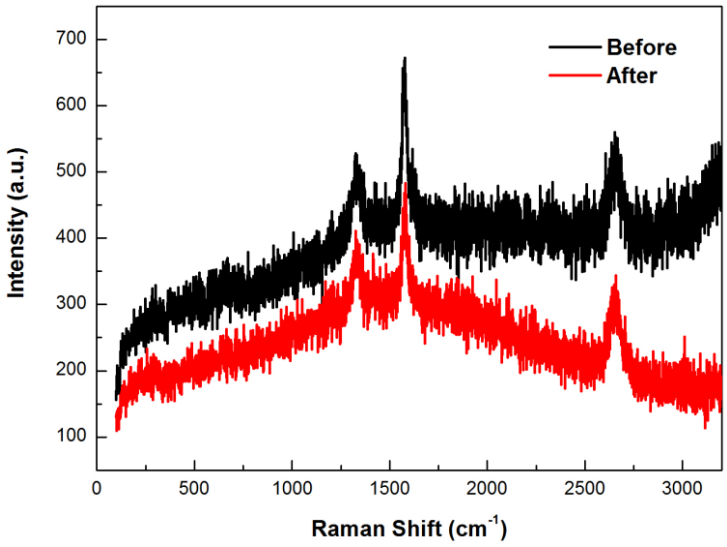

Figure 3.11 Raman spectra (excitation at 633 nm) of graphene wrapped microsphere right before and after friction tests.

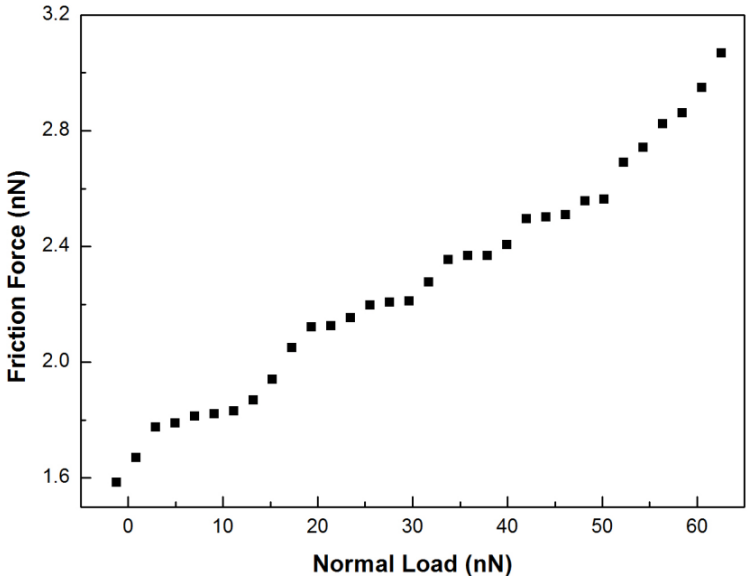

Figure 3.12 Friction vs. applied load for graphene sliding on HOPG.

The average friction forces measured of 140 ° sample rotation angles was listed in Figure 3.14. Two peaks were able to be recognized, while the distance between the two friction peaks is roughly 60 °, which corresponds well with the 60 ° symmetry of individual atomic layers in the graphite lattice. As shown by experiments, friction is maximum at a highly commensurate contact ($\theta=0^{\circ}$) and decreases rapidly as the HOPG rotates to incommensurate stacking. Friction force decreases by nearly one order of magnitude from the high friction $\theta=0^{\circ}$ commensurate angle to the low friction $\theta<60^{\circ}$ incommensurate one. This drop is smaller than was found by experiment, where it exceeded significantly one order of magnitude. In order to exclude instrumental artifacts, the friction values in Figure 3.14 were always measured for the same sliding direction

with respect to the substrate. The lattice related orientation variation in the friction force and the near varnishing of friction for most orientations constitute firm evidence of superlubricity between the AFM tip and the graphite lattice.

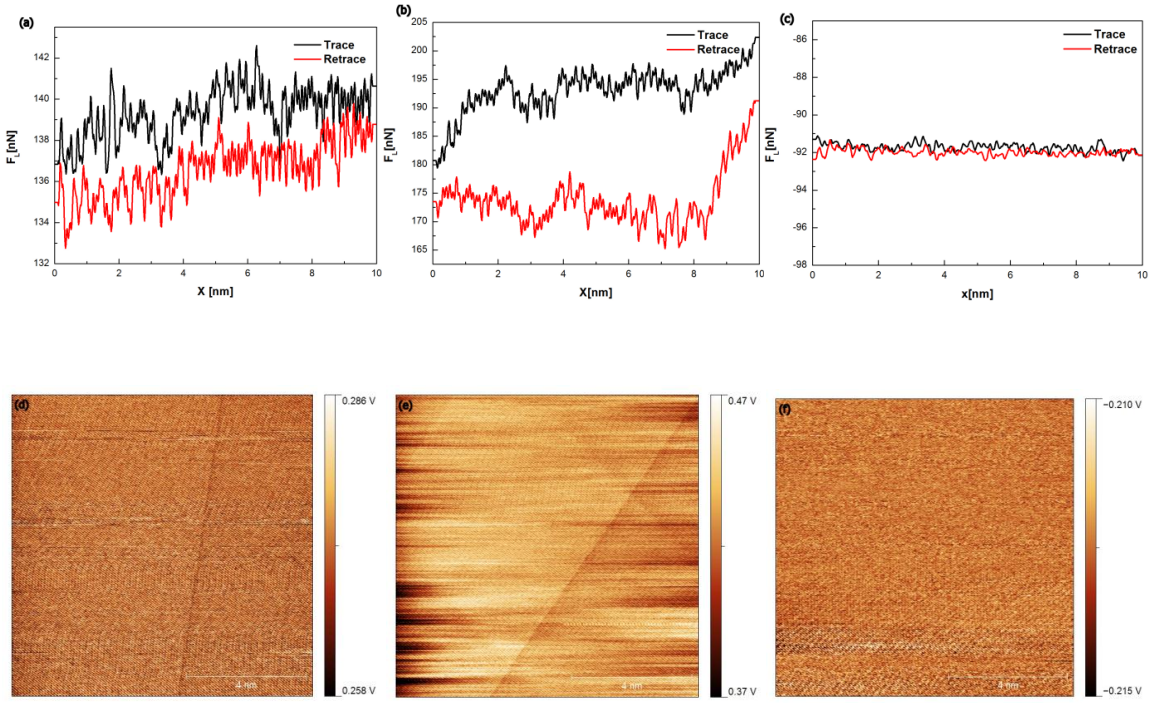

Figure 3.13 Friction loops (black, trace; red, retrace) and lateral force image (trace), measured along the relative scanning direction orientation angles of 66 ° (a), (d) (Normal force F_N= 20 nN); 60 ° (b), (e) (F_N=26 nN); 85 ℃), (f) (FN=30 nN). Image size is 10 nm ×10 nm.

Other graphitic systems have been found that show remarkable nanotribological properties, which might be attributed to superlubricity. Our results might explain the very low interwall friction between nested CNTs, observed in TEM experiments. In most cases, the inner and outer tubes in a multiwall CNT form an incommensurate graphitic system, similar to a few layer graphene that slides over a graphite surface.

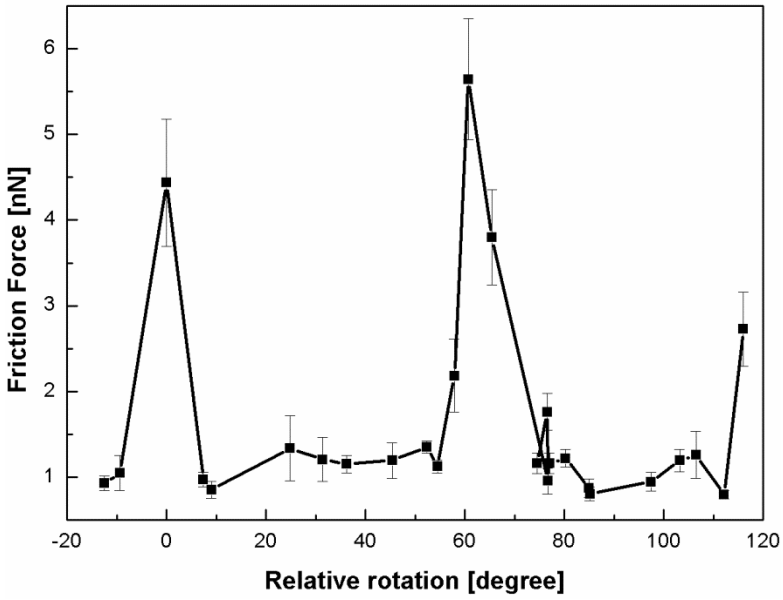

Figure 3.14 Average friction forces versus rotation angle of the HOPG sample surface. Two peaks of high friction were observed with the interval of 60 degrees.

3.2.4. Conclusion

Using a robust CVD technique, thin layers of graphene with relative large grain size were grown on the nickel microsphere surface, as evidenced by the high resolution SEM image and Raman spectra. The graphene wrapped Ni microsphere was attached onto a tipless AFM probe for friction forces detection between graphene and HOPG surface. We have studied the energy dissipation between a few layer graphene sliding over a graphite surface. By measuring atomic-scale friction as a function of the rotational angle between two contacting bodies, we show that the origin of the ultralow friction of graphite lies in the incommensurability between rotated graphite layers, an effect proposed under the name of “superlubricity”. Two narrow peaks of high friction were

observed at 0 and 60◦, respectively. Between these peaks a wide angular range with ultralow friction close to the detection limit was found.

Chapter 4

4.In situ Characterization of Interfacial Facture Toughness of Carbon Nanotube Reinforced Polymer Derived Ceramics Composite

4.1. Introduction

CNTs reinforced ceramic nanocomposites are being very actively pursued as potentially strong, tough, and lightweight materials in the last two decades[3, 110-113]. Intuitively, nanocomposites have a much larger fiber/matrix interface area, and much stronger, more-flexible reinforcements that could improve strength and toughness simultaneously, compared with traditional carbon fiber reinforced composites. However, it is disappointing to notice that only little or no improvement have been reported in CNTs/ceramic composite materials[114, 115], presumably due to the inhomogeneous dispersion of CNTs in the matrix and the poor interfacial connectivity between two phases[116]. Furthermore, whether composite fracture and damage mechanics at the

nanoscale differs from that at the micron-scale due to the near-atomic-scale is simply unknown.

The toughening mechanisms of composites by micron-scale reinforcing fibers are now well established[117]. The first key characteristic is crack deflection at the fiber/matrix interface, which is observed by investigating cracks that grow transverse to the axial direction of the fibers. The fibers actually weaken the composite such that crack propagates easily. In addition, the fiber bridging of cracks that propagate perpendicular to the axial direction of the fibers is another hallmark. The fiber bridging force resulting from debonding and sliding resistance makes a great contribution to the strength and toughness. The third key characteristic is fiber pullout on the fracture surface, which demonstrates that the bridging fibers eventually fail away from the crack plane. The energy consumed by pulling the embedded fibers out against any residual frictional stresses at the interface would be a major contribution in improvement of fracture toughness of the brittle material. Only a few efforts have been devoted to understanding the CNTs/ceramics interface in the fracture process. Xia *et al*. directly observed the toughening mechanisms in CNTs alumina matrix composite by introducing controlled cracks under SEM[118]. Additionally, Yamamoto *et al*. claimed that MWCNTs broken in the outer shells and then the inner core was pulled away, leaving fragments of the outer shells in the alumina matrix[116]. And he also suggested that the use of MWNTs having a much higher load carrying capacity may lead to composites with higher fracture toughness[116].

4.2. Single fiber pullout

Mechanical properties of fiber-reinforced composites depend on not only the properties of the fibers and the matrix but also the fiber/matrix interfacial properties, which have a complex structure. Typically, in composites, the constituents do not dissolve or merge completely, and therefore, exhibit an interface between one another, which can be considered as a different material with different mechanical properties. The interfacial properties are determined by the material properties such as the adhesion of the fiber surface to the matrix, as well as the volume fraction. Therefore, the knowledge and understanding of the nature and mechanics of load transfer between the nanofiber and matrix and properties of the interface is critical for the manufacturing of mechanically superior carbon nanofiber-based composites, and will enable in tailoring of the interface for specific application or superior mechanical properties. One of the most important properties of the interface in a composite is the interfacial strength. Several techniques for measurement of interfacial strength, such as single fiber pullout or pushout, fragmentation, and Raman Spectroscopy, were used before. Among these techniques, single fiber pullout is preferred technique for interface characterization, because it provides a direct estimate of the interfacial strength. An advantage of the pullout test is that in addition to the interfacial bond strength and interfacial toughness, other interfacial properties such as the matrix shrinkage pressure on the filler, the interfacial shear stress and the work done in pulling out the filler from the matrix, can be determined. The last factor is important, since the significant increase in fracture toughness of fibrous composites has been attributed to the fiber pullout process during failure.

4.3. Experimental Methods

MWCNTs were from Mitstui Corp., Japan, and lot No. 05072001K 28. The PDC precursor was prepared by mixing CSO-230 and CLC-PL005 platinum catalyst at a weight ratio of 100:1 (Extreme Environment Materials Solutions, LLC, and Saratoga Springs, NY). *N*-methylpyrrolidone (NMP) was from Alfa Aesar, Ward Hill, MA. Glycerol, isopropanol, trimethyl aluminum, and HPLC grade water were from Sigma Aldrich, St. Louis, MO. All materials were used as received without further purification.

A spring like "push-pull" mechanism functioned micro-device which consists of three moveable shuttles attached to each other via inclined freestanding beams is shown in Figure 4.1. The pullout specimens used in this study are comprised of individual MWCNTs embedded in polymer derived ceramics films. The PDC precursor was prepared by mixing CSO-230 and CLC-PL005 platinum catalyst at a weight ratio of 100:1. A thin fresh layer of viscous PDC precursor was first deposited on a small portion of sample stage shuttle. A droplet from the sonicated suspension of the MWCNTs in toluene was then dropped onto a Si wafer coated with a 5 nm thick layer of titanium. Individual nanotube of 100-300 nm diameter and 10-15 μm long was subsequently picked up and placed across the shuttles using micromanipulators housed within a probe station (The micromanipulator Co., Carson City, NV) under an optical microscope. The embedment length of the MWCNT was measured at this point by observation within a SEM. The micro-devices after sample loading were heated on a hot plate at 393 K for 1800 s, following a robust pyrolysis procedure for ceramics formation. Specifically, the devices were placed in a tube furnace, and ramped at 10 K/min to 1273 K for 1800 s. The furnace atmosphere was controlled by blowing the forming gas (95% Ar and 5% H_2) at

1000 cm^3/min. The formed ceramic $Si_xC_yO_z$ embedded one segment of the MWNT; the other end was subsequently clamped onto the device by electron beam induced deposition of platinum within a FIB chamber (FEI HELIOS 600). This process results in some Pt deposition on the exposed regions of the single MWNT, which naturally acts a geomorphic marker for pullout observation.

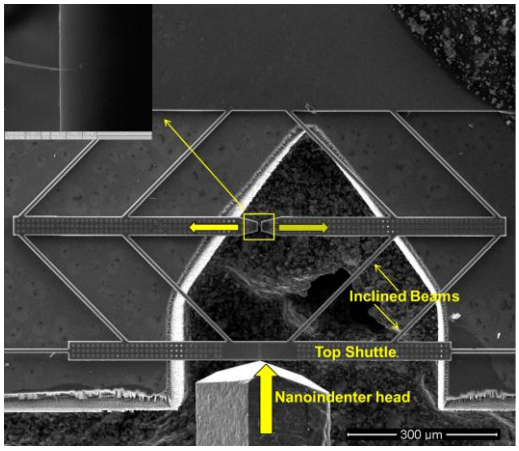

Figure 4.1 SEM micrograph of a micro-fabricated device to perform the pullout experiments, and yellow arrows show the direction of movement of the indenter and the shuttles.

The pullout experiments of MWNTs were conducted within a SEM (FEI Quanta 400 high resolution field emission scanning electron microscope, FEI Company, Hillsboro, Oregon) equipped with an InSEM Indenter (AGILENT Technologies, Oak Ridge, Tennessee) system. A blunt Berkovich nanoindenter tip was used to apply load at a displacement rate of ~20 nm/s. The electron beam was focused on the MWNT specimens to monitor their pullout from the matrix in real time. During the experiment, the maximum load applied to the device ranged from 100 µN to 400 µN. After each

experiment, the pullout MWNTs length was quantified again to confirm all embedded sample was pulled out rather than fractured inside the matrix.

4.4. Results and Discussion

Application of μN-level loads resulted in the pull-out of the MWNT specimens from the ceramics matrix, as observed in the SEM snapshots extracted from the video recording of an illustrative test shown in Figure 4.2. A MWNT specimen of 102 nm in diameter with 6.14 μm embedded depth was gradually pulled out from the ceramic matrix. It was observed that interface failure initiates at the tube entry point and develops into an interfacial crack which propagates along the embedded tube length. The diameter difference of the MWNT before and after applying load is due to the atom diffusion when Pt deposition. Load applied to the samples and the sample displacements were derived from the nanoindenter load and the displacement data using a simple response subtraction method and image correlation techniques10. Figure 4.3 provides a representative load-displacement plot. Essentially, it is observed that the response before reaching the maximum load was linear.

MWNTs-PDC matrix interface is characterized by the critical shear stress needed to debond the interface and the possible subsequent shear resistance for a relative sliding of MWCNTs and ceramics. When the maximum shear stress reaches the interface shear strength (IFSS) τ_b, the debonding at the MWNT-PDC interface occurs, and then the MWNT is pulled out. Assuming perfect interfacial bonding and uniform shear stress distribution (i. e. no shear lag), the corresponding critical load is

$$F_{max}^{\tau} = \tau_b . \pi D L_{emb}$$

Equation 4.1 The critical load calculation equation.

where D is the diameter of the MWNT, and L_{emb} is the embedded depth in the matrix. The pullout force values that used to calculate the IFSS were listed in Table 4.1. It is observed that IFSS exhibits significant scatter and its average value of 61.0 ± 20.0 MPa reaches the theoretical τ_b between MWNT and ceramics reported in the range of 1-40 MPa by Li *et. al* [119]and is the highest value reported in literature.

Another approach for nanotube/ceramics composite interface failure analysis is the calculation of the interfacial fracture energy release rate. This failure criterion is based on the energy balance before and after interfacial failure. Jiang and Penn has developed a fracture mechanics model that the total energy is comprised of the strain energy in the non-embedded region of the tube and in the debonded portion, the work of friction, as well as the interfacial fracture energy[120]. The strain energy that is assumed to be used for finite size crack advancement occurring simultaneously with frictional energy dissipation at the interface was released at the instant of interfacial crack propagation by neglecting the thermal effect.

The expression relates the critical load for interfacial crack advancement, *Pc* to geometrical parameters (*r, R, l*) and the elastic constant (E_f, E_m, v_m) of the nanotube and the matrix to the maximum interfacial fracture energy rate, *Gc*:

$$G_c = \frac{{P_c}^2[1 + csch^2\left(\frac{nl}{r}\right)]}{4\pi^2 r^3 E_f}$$

Equation 4.2 The maximum interfacial fracture energy rate calcualtion equation.

where n is a utility constant defined as $\sqrt{\frac{E_m}{E_f(1+\nu_m)\ln(\frac{R}{r})}}$, the subscript f and m denote the tube and the matrix, respectively, R denotes for the radical distance from the tube axis at which the shear stress in the matrix reduces to zero, l is the embedded length, a is the initial crack length at the interface, r stands for the MWNTs radius.

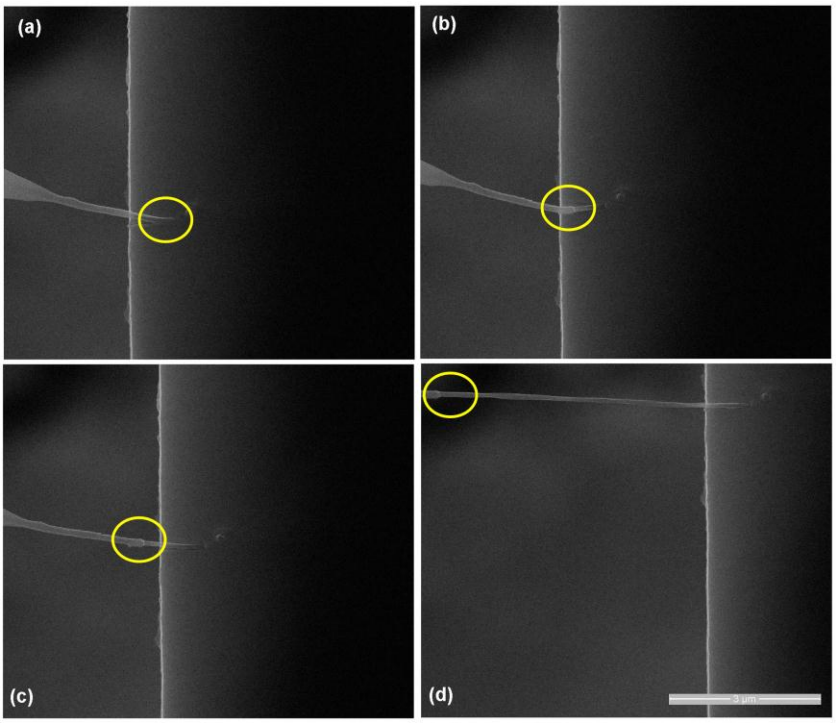

Figure 4.2 SEM snapshots showing a single MWNT as it pulls out of a ceramic matrix at (a) t=0, (b) t=20s, (c) t=57s, and (d) t=306s, respectively. The experiment was conducted at an indenter displacement rate of 20 nm/s, and the yellow circle indicates the onset of MWNT pullout.

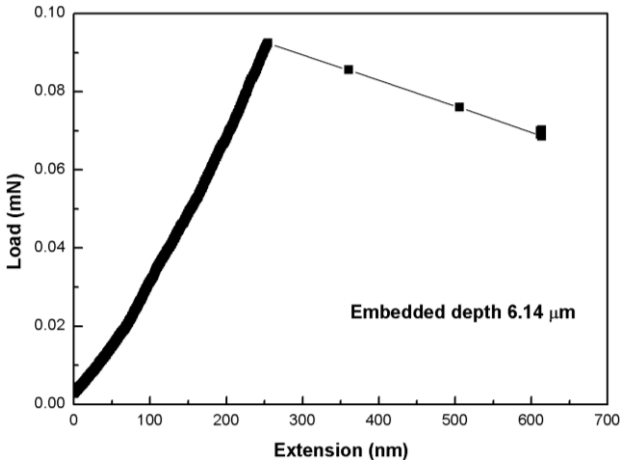

Figure 4.3 Representative load-extension curve for a specimen with 6.14μm embedment.

The critical load for interfacial crack advancement is simply taken as the pullout force. E_f was found to be equal to 200 GPa[121], and the average value E_m was found to be 78 GPa. The Poisson's ratio of the PDC was set equal to 0.2. The diameter of the MWCNTs was calculated as 174 ± 88 nm. The initial crack length, *a*, was equal to zero at the critical load, and the pull-out process proceeded catastrophically without measurable frictional force. The stress transfer parameter R/r value ranging from 2 (a value typical for weak interfaces) to 9 (a value that would be typical for a strong interface)[122, 123]. Eq 2 provides an interfacial fracture release rate value for the MWNTs-PDC interface within the range of 5.0-44.5 J/m^2. The large deviation originates primarily in variability in nanotube diameter rather than the choice of the value of the stress transfer parameter *R/r* (we used the average *R/r*=6 for the calculation).

Some enhancement in the critical pulling force such as due to the radical compressive stress applied to MWNTs during high temperature ceramic pyrolysis and the

formation of interfacial phase between CNTs/PDC is expected for the high value of fracture energy release rate. The previous effort on interfacial fracture energy release rate has been focused on CNTs/polymer composite. Ganesan *et al.* quantified the interfacial fracture energy value for the pristine MWNT-Epon 828 interface within the range of 0.05-0.25 J/m^2[121]. The range for nanotube pull-out from a polyethylene-butene matrix was reported in 4-70 J/m^2[124].

Embedded depth (nm)	Outer diameter (nm)	Critical pull-out force (mN)	IFSS τb (MPa)	Fracture energy release rate (J/m2)
3870	186	0.163	72.0	22.58
4913	295	0.380	83.5	44.48
4945	114	0.073	41.7	4.997
6138	102	0.092	46.8	6.416

Table 4.1 Interfacial properties Obtained from single MWNT Pull-out Experiments.

4.5. Discussion

A novel technique which involves the usage of delicate micro-devices plus a quantitative nanoindenter system was used to perform in situ single MWNT pullout experiments in order to study the interfacial properties of a MWNT-polymer derived ceramics nanocomposite. Several successful pullout experiments allowed us to measure the interfacial fracture energy for the pristine MWNT-PDC interface. With regard to the

pristine MWNT-PDC interface, the interfacial fracture energy values were found to be considerably higher than those reported earlier for similar systems and those associated with conventional engineering composite systems.

Chapter 5

5.Mechanical Characterization of Individual Functionalized Carbon Nanofibers

5.1. Quantitative *In-situ* Mechanical Characterization of Effects of Chemical Functionalization on Individual Carbon Nanofibers

5.1.1. Introduction

The high strength-to-weight ratio combines with superior stiffness have made CNFs the material of choice for high performance composite structure in aerospace, defense, and other industries. The fact that CNFs can be produced in large quantity and at low cost is particularly attractive for these applications compared to carbon nanotubes. However, the challenges associates with CNFs dispersion and poor load transfer between CNFs and matrices have been a bottleneck for the development of CNFs based composite structures. One popular approach to address these issues and to improve the properties of CNFs based composites is to chemically modify the nanofiber surface with functional

groups. Therefore, an in-depth understanding of the structure and mechanical properties of the functionalized CNFs at a single fiber level would be a critical step to improve their integration into different matrices. Nevertheless, the mechanical properties of individual functionalized CNFs have not been systematically explored.

Due to the lack of structural perfection and the existence of a complex hybrid structure[110, 125], it is extremely difficult to obtain theoretical prediction for CNFs strength without extensive simplifications and assumptions[126]. Furthermore, owing to the small sample size as well as the magnitude of the forces and the deformation involved, quantitative mechanical measurements of individual CNFs are considered extremely challenging. The most popular approach to these measurements is atomic force microscope (AFM) based bending test and many attempts have already been made to measure the elastic moduli of CNFs in this manner. The Young's modulus of a suspended CNFs rope was determined to be 400 GPa by Kim *et al*.[127] Lawrence *et al*.[128] and Zhang *et al*.[129] obtained the elastic modulus of individual CNFs to be in the range of 6-207 GPa and the average tensile modulus of single-walled carbon nanotube bundle to be 265 GPa by using the similar technique. Furthermore, Zussman *et al*.[130] reported the mechanical properties of solid electronspun polyacrylonitrile (PAN)-derived CNFs: the failure stress of CNFs varied from 0.32 to 0.90 GPa and the average Young's modulus was 63±7 GPa. In addition, Inaba *et al*. found the Young's modulus to be 38-48 GPa for CNFs probes fabricated by the argon ion bombardment of carbon coated silicon cantilever[131]. However, the limitation of AFM based testing, such as poor accuracy and reproducibility, greatly hampers the mechanical measurement of individual CNFs.

MEMS offer a promising class of very small actuators and diagnostic tools for stretching nanomaterials under various mechanical and electromechanical loading conditions. The individual pristine, high temperature heat-treated and graphitized/surface oxidized vapor grown carbon nanofibers (VGCNFs) were evaluated for their elastic modulus and tensile strength by Ozkan *et al*. using a MEMS loading platform[132]. They claimed that the VGCNFs with diameters of the order of 150-300 nm had high tensile strengths between 2.74 GPa and 3.34 GPa, and Young's modulus between 180 GPa and 245 GPa. In addition, with the aid of the same MEMS system, Arshad *et al*. quantified the average tensile strength and the elastic modulus of the individual solid electrospun PAN-derived CNFs carbonized at 1673 K to be 3.5 ± 0.6 GPa and 172 ± 40 GPa, which were 6 and 3 times higher than the previous reports, respectively[130, 133, 134]. The electrospun CNFs is solid in the inner structure while the functionalized CNFs in this report are mostly hollow.

5.1.2. CNFs Functionalization and Characterization

In a typical fluorination process[135], 1.75 g of commercially available pristine CNFs (Pyrograf®-III, batch PR-19-XT-PS from PPI, Cedarville, Ohio) was loaded into a custom-built fluorination apparatus. The chamber was purged with the flow of helium while the temperature was ramped to 428 K. At this temperature, the fluorination was carried out for 16 hours by passing a 10% fluorine-90% helium gas mixture over the CNFs in the chamber. The unreacted F_2 gas was absorbed into a trap containing aqueous solution of KOH. After cooling to the room temperature, 2.16 g of the fluorinated CNFs were produced, which resulted in the covalent addition of about 25wt% of fluorine on CNFs surface.

Amination of CNFs was carried out by analogy with the amino functionalization of fluorinated CNTs[136]. 2.0 g of fluorinated CNFs, 20 cm^3 of ethylenediamine, and 200 cm^3 of DMF were placed into a 500 cm^3 three-neck flask, equipped with the thermometer and condenser, and then 1 cm^3 of pyridine was added. The mixture was stirred overnight at 363 K under nitrogen. After cooling down to the room temperature, the mixture was filtered through a 220 nm Teflon membrane (Millipore, Billerica, MA) and the residue on the membrane washed with ethyl alcohol, then dried overnight at 343 K in vacuum oven. As the result, 1.85 g of amino-functionalized CNFs was prepared.

In order to confirm the effective functionalization by fluorination and subsequent amination, and also to evaluate the concentration of the fluorine and amino groups on CNFs surfaces, the bonding nature of carbon in functionalized CNFs, and finally the effects of fluorination and amination on CNFs structures, a series of careful investigations utilizing attenuated total reflectance Fourier transform infrared spectroscopy (ATR-FTIR), X-ray photoelectron spectroscopy (XPS) and Raman spectroscopy, Thermogravimetric analyzer (TGA), X-ray diffraction (XRD) were conducted. ATR-FTIR spectra were collected using a Ge crystal attachment at Nicolet 4700 spectrometer. XPS measurements were made using a PHI 5700 with Al Kα X-rays (1486.6 eV) at a maximum pressure of 5.33 x 10^{-6} Pa. Raman spectroscopic measurements were collected with a Renishaw 1000 microraman system operating with a 532 nm laser source. TGA was performed in flowing air on a TA Instruments Q500 by heating the sample from 293 to 1273 K using a ramp rate of 10 K/min. XRD patterns of powder samples deposited on a zero-background quartz crystal plate were collected on a Siemens D5000 using a Cu Kα source (λ=0.154 nm).

The ATR-FTIR spectroscopy provided information on structural nature and vibrational properties of functional groups covalently bonded to CNFs surface (Figure 5.1). In the ATR-FTIR spectrum of fluorinated CNFs (Figure 5.1(a)) the highest intensity band at ~1200 cm^{-1} characterized the stretching modes of C-F and CF_2 groups, while the band at ~700 cm^{-1} belonged to deformation modes of these groups. The medium intensity band at ~1560 cm^{-1} was related to activated C=C stretching mode of the CNFs surface. Such spectroscopic "fingerprints" were similar to those observed in fluorinated carbon nanotubes[135, 136]. The ATR-FTIR spectrum of amino-functionalized CNFs sample (Figure 5.1(b)) showed a broad band centered at ~3070 cm^{-1} which was crucial for identification of NH and NH_2 groups (N-H stretches). Deformation modes of these groups appeared in this spectrum at ~1560 and ~1520 cm^{-1}, as well as twisting mode at ~714 cm^{-1}. Weaker bands near 2830 cm^{-1} characterized C-H stretches and broad band at ~1100 cm^{-1} has been associated with the C-C and C-N stretches of the ethylenediamino groups bonded to CNFs surface. In comparison, the FTIR spectrum of pristine CNFs (Figure 5.1(c)) did not show a distinct features of surface bonded and IR active groups.

We also compared the results of TGA study of three types of CNFs. The complete weight loss of pristine CNFs due to thermal oxidation of CNFs and volatilization of products was observed above 873 K. For fluorinated CNFs, the weight loss of ~28% was observed to take place in the temperature range of 523-823 K. From previous studies of other fluorinated carbon materials, such as graphite and carbon nanotubes, it was known that fluorocarbons eliminated fluorine groups in the form of CF_4 and COF_2 molecules (when air is present). Taking this into account, the weight content of fluorine groups in the CNFs was calculated as ~24.7%, which was in good agreement with the observed

weight gain of ~25-26% occurring after fluorination of CNFs. In comparison, amino-functionalized CNFs exhibited weight loss of about 20% in a narrow temperature range of 453-523 K, which was similar to carbon nanotubes that were also functionalized with ethylene diamine through reaction with fluorinated derivatives. Elemental analysis by XPS showed atomic concentration (at%) on the surface of functionalized CNFs as follows: fluorinated CNFs, C (50.8), O (4.2), F (45.0); amino-functionalized CNFs, C (70.0), N (13.3), O (7.6), F (9.1). The covalent bonding of fluorine to the CNFs was evidenced by observation of the F1s peak in the XPS spectra at binding energies of 687.4-687.8 eV which is typically observed for fluorine covalently bonded to carbon.

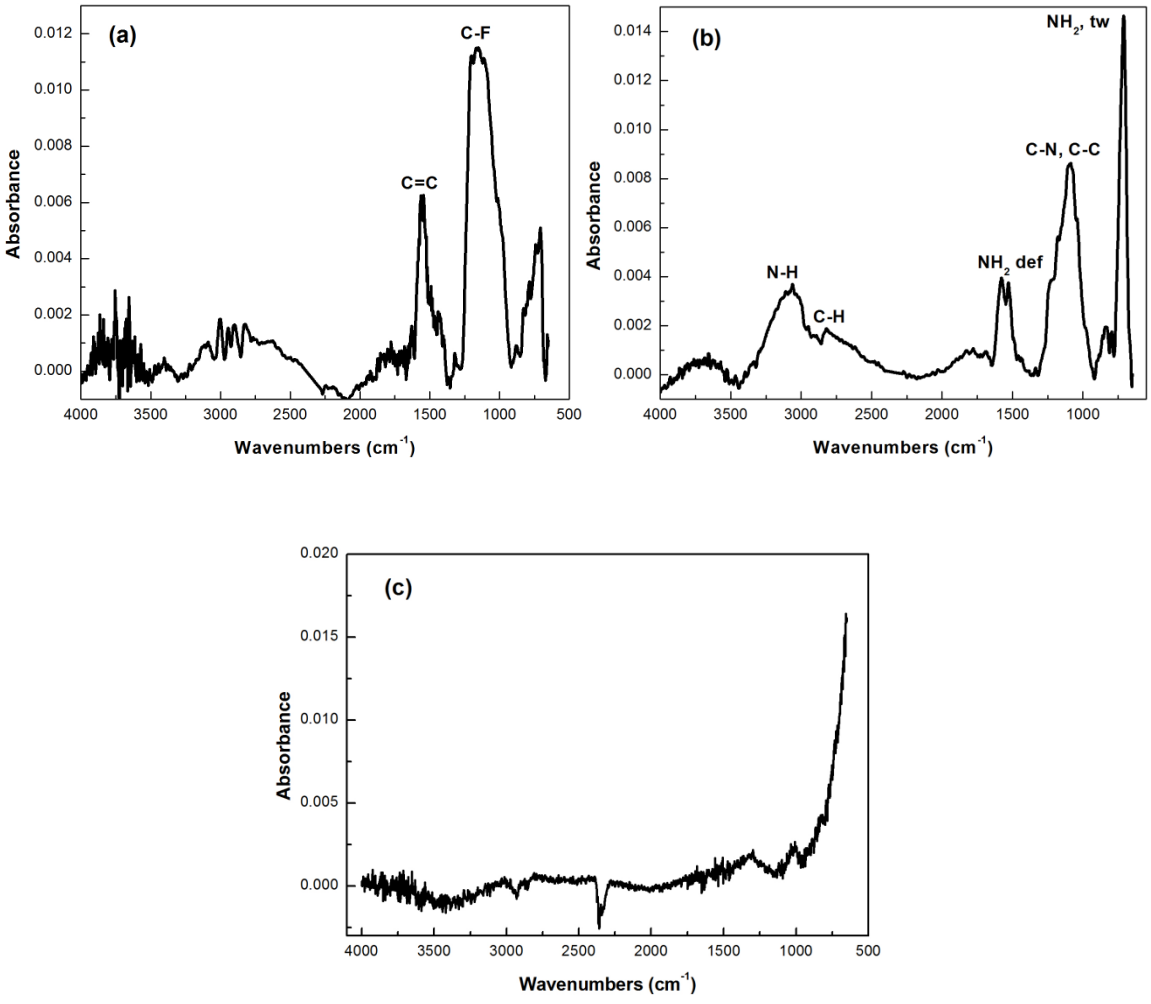

Figure 5.1 (a) ATR-FTIR spectra of fluorinated CNFs (a), amino-functionalized CNFs (b) and pristine CNFs (c).

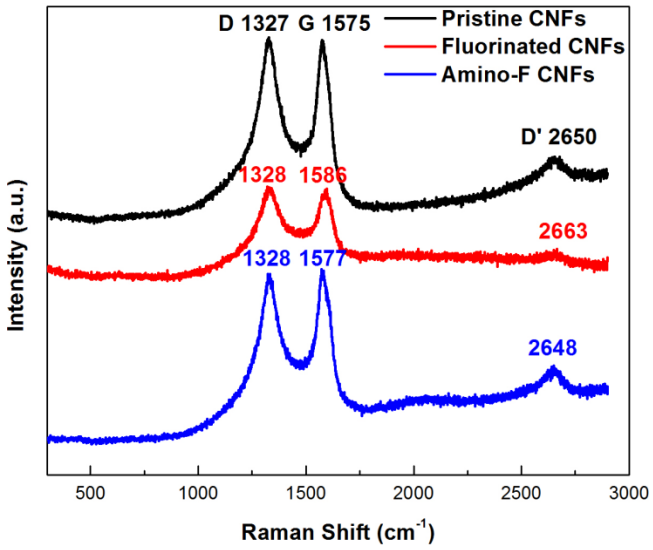

Figure 5.2 Raman spectra of pristine, fluorinated and amino-functionalized CNFs.

Raman spectroscopy provided essential information to evaluate the bonding states of carbons in the fiber structure changed by fluorination and amination. The Raman spectra collected from the pristine, fluorinated as well as the amino-functionalized CNFs were shown here (Figure 5.2). In the spectrum of the pristine CNFs, a strong and sharp peak at 1575 cm^{-1} (G band) corresponded to the in-plane stretching vibration of the sp^2 carbon-carbon bonds within the ordered graphitic layers of fibers, while another strong peak at 1327 cm^{-1} (D band) was related to the defects in the graphene structure. A weaker peak at 2650 cm^{-1} (D' band) reflected the boundary point K in Brillouin zone of graphite and was dependent upon the packing in three-dimensional space[137]. For the fluorinated CNFs, the Raman "red shift" in G (1575 cm^{-1} to 1586 cm^{-1}) and D' (2650 cm^{-1} to 2663 cm^{-1}) bands occurred due to the difference in microstructure, such as the interlayer

distance. Another thing worth mentioning was that the D' shift could be due to the introduced compressive force on the fiber surface[52], which was also evidenced by TEM images later. In comparison, the G and D' bands shifted back to pristine fiber's positions after grafting amino functional group.

Significant changes in the structure of CNFs caused by the functionalization were detected through XRD measurements. As comparison of XRD patterns (Figure 5.3), the fluorination of CNFs caused the appearance of a very broad new feature in the XRD of the fluorinated CNFs centered at 2θ= 13.5°, as found by the curve-fitting analysis, in addition to a typical graphite (002) peak at 2θ= 26.32°. Based on XPS surface analysis, the outer layers of the fluorinated CNFs were built from fluorographene layers of C_1F_1 composition. According to the calculation from XRD value of interlayer distance, these layers were separated by d-spacing equal to 0.657 nm which matched the interplanar d-spacing in fluorographite $CF_{1.12}$ (0.57-0.66 nm), indicating strong repulsive interactions between curved fluorographene layers in fluorinated CNFs.

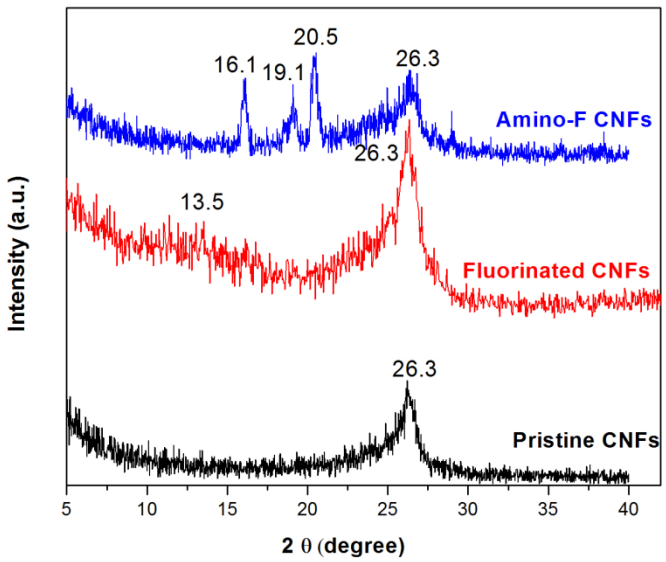

Figure 5.3 XRD patterns of Pristine, Fluorinated, and Amino-functionalized CNFs.

XPS data also showed that although reaction of fluorinated CNFs with ethylenediamine resulted in grafting of $–NHCH_2CH_2NH_2$ groups to the surface of CNFs, complete removal of fluorine did not take place, so about 9 at% fluorine still remained bonded in the structure. Nevertheless, such defluorination of the fluorinated CNFs produced a significant decrease of interlayer spacing since stoichiometry of fluorographene layers in amino-functionalized CNFs became reduced from C_1F_1 to approximately C_5F and below, as calculated from XPS elemental analysis data. It was witnessed by complete disappearance of a low angle peak observed on the fluorinated CNFs and appearance of new sharp peaks at 2θ= 16.14, 19.1, and 20.48°, along with the peak of neat CNFs at 2θ= 26.32° (Figure 5.3) which corresponded to d-spacing of 0.535, 0.464, 0.433, and 0.338 nm, respectively.

5.1.3. Tensile testing technique

The details about the micro-device fabrication using standard photolithography techniques were discussed earlier[138]. In conjunction with a quantitative nanoindenter within an SEM/TEM chamber, the micro-device was employed to perform *in situ* tensile tests on 1-D nanoscale specimens[138-141]. A thin fresh layer of epoxy (HARDMAN Water-Clear Epoxy) was first deposited on a small portion of sample stage shuttle. A droplet from the sonicated suspension of the CNFs in toluene was dropped onto a Si wafer coated with a 5 nm thick layer of titanium. Individual nanofiber of 200-250 nm diameters was subsequently picked up and placed across the shuttles using

micromanipulators housed within a probe station (The micromanipulator Co., Carson City, NV) under an optical microscope.

Uniaxial tensile experiments of individual pristine, fluorinated and amino-functionalized CNFs were conducted within a SEM (FEI Quanta 400 high resolution field emission scanning electron microscope, FEI Company, Hillsboro, Oregon) equipped with an InSEM Indenter (AGILENT Technologies, Oak Ridge, Tennessee) system (see Figure 5.4). A blunt Berkovich nanoindenter tip was used to apply load at a displacement rate of ~20 nm/s. The maximum load applied to the device ranged from 0.3 mN to 0.5 mN. After each experiment, both ends of the ruptured CNFs were imaged by SEM at higher magnification to identify the fracture mode. Since it was not always possible to accurately measure the inner radius of the hollow CNFs, our analysis employs solely the outer CNFs diameter to estimate the nominal fiber strength. Due to the relative low stiffness of epoxy clamps, the displacement of the deformable epoxy clamps during testing need to be carefully considered. To ensure the accuracy of displacement measurement, a digital image correlation method was utilized, and all results reported in this work have been corrected by this technique.

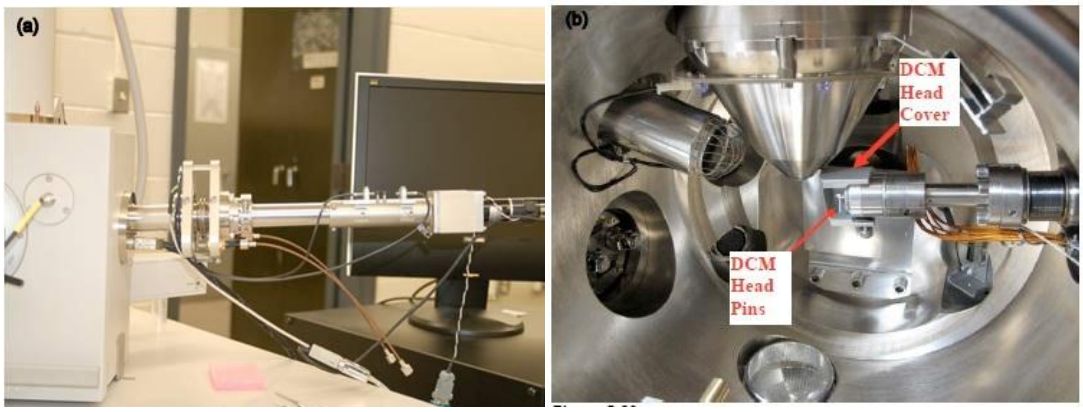

Figure 5.4 (a) Image show InSEM^{TM} indenter extension axis and (b) nanoindenter module within SEM chamber, DCM head cover and head pins for protection of indenter.

5.1.4. Mechanical Testing Results and Discussion

With the successful functionalization of CNFs by fluorine and amino groups along with the corresponding chemical characterizations completed, quantitative *in situ* tensile testing method as described was employed to investigate the mechanical consequences of such chemical treatments on individual CNFs. At least 10 samples for each type of CNFs were successfully tested and the deformation and fracture of individual CNFs were closely monitored by real time SEM imaging. A simple micro-fabricated device (see Figure 5.5) that works in conjunction with a quantitative nanoindenter within an SEM/TEM chamber was used to perform *in situ* tensile tests on functionalized CNFs. Loads applied to the samples and the sample elongations were derived from the nanoindenter load and the displacement data using a simple response subtraction method and image correlation techniques[139]. The SEM snapshots of the pristine, fluorinated and amino-functionalized CNFs during tension and after failure (Figure 5.6) as well as the selected stress versus strain curves of three different types of CNFs (Figure 5.7) exhibit an initial gradual change in the fiber stiffness. It is due to the fiber waviness in its natural state after sample mounting, and the sample would need to be first pulled straight before any load application can occur. The rest of stress-strain curves show a typical linear elastic deformation behavior observed in carbon nanotubes and similar 1-D nanomaterials. It is evident that the strength of fibers increased dramatically after the fluorination but dropped back to the similar level as the pristine CNFs after

further partial defluorination and grafting of ethylenediamino functional groups (Table 5.1). These obtained strength values also compare favorably with the limited data available in the literature from direct measurements of individual CNFs[132].

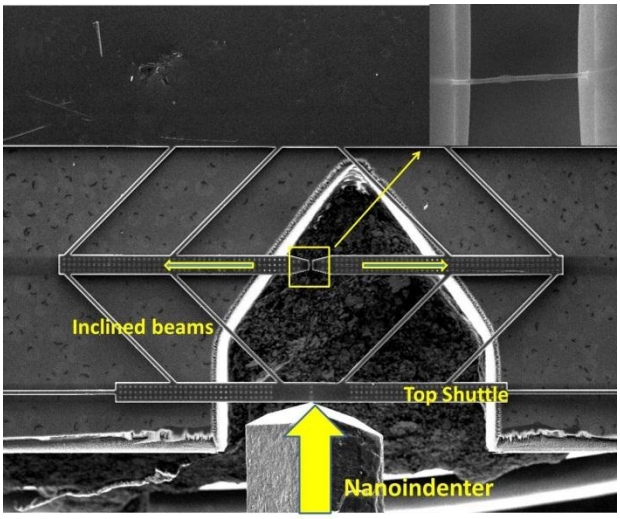

Figure 5.5 SEM image of the *In situ* tensile test platform: block arrows show the direction of movement of the indenter tip and the shuttles during the experiment; (Inset) close up view of rectangle region showing a CNFs specimen across the sample stage shuttle gap.

Due to the stochastic nature of the mechanical properties measured for CNFs, a probabilistic analysis using two parameter Weibull cumulative probability density function was applied to evaluate the tensile strength of CNFs:

$$P_f(\sigma) = 1 - \exp(-(\frac{\sigma}{\sigma_0})^m)$$

Equation 5.1 The Weibull probability function.

where σ, is the applied stress resulting in a probability of failure, $P_f(\sigma)$, m is the Weibull modulus, which provide a measure of the scatter in the strength data, and σ_0 is the material stress parameter. The Weibull parameters were computed by the method reported by Klein. Specifically, ranking the failure stresses (σ_i) in the ascending order (i=1, 2,…n) and assigning probabilities of failure according to P_i=(i-0.5)/n, where n is the number of broken specimens, are the initial task to estimate the cumulative failure probability from the available failure-stress data. Subsequently, a linear curve fitting with a logarithmic axis was performed for data collected from all three types of CNFs to obtain the corresponding Weibull parameters as listed in Table 5.1.

In the study of Endo *et al.*, the majority of fiber strength values for VGCNFs diameter between 300-1000 nm are in the range of 500-1000 MPa, and the mechanical strength of VGCNFs is found to be inversely related to the diameter size[142]. The trends proposed by them could predict the higher strengths measured in this study, in which the size of three types of CNFs ranged between 200 and 250 nm. Compared to the pristine CNFs, the other two functionalized CNFs have relatively small Weibull moduli which indicate the presence of a broader spectrum of flaws[143]. The characteristic strength of the pristine CNFs is 2.10 GPa compared to 3.05 GPa for the fluorinated CNFs, see Table 5.1. The negative effect of partial defluorination and further amino functional group grafting on the average CNFs strength is evidenced by the fact that the characteristic strength decreases significantly to 1.94 GPa, even lower than that of the pristine CNFs. The great decrease of characteristic strength reveals a dramatic increase in the average size of the catastrophic flaws after amnino functionalization. On the other hand, the greater variability of the strength and the smaller Weibull modulus for the fluorinated

CNFs suggest that the fluorination increases the randomness in the distribution and variability of flaw size. Finally, the elastic modulus measured for different CNFs samples follow the similar trend. These results are comparable with the elastic modulus of amorphous and hollow CNFs based probes calculated to be 42GPa[131].

Sample	Diameter (nm)	Modulus, m	Strength, σ_0 (GPa)	E (GPa)	Strength (GPa)	Strain
Pristine CNFs	210±30	3.39	2.10	25.8±3.3	1.89±0.66	0.063±0.021
Fluorinated CNFs	221±25	2.83	3.05	45.8±10.2	2.67±0.94	0.057±0.015
Amino-F CNFs	215±38	3.13	1.94	31.6±13.8	1.75±0.68	0.053±0.013

Table 5.1 Weibull parameters, elastic moduli and mean strength as well as strain for three types of CNFs.

(a) Pristine CNFs

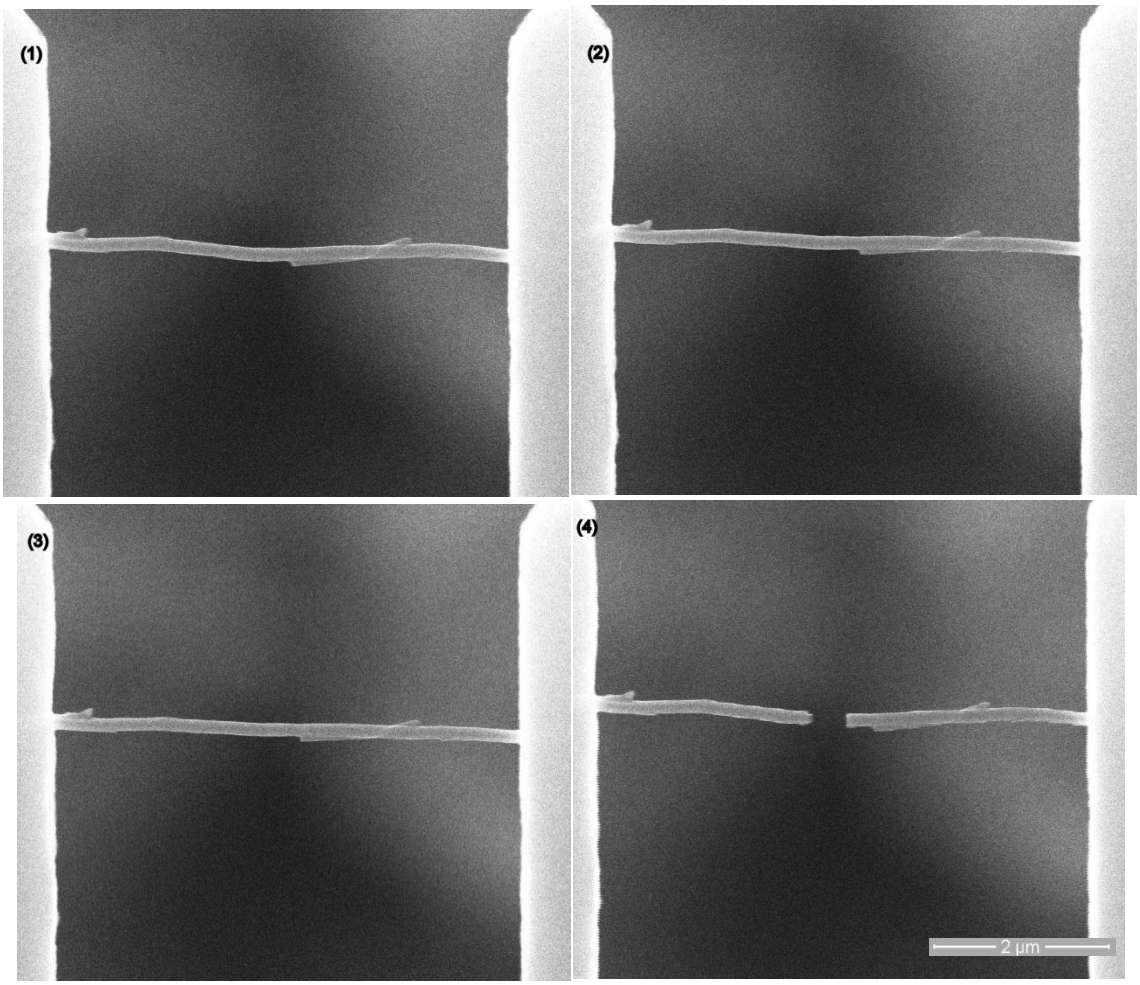

(b) Fluorinated CNFs

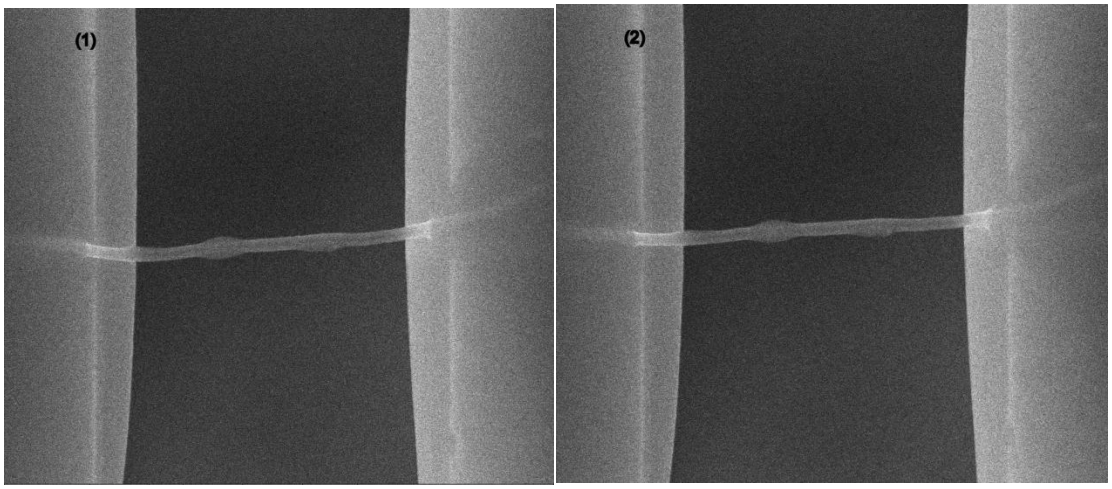

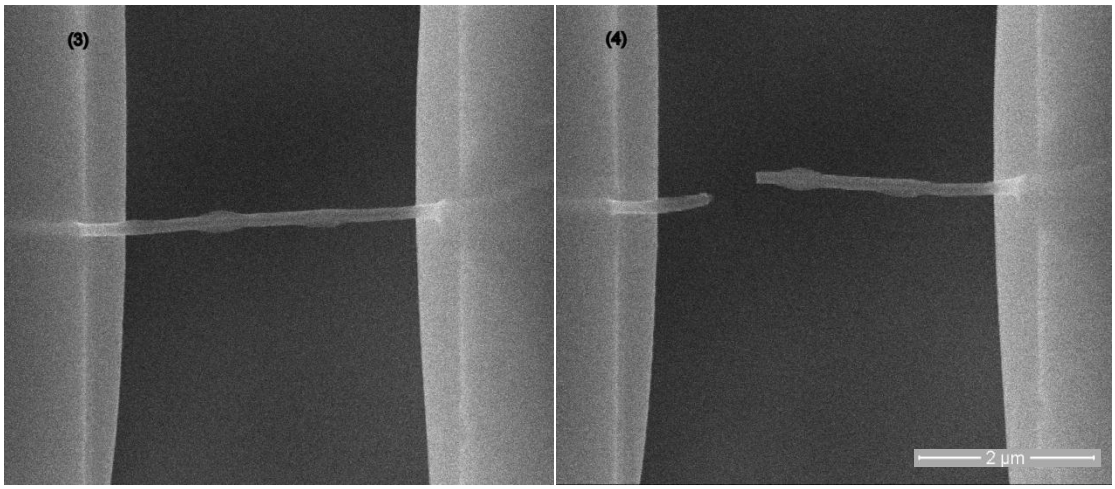

6) (c) Amino-Functionalized CNFs

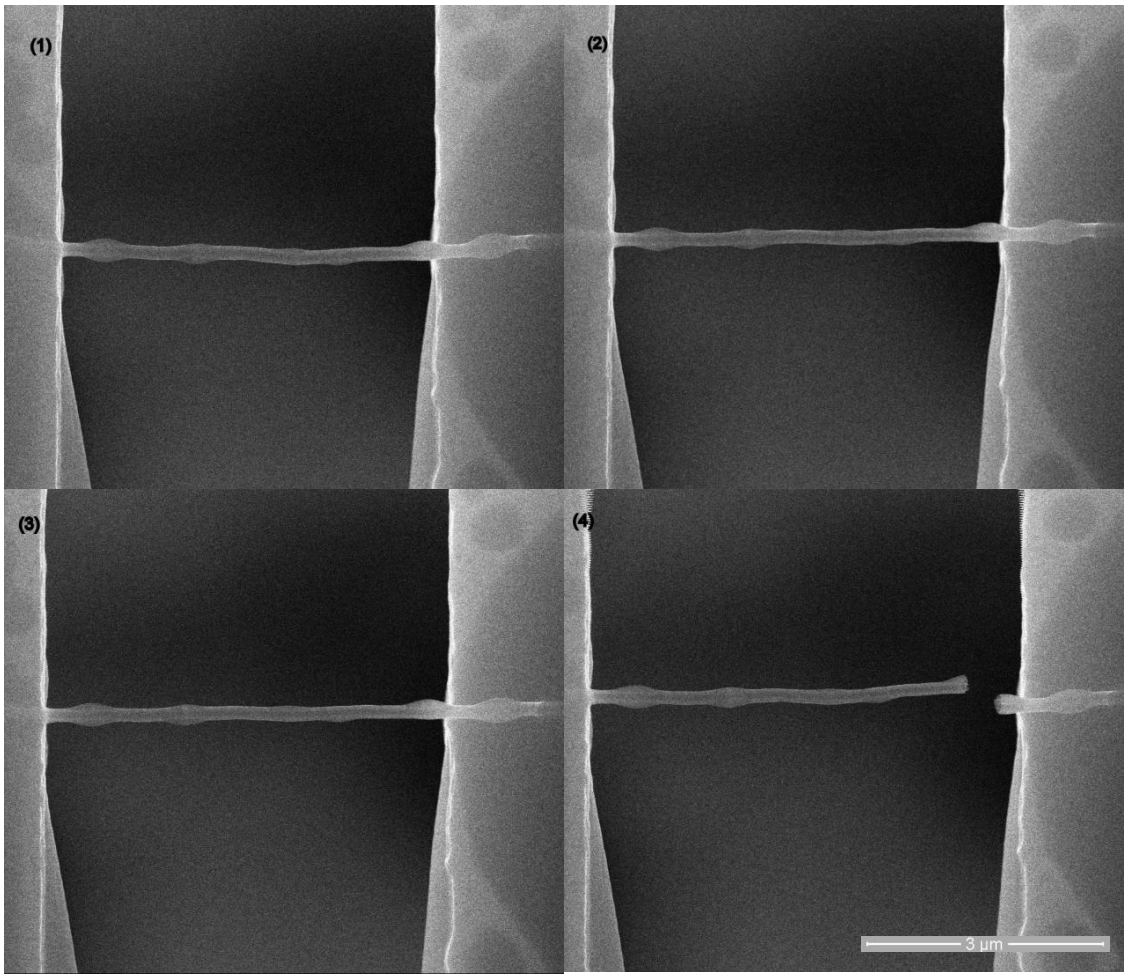

Figure 5.6 (a) SEM Snapshots show a pristine CNFs specimen undergoing deformation and failure under a tensile test at (1) t=0, (2) t=10, (3) t=19, (4) t=30s. (b) SEM Snapshots show a fluorinated CNFs specimen undergoing deformation and failure under a tensile test at (1) t=0, (2) t=27, (3) t=61, (4) t=99s. (c) SEM Snapshots show an amino-functionalized CNFs specimen undergoing deformation and failure under a tensile test at (1) t=0, (2) t=20, (3) t=40, (4) t=60s.

Next, fracture modes of the CNFs were studied by high resolution SEM imaging of the fracture surfaces. The close up views of fracture specimens of the pristine (Figure 5.8(a)), fluorinated (Figure 5.8(b)) and amino-functionalized (Figure 5.8(c)) CNFs demonstrate that all three types of fiber failed in the similar cup-and-cone fashion reported earlier[132, 144, 145]. Suzuki observed the cup-shaped morphology in the fractured ends of the CNFs, and he claimed that the relatively weak interlayer bonding was responsible for the observed breakdown[144]. Brown *et al.* applied about 5% strain on fibers made of CNTs within amorphous carbon resulted in a permanent damage to its outer shells, giving rise to the plastic deformation until the outer shell eventually fractured and the inner layers nearly pulled out[145]. In this study, due to the turbostratic nature of CNFs walls, it is hypothesized that fracture begins in the outer layers where carbon structure is more disordered. Therefore, failure could initiate in the outer fiber layers with subsequent sliding of the inner graphitic layers, leading to the complete final fracture of the whole fiber.

The fine details of the cone structures in the pristine, fluorinated and amino-functionalized CNFs were further revealed by HRTEM images (Figure 5.9). It was found that the diameter of the hollow core remained unchanged in the cone section for the pristine (Figure 5.9(a)) and amino-functionalized (Figure 5.9(c)) CNFs, compared to the

fiber section without broken out layers further away from the fracture surface. Surprisingly, such well-expected morphology changed drastically in the fluorinated CNFs, where the diameter of the hollow core in the cone section expanded almost 5 times as compared to the hollow core diameter in the fiber section away from the fracture surface (Figure 5.9(b)). Also apparent from the insets of these HRTEM images, the inner carbon layers of all CNFs appeared to be more ordered as clearly shown in the magnified view of layer structures in the cone sections (Figure 5.9 insets).

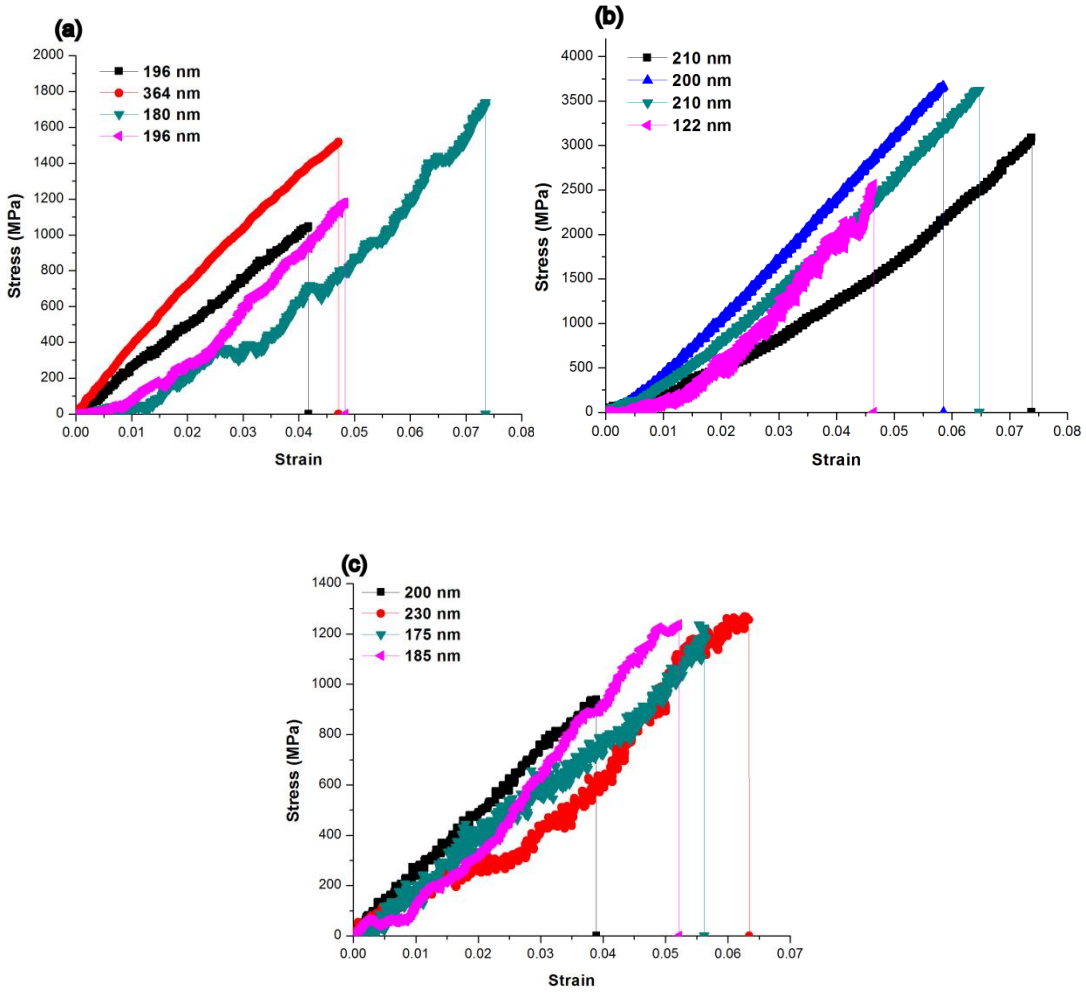

Figure 5.7 (a) selected tensile test engineering stress versus strain curves for pristine CNFs samples, (b) selected tensile test engineering stress versus strain curves for

fluorinated CNFs samples, (c) selected tensile test engineering stress versus strain curves for amino-functionalized CNFs samples.

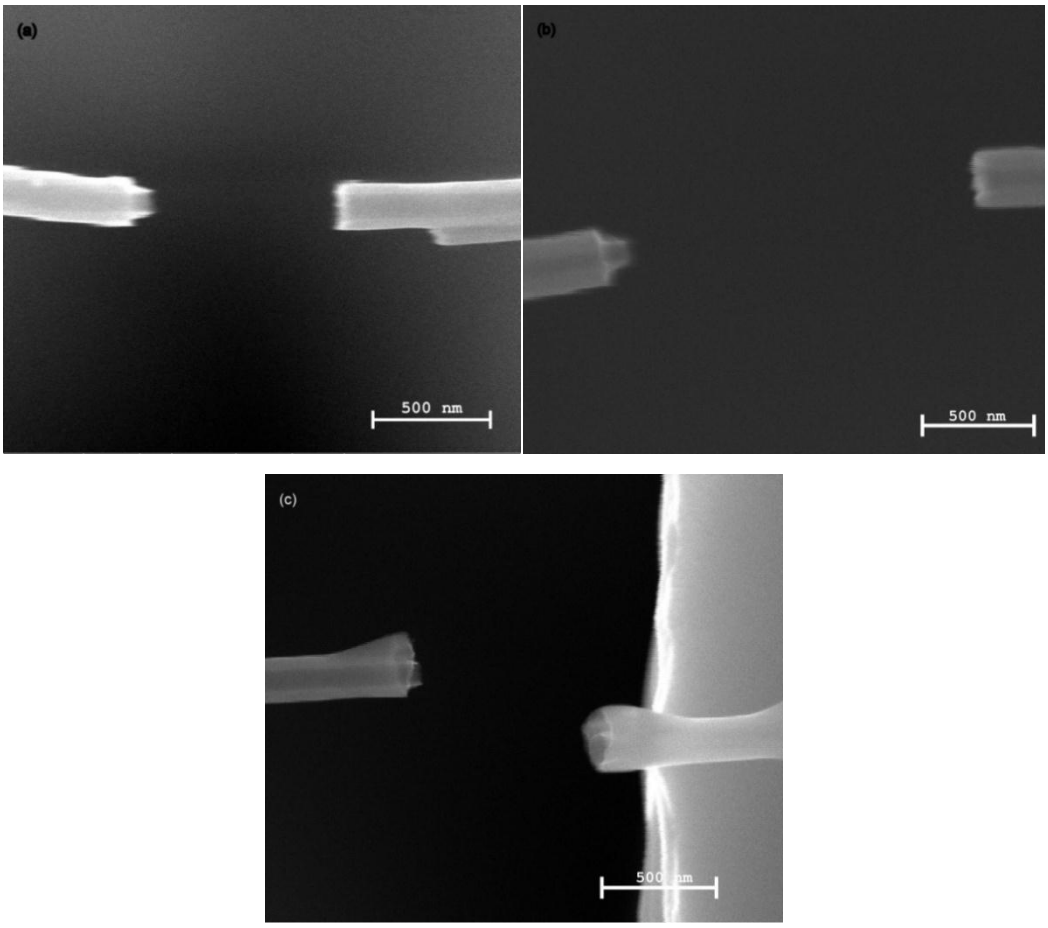

Figure 5.8 Representative SEM images of ruptured surfaces of (a) Pristine CNFs, (b) Fluorinated CNFs (c) Amino-functionalized CNFs.

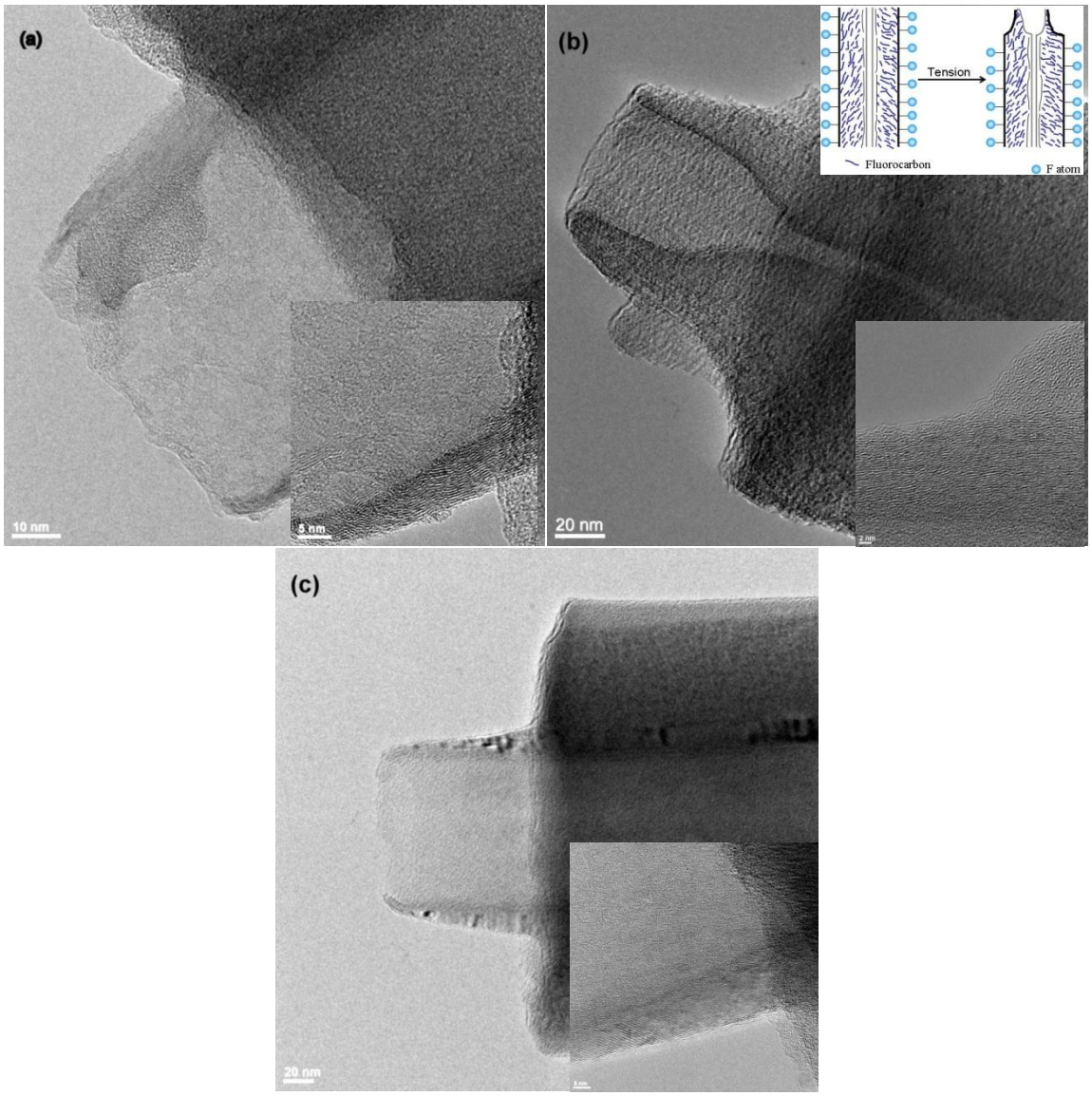

Figure 5.9 (a) HRTEM image of the pristine CNF fracture surface. The diameter of the hollow core kept the same in both cone and intact fiber sections after failure, the inset in bottom right corner showed more ordered inner layers of the pristine CNF. (b) HRTEM images of the fluorinated CNF fracture surface clearly showing the dramatic change of hollow core diameter from the cone to intact fiber section. The top inset showed a schematic illustration of the hollow core diameter change before and after fluorinated CNF fracture and the bottom inset showed more ordered inner layers of the fluorinated CNF. (c) HRTEM images of the amino-functionalized CNF fracture surface. The diameter of hollow core kept the same after failure in cone and intact fiber sections, the inset showed more ordered inner layers of the amino-functionalized CNF.

In order to better understand these intriguing fracture processes in CNFs with different chemical functionalization treatments, we need to first carefully evaluate the resulting structures of these functionalized CNFs. A simple schematic illustration of the complete fluorination and amination processes of CNFs is shown in (Scheme 5.1) to facilitate our understandings. For better illustration of the fluorinated CNFs structure, the distance between the fluorine atoms and fiber surface are exaggerated while the bold segments represent the fluorocarbons layers. During the fluorination process, previous XPS studies have shown that most of the fluorine atoms are expected to bond covalently on CNFs' outer layers. It should be noted that the hollow core can shrink due to the repulsive interaction of thicker fluorocarbons layers which is mostly directed inward. Such phenomenon has already been reported by Liu *et al*. where a similar fluorination method was used for the treatment of carbon nano-onions[146]. It was found that the fluorination process disrupted the integrity of the graphene layers in the onions by formation of fluorographene segments which compressed their interior structure, while the subsequent de-fluorination of carbon nano-onions by hydrazine treatment resulted in remarkable "healing" of broken graphene layers which recovered the original inner structure. In our case, it is believed that the diameter of the hollow core has been mostly recovered after defluorination and grafting of ethylenediamion groups predominantly to the CNFs surfaces as shown in Scheme 5.1.

Therefore, a possible scenario was proposed that the compressive force could be introduced on CNFs surfaces during the fluorination owing to the repulsive interactions of outer fluorocarbon layers, which could not only lead to a smaller hollow core diameter but also positively improve the nominal mechanical strength of the fluorinated CNFs. In

fact, such improvements were indeed observed in both average strength and Weibull characteristic strength values of fluorinated CNFs (Table 5.1). When the failure initiated at the less ordered outer layers as discussed earlier and then grew inward, the cup-and-cone type of fracture would develop facilitated by the relative sliding of more ordered inner layers with respect to the outer layers. Once the fluorinated CNFs fractured, the break-off of the outer layers in the cone side of the fracture surface would release the compressive force causing an abrupt hollow core expansion as observed in Figure 5.9(b). In the subsequent amino-functionalization procedures, the fluorination induced compressive force on CNFs surfaces was mostly released due to the de-fluorination process while further grafting of amino functional groups had minimum impact on CNFs hollow core size, promoting the recovery of hollow core size for amino-functionalized CNFs. This change was reflected by the similar fracture surface features (Figure 5.9(a) and (c)) and the average strength in the similar level (Table 5.1), although the strength of amino-functionalized CNFs was slightly lower due to the inevitable disruption of the CNFs surfaces and introduction of additional defects during the functionalization procedures.

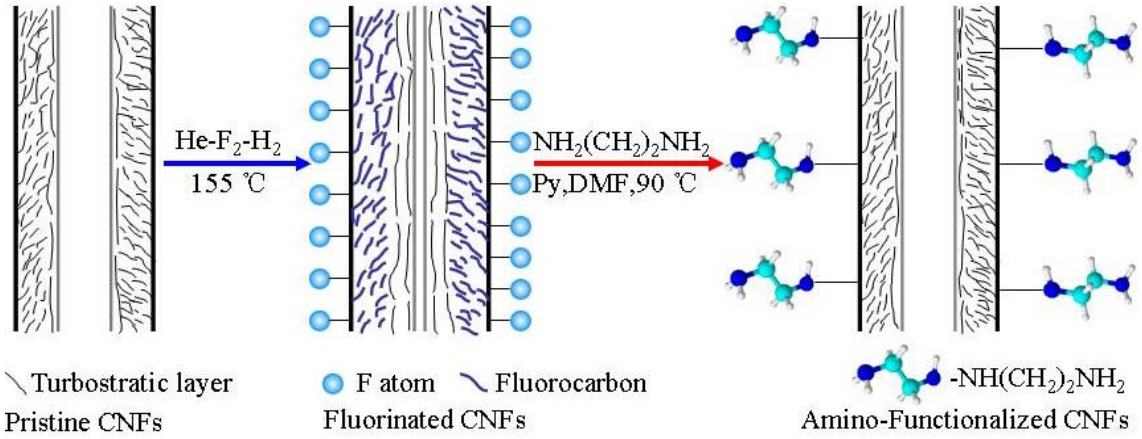

Scheme 5.1 Schematic illustration of the complete functionalization process for CNFs, note that the hollow core shrinks after fluorination and recovers after defluorination associated with amino-functionalization.

5.2. Conclusion

Successful fluorination and amination of CNFs were first achieved and systematic chemical characterizations of functionalized CNFs were performed. An *in situ* tensile testing method, which combined a simple micro-fabricated device with a quantitative nanoindenter inside a scanning electron microscope (SEM) chamber, was subsequently employed to measure mechanical properties of individual pristine, fluorinated and amino-functionalized CNFs. The nominal CNFs strengths followed the Weibull distribution with characteristic strengths between 1.94 and 3.05 GPa, and the fluorinated CNFs were found to possess higher nominal strength but similar strain compared with the pristine as well as the amino-functionalized CNFs. The relatively small Weibull moduli indicated a broad spectrum of flaws induced during functionalization for fluorinated and amino-treated CNFs. Further, SEM fracture surfaces analysis showed that all nanofibers failed in a similar cup-and-cone fashion. High resolution transmission electron microscope (HRTEM) of fluorinated CNFs revealed an unexpected change of the inner chamber before and after fiber fracture, which was attributed to the possible effects of fluorination-induced compression on nanofiber surfaces. The results demonstrated the potential of fluorination on improving both the mechanical properties of CNFs and their successful integration into composites.

Chapter 6

6.Concluding Remarks

6.1. Conclusion

The adhesion and tribological behaviors of aligned carbon nanotube arrays with different orientations and graphene nanoribbons with distinct functional groups were quantified using AFM/LFM under controlled environments. It was found that the adhesion forces on a transversely aligned CNTs surface are lower than those on a vertically aligned CNTs surface; the trend shows that the adhesion forces drop as the relative humidity decreases. Similarly, the friction forces are lower for transversely aligned CNTs side than for vertically aligned CNTs side in all above environments. The friction force was found to be critically influenced by the relative humidity; with decreasing relative humidity the friction force drops. For three types of chemically treated GNRs, measurements in both ambient and low humidity conditions demonstrate that covalently bonded functional groups have a significant impact on the frictional

response of GNRs. The measured tip-sample adhesion forces seem to support the observed friction force dependence on functionalizations, and the friction and adhesion differences could also be attributed to the surface reactivity and hydrophilicity differences induced by different chemical functionalization schemes.

We have developed a Peierls-type mechanistic study to elucidate the atomic frictional behavior from the initiation and spatiotemporal evolution of interface defects and lattice slip. Particularly, we found the temperature- and velocity-dependence of frictional behavior from the connection between activation energy calculations and spatially nonuniform rate-limiting process. The tunable friction force between two kindred materials, CVD grown graphene and HOPG, was realized by altering the relative rotation angle. We identified two narrow angular regions with high friction, separated by a wide angular interval with low friction. The distance between the two friction peaks is 61◦, which corresponds well with the 60◦ symmetry of individual atomic layers in the graphite lattice.

In addition, the development and application of a novel technique for mechanical characterization of nanomaterials and interfaces within an electron microscope was described in detail. The devices were first used to perform single MWNTs pullout experiments within a scanning electron microscope, in order to study the nature of adhesion at the MWNTs/polymer derived ceramics nanocomposite interface. The results of the pullout experiments showed that the interfacial strength (and toughness) of the pristine MWNTs/PDC interface was considerably higher than for conventional engineering composite systems. The calculated fracture energy release rate is in the range

of 5-44 J/m^2. The technique was subsequently used for the *in situ* quantitative tensile testing of individual functionalized carbon nanofibers. The nominal CNFs strengths follow the Weibull distribution with characteristic strengths between 1.94~3.05 GPa, and the fluorinated CNFs are found to possess higher nominal strength but similar strain compared with the pristine as well as the amino-functionalized CNFs. The relatively small Weibull moduli reflect a broad spectrum of flaws induced during functionalization for fluorinated and amino-treated CNFs. Further, SEM fracture surfaces analysis show that all nanofibers failed in a similar cup-and-cone fashion. HRTEM) image of fluorinated CNFs reveals an unexpected change of the hollow core before and after fiber fracture, which is attributed to the possible effects of fluorination-induced compression on nanofiber surfaces.

Even though there exists more than a decade's worth of research pertaining to the mechanical properties of CNTs/CNFs and the interfacial properties and related load transfer mechanisms in CNTs/CNFs reinforced nanocomposites, our ability to engineer CNTs/CNFs based structural composites to achieve the desired properties still remains rather limited. The novel technique described in this dissertation was developed in order to alleviate the issues of solid understanding of CNTs/CNFs deformation and interfacial processes. Look forward, the author envisions the technique being used as a robust tool for studying novel reinforcement materials and for interface tailoring.

Related Publications

1. L. Zhang, T. Petit, K. E. Peyer, B. E. Kratochvil, J. Zhang, J. Lou and B. Nelson. "Noncontact and Contact Micromanipulation Using a Rotating Nickel Nanowire", Proceedings of the 2010 IEEE International Conference on Nano/Molecular Medicine and Engineering, 2010, 38-43.

2. H. Lu*, J. Zhang* and J. Lou. "Localized Quantitative Characterization of Chemical Functionalization Effects on Adhesion Properties of SWNT", Journal of Nanomaterials, 2011, 1-5. (*Equally Contributed)

3. Z. Liu, L. Song, S. Zhao, J. Huang, L. Ma, J. Zhang, J. Lou and P. Ajayan. "Direct Growth of Graphene/Hexagonal Boron Nitride Stacked Layers", Nanoletters, 2011, 11, 2032-2037.

4. J. Zhang, P. Loya, C. Peng, V. Khabashesku and J. Lou. "Quantitative *In-situ* Mechanical Characterization of Effects of Chemical Functionalization on Individual Carbon Nanofibers", Advanced Functional Materials, 2012.

5. J. Zhang, W. Lu, J. M. Tour and J. Lou. " Nanoscale frictional characteristics of graphene nanoribbons", Applied Physics Letters, 101, 2012, 123104.

6. J. Zhang, Y. Zhang, N. Mara, L. Nicola and J. Lou. "Nanoimprinting of single crystalline gold: experiments and dislocation dynamics simulations", International Journal of Plasticity, under review.

7. A. Kessman, J. Zhang, J. Lou and B. Sheldon. “Carbon Nanotube Pullout and Toughness in Ceramic Nanocomposites”, in preparation.

8. J. Ma, J. Zhang, J. Lou and Q. Li. “Colloidal Particle Adhesion on Micro-patterned Surface”, in preparation.

References

[1] Chen, M. S. and Goodman, D. W."The Structure of Catalytically Active Gold on Titania", Science. (2004) 306,252-255

[2] Kim, S.-W., et al."Fabrication of Hollow Palladium Spheres and Their Successful Application to the Recyclable Heterogeneous Catalyst for Suzuki Coupling Reactions", Journal of the American Chemical Society. (2002) 124,7642-7643

[3] Valden, M., et al."Onset of Catalytic Activity of Gold Clusters on Titania with the Appearance of Nonmetallic Properties", Science. (1998) 281,1647-1650

[4] Zhou, S., et al."Enhanced CO Tolerance for Hydrogen Activation in Au−Pt Dendritic Heteroaggregate Nanostructures", Journal of the American Chemical Society. (2006) 128,1780-1781

[5] Cao, Y. C., et al."Nanoparticles with Raman Spectroscopic Fingerprints for DNA and RNA Detection", Science. (2002) 297,1536-1540

[6] Elghanian, R., et al."Selective Colorimetric Detection of Polynucleotides Based on the Distance-Dependent Optical Properties of Gold Nanoparticles", Science. (1997) 277,1078-1081

[7] Nie, S. and Emory, S. R."Probing Single Molecules and Single Nanoparticles by Surface-Enhanced Raman Scattering", Science. (1997) 275,1102-1106

[8] Ko, Y. H. and Yu, J. S."Urchin-aggregation inspired closely-packed hierarchical ZnO nanostructures for efficient light scattering", Opt. Express. (2011) 19,25935-25943

[9] Xia, L., et al."Naturally occurring nanoparticles from English ivy: an alternative to metal-based nanoparticles for UV protection", Journal of Nanobiotechnology. (2010) 8,12

[10] Iijima, S."Helical microtubules of graphitic carbon", Nature. (1991) 354,56-58

[11] Novoselov, K. S., et al."Electric Field Effect in Atomically Thin Carbon Films", Science. (2004) 306,666-669

[12] Novoselov, K. S., et al."Two-dimensional atomic crystals", Proceedings of the National Academy of Sciences of the United States of America. (2005) 102,10451-10453

[13] Dean, C. R., et al."Boron nitride substrates for high-quality graphene electronics", Nat Nano. (2010) 5,722-726

[14] Shao, Y., et al."Graphene Based Electrochemical Sensors and Biosensors: A Review", Electroanalysis. (2010) 22,1027-1036

[15] Liang, X., et al."Graphene Transistors Fabricated via Transfer-Printing In Device Active-Areas on Large Wafer", Nano Letters. (2007) 7,3840-3844

[16] Anton, N. S., et al."Electrostatic deposition of graphene", Nanotechnology. (2007) 18,135301

[17] Reina, A., et al."Large Area, Few-Layer Graphene Films on Arbitrary Substrates by Chemical Vapor Deposition", Nano Letters. (2008) 9,30-35

[18] Moreau, E., et al."Graphene growth by molecular beam epitaxy using a solid carbon source", physica status solidi (a). (2010) 207,300-303

[19] Roduner, E."Size matters: why nanomaterials are different", Chemical Society Reviews. (2006) 35,583-592

[20] Yu-Sheng, H., et al."Morphological control of CuPc and its application in organic solar cells", Nanotechnology. (2008) 19,415603

[21] Nurislamova, G., et al."Nanostructure and related mechanical properties of an Al–Mg–Si alloy processed by severe plastic deformation", Philosophical Magazine Letters. (2008) 88,459-466

[22] Tabor, D. and Winterton, R. H. S."Surface Forces: Direct Measurement of Normal and Retarded van der Waals Forces", Nature. (1968) 219,1120-1121

[23] Krim, J., et al."Nanotribology of a Kr monolayer: A quartz-crystal microbalance study of atomic-scale friction", Physical Review Letters. (1991) 66,181-184

[24] Hertz, H., *Miscellaneous Papers by H. Hertz, ed.* (Macmillian, London, 1896).

[25] Bradley, R. S."The Cohesive Force Between Solide Surfaces and the Surface Energy of Solids", Philosophical Magazine. (1932) 31, 853-862

[26] Johnson, K. L., et al." Surface energy and the contact of elastic solids", Proceedings of the Royal Society of London. (1971) A324,301-313

[27] Derjaguin, B. V., et al."Effect of Contact Deformations on the Adhesion of Particles", Journal of Colloid and Interface Science. (1975) 53,314-326

[28] Tomlinson, G. A."A molecular theory of friction ", Philosophical Magazine. (1929) 7,905-939

[29] Zhong, W. and Tománek, D."First-principles theory of atomic-scale friction", Physical Review Letters. (1990) 64,3054-3057

[30] Hirano, M., et al."Observation of Superlubricity by Scanning Tunneling Microscopy", Physical Review Letters. (1997) 78,1448-1451

[31] Socoliuc, A., et al."Atomic-Scale Control of Friction by Actuation of Nanometer-Sized Contacts", Science. (2006) 313,207-210

[32] Hirata, A. and Yoshioka, N."Sliding friction properties of carbon nanotube coatings deposited by microwave plasma chemical vapor deposition", Tribology International. (2004) 37,893-898

[33] Tu, J. P., et al."Synthesis and frictional properties of array film of amorphous carbon nanofibers on anodic aluminum oxide", Carbon. (2003) 41,1257-1263

[34] Yakobson, B. I."Mechanical relaxation and ``intramolecular plasticity'' in carbon nanotubes", Applied Physics Letters. (1998) 72,918-920

[35] Ramirez, F. and Carlsson, L."Modified single fiber fragmentation test procedure to study water degradation of the fiber/matrix interface toughness of glass/vinylester", Journal of Materials Science. (2009) 44,3035-3042

[36] Hampe, A., et al."An advanced equipment for single-fibre pull-out test designed to monitor the fracture process", Composites. (1995) 26,40-46

[37] Zidi, M., et al."Quantitative analysis of the micro-indentation behaviour of fibre-reinforced composites: development and validation of an analytical model", Composites Science and Technology. (2000) 60,429-437

[38] Dervishi, E., et al."Carbon Nanotubes: Synthesis, Properties, and Applications", Particulate Science and Technology. (2009) 27,107-125

[39] Ajayan, P. M., et al."Single-Walled Carbon Nanotube–Polymer Composites: Strength and Weakness", Advanced Materials. (2000) 12,750-753

[40] Ni, B. and Sinnott, S. B."Tribological properties of carbon nanotube bundles predicted from atomistic simulations", Surface Science. (2001) 487,87-96

[41] Kinoshita, H., et al."High friction of a vertically aligned carbon-nanotube film in microtribology", Applied Physics Letters. (2004) 85,2780-2781

[42] Dickrell, P. L., et al."Frictional anisotropy of oriented carbon nanotube surfaces", Tribology Letters. (2005) 18,59-62

[43] Dickrell, P. L., et al."Tunable friction behavior of oriented carbon nanotube films", Tribology Letters. (2006) 24,85-90

[44] Lou, J. and Kim, K. S."Effects of interfaces on nano-friction of vertically aligned multi-walled carbon nanotube arrays", Materials Science and Engineering: A. (2008) 483–484,664-667

[45] Schall, J. D. and Brenner, D. W."Molecular Dynamics Simulations of Carbon Nanotube Rolling and Sliding on Graphite", Molecular Simulation. (2000) 25,73-79

[46] Falvo, M. R., et al."Gearlike rolling motion mediated by commensurate contact: Carbon nanotubes on HOPG", Physical Review B. (2000) 62,R10665-R10667

[47] Falvo, M. R., et al."Nanometre-scale rolling and sliding of carbon nanotubes", Nature. (1999) 397,236-238

[48] Suekane, O., et al."Static Friction Force of Carbon Nanotube Surfaces", Applied Physics Express. (2008) 1,1-3

[49] Heremans, J., et al."Magnetic susceptibility of carbon structures", Physical Review B. (1994) 49,15122-15125

[50] Langer, L., et al."Quantum Transport in a Multiwalled Carbon Nanotube", Physical Review Letters. (1996) 76,479-482

[51] Treacy, M. M. J., et al."Exceptionally high Young's modulus observed for individual carbon nanotubes", Nature. (1996) 381,678-680

[52] Schadler, L. S., et al."Load transfer in carbon nanotube epoxy composites", Applied Physics Letters. (1998) 73,3842-3844

[53] Ganesan, Y. and Lou, J."The mechanical characterization of carbon-nanotube-reinforced polymer-matrix nanocomposites: An unfolding story of interface", JOM Journal of the Minerals, Metals and Materials Society. (2009) 61,32-37

[54] Ler, J. G. Q., et al."Effect of sidewall modification in the determination of friction coefficient of vertically aligned carbon nanotube films using friction force microscopy", Carbon. (2007) 45,2737-2743

[55] Ohmae, N."Humidity effects on tribology of advanced carbon materials", Tribology International. (2006) 39,1497-1502

[56] Turq, V., et al."Influence of humidity on microtribology of vertically aligned carbon nanotube film", Tribology Letters. (2005) 19,23-28

[57] Bowden, F. P. and Tabor, D., *The friction and lubrication of solids*, 1st ed. (Oxford University press, Oxford, 1950), p.67.

[58] Weisenhorn, A. L., et al."Measuring adhesion, attraction, and repulsion between surfaces in liquids with an atomic-force microscope", Physical Review B. (1992) 45,11226-11232

[59] Owens, D. K. and Wendt, R. C."Estimation of the surface free energy of polymers", Journal of Applied Polymer Science. (1969) 13,1741-1747

[60] Geim, A. K. and Novoselov, K. S."The rise of graphene", Nat Mater. (2007) 6,183-191

[61] Morozov, S. V., et al."Giant Intrinsic Carrier Mobilities in Graphene and Its Bilayer", Physical Review Letters. (2008) 100,016602

[62] Calizo, I., et al."Variable temperature Raman microscopy as a nanometrology tool for graphene layers and graphene-based devices", Applied Physics Letters. (2007) 91,071913-071913

[63] Semenoff, G. W."Condensed-Matter Simulation of a Three-Dimensional Anomaly", Physical Review Letters. (1984) 53,2449-2452

[64] Shin, Y.-S., et al."High-Mobility Graphene Nanoribbons Prepared Using Polystyrene Dip-Pen Nanolithography", Journal of the American Chemical Society. (2011) 133,5623-5625

[65] Murali, R., et al."Resistivity of Graphene Nanoribbon Interconnects", Electron Device Letters, IEEE. (2009) 30,611-613

[66] Lee, C., et al."Measurement of the Elastic Properties and Intrinsic Strength of Monolayer Graphene", Science. (2008) 321,385-388

[67] Han, M. Y., et al."Energy Band-Gap Engineering of Graphene Nanoribbons", Physical Review Letters. (2007) 98,206805

[68] Li, X., et al."Chemically Derived, Ultrasmooth Graphene Nanoribbon Semiconductors", Science. (2008) 319,1229-1232

[69] Kosynkin, D. V., et al."Longitudinal unzipping of carbon nanotubes to form graphene nanoribbons", Nature. (2009) 458,872-876

[70] Jiao, L., et al."Narrow graphene nanoribbons from carbon nanotubes", Nature. (2009) 458,877-880

[71] Rafiee, M. A., et al."Graphene Nanoribbon Composites", ACS Nano. (2010) 4,7415-7420

[72] Ricardo, F. and et al."Mechanical properties of graphene nanoribbons", Journal of Physics: Condensed Matter. (2009) 21,285304

[73] Kosynkin, D. V., et al."Highly Conductive Graphene Nanoribbons by Longitudinal Splitting of Carbon Nanotubes Using Potassium Vapor", ACS Nano. (2011) 5,968-974

[74] Zhu, Y., et al."Covalent Functionalization of Surfactant-Wrapped Graphene Nanoribbons", Chemistry of Materials. (2009) 21,5284-5291

[75] Higginbotham, A. L., et al."Lower-Defect Graphene Oxide Nanoribbons from Multiwalled Carbon Nanotubes", ACS Nano. (2010) 4,2059-2069

[76] Lu, H., et al."Friction and adhesion properties of vertically aligned multi-walled carbon nanotube arrays and fluoro-nanodiamond films", Carbon. (2008) 46,1294-1301

[77] Becerril, H. A., et al."Evaluation of Solution-Processed Reduced Graphene Oxide Films as Transparent Conductors", ACS Nano. (2008) 2,463-470

[78] Gates, R. S. and Reitsma, M. G."Precise atomic force microscope cantilever spring constant calibration using a reference cantilever array", Review of Scientific Instruments. (2007) 78,086101-086103

[79] Landolsi, F., et al."Regular and reverse nanoscale stick-slip behavior: Modeling and experiments", Applied Surface Science. (2010) 256,2577-2582

[80] Lee, C., et al."Frictional Characteristics of Atomically Thin Sheets", Science. (2010) 328,76-80

[81] Buzio, R., et al."Friction force microscopy investigation of nanostructured carbon films", Carbon. (2002) 40,883-890

[82] Ou, J., et al."Tribology Study of Reduced Graphene Oxide Sheets on Silicon Substrate Synthesized via Covalent Assembly", Langmuir. (2010) 26,15830-15836

[83] Frisbie, C. D., et al."Functional Group Imaging by Chemical Force Microscopy", Science. (1994) 265,2071-2074

[84] Noy, A., et al."Chemical Force Microscopy: Exploiting Chemically-Modified Tips To Quantify Adhesion, Friction, and Functional Group Distributions in Molecular Assemblies", Journal of the American Chemical Society. (1995) 117,7943-7951

[85] Poggi, M. A., et al."Measuring the Adhesion Forces between Alkanethiol-Modified AFM Cantilevers and Single Walled Carbon Nanotubes", Nano Letters. (2003) 4,61-64

[86] Lu, H., et al."Localized Quantitative Characterization of Chemical Functionalization Effects on Adhesion Properties of SWNT", Journal of Nanomaterials. (2011) 2011,

[87] Sumant, A. V., et al."Surface chemistry and bonding configuration of ultrananocrystalline diamond surfaces and their effects on nanotribological properties", Physical Review B. (2007) 76,235429

[88] Carpick, R. W. and Salmeron, M."Scratching the Surface: Fundamental Investigations of Tribology with Atomic Force Microscopy", Chemical Reviews. (1997) 97,1163-1194

[89] Hölscher, H., et al."Principles of atomic friction: from sticking atoms to superlubric sliding", Philosophical Transactions of the Royal Society A: Mathematical, Physical and Engineering Sciences. (2008) 366,1383-1404

[90] Izabela, S., et al."Recent advances in single-asperity nanotribology", Journal of Physics D: Applied Physics. (2008) 41,123001

[91] Socoliuc, A., et al."Transition from Stick-Slip to Continuous Sliding in Atomic Friction: Entering a New Regime of Ultralow Friction", Physical Review Letters. (2004) 92,134301

[92] Gao, Y."A Peierls perspective on mechanisms of atomicfriction", Journal of the Mechanics and Physics of Solids. (2010) 58,2023-2032

[93] Gnecco, E., et al."Velocity Dependence of Atomic Friction", Physical Review Letters. (2000) 84,1172-1175

[94] Sang, Y., et al."Thermal Effects on Atomic Friction", Physical Review Letters. (2001) 87,174301

[95] Riedo, E., et al."Interaction Potential and Hopping Dynamics Governing Sliding Friction", Physical Review Letters. (2003) 91,084502

[96] Zhao, X., et al."Transition from Thermal to Athermal Friction under Cryogenic Conditions", Physical Review Letters. (2009) 102,186102

[97] Tortonese, M. and Kirk, M."Characterization of application-specific probes for SPMs", (1997) 53-60

[98] Li, Q., et al."Lateral force calibration of an atomic force microscope with a diamagnetic levitation spring system", Review of Scientific Instruments. (2006) 77,065105-065113

[99] Rice, J. R. and Beltz, G. E."The activation energy for dislocation nucleation at a crack", Journal of the Mechanics and Physics of Solids. (1994) 42,333-360

[100] Lee, J. H. and Gao, Y."Mixed-mode singularity and temperature effects on dislocation nucleation in strained interconnects", International Journal of Solids and Structures. (2011) 48,1180-1190

[101] Thomas, P., et al."Tribological properties of low-temperature graphite fluorides. Influence of the structure on the lubricating performances", Journal of Physics and Chemistry of Solids. (2006) 67,1095-1099

[102] Chen, Y., et al."Graphene and its derivatives: switching ON and OFF", Chemical Society Reviews. (2012) 41,4688-4707

[103] Gosvami, N., et al."Microscopic Friction Studies on Metal Surfaces", Tribology Letters. (2010) 39,19-24

[104] Greiner, C., et al."Controlling Nanoscale Friction through the Competition between Capillary Adsorption and Thermally Activated Sliding", ACS Nano. (2012) 6,4305-4313

[105] Jinesh, K. B., et al."Thermolubricity in atomic-scale friction", Physical Review B. (2008) 78,155440

[106] Aubry, S."The twist map, the extended Frenkel-Kontorova model and the devil's staircase", Physica D: Nonlinear Phenomena. (1983) 7,240-258

[107] Mate, C. M., et al."Atomic-scale friction of a tungsten tip on a graphite surface", Physical Review Letters. (1987) 59,1942-1945

[108] Dienwiebel, M., et al."Superlubricity of Graphite", Physical Review Letters. (2004) 92,126101

[109] Wang, R., et al."Large-Diameter Graphene Nanotubes Synthesized Using Ni Nanowire Templates", Nano Letters. (2010) 10,4844-4850

[110] Ekşiog˘lu, B. and Nadarajah, A."Structural analysis of conical carbon nanofibers", Carbon. (2006) 44,360-373

[111] Cha, S. I., et al."Strengthening and toughening of carbon nanotube reinforced alumina nanocomposite fabricated by molecular level mixing process", Scripta Materialia. (2005) 53,793-797

[112] Maensiri, S., et al."Carbon nanofiber-reinforced alumina nanocomposites: Fabrication and mechanical properties", Materials Science and Engineering: A. (2007) 447,44-50

[113] Kothari, A. K., et al."Comparison Between Carbon Nanotube and Carbon Nanofiber Reinforcements in Amorphous Silicon Nitride Coatings", Journal of the American Ceramic Society. (2008) 91,2743-2746

[114] Peigney, A."Composite materials: Tougher ceramics with nanotubes", Nat Mater. (2003) 2,15-16

[115] Sheldon, B. W. and Curtin, W. A."Nanoceramic composites: Tough to test", Nat Mater. (2004) 3,505-506

[116] Yamamoto, G., et al."Nanotube fracture during the failure of carbon nanotube/alumina composites", Carbon. (2011) 49,3709-3716

[117] Evans, A. G."Perspective on the Development of High-Toughness Ceramics", Journal of the American Ceramic Society. (1990) 73,187-206

[118] Xia, Z., et al."Direct observation of toughening mechanisms in carbon nanotube ceramic matrix composites", Acta Materialia. (2004) 52,931-944

[119] Li, L., et al."Molecular Dynamics Simulations of Interfacial Sliding in Carbon-Nanotube/Diamond Nanocomposites", Journal of the American Ceramic Society. (2009) 92,2331-2336

[120] Jiang, K. R. and Penn, L. S."Improved analysis and experimental evaluation of the single filament pull-out test", Composites Science and Technology. (1992) 45,89-103

[121] Ganesan, Y., et al."Interface Toughness of Carbon Nanotube Reinforced Epoxy Composites", ACS Applied Materials & Interfaces. (2011) 3,129-134

[122] Galiotis, C."Interfacial studies on model composites by laser Raman spectroscopy", Composites Science and Technology. (1991) 42,125-150

[123] Detassis, M., et al."Interface toughness in fibre composites by the fragmentation test", Composites Part A: Applied Science and Manufacturing. (1996) 27,769-773

[124] Barber, A. H., et al."Interfacial fracture energy measurements for multi-walled carbon nanotubes pulled from a polymer matrix", Composites Science and Technology. (2004) 64,2283-2289

[125] Lawrence, J., et al."Structural transformation of vapor grown carbon nanofibers studied by HRTEM", Journal of Nanoparticle Research. (2008) 10,1155-1167

[126] Wei, C."Nanomechanics of carbon nanofibers: Structural and elastic properties", Appl. Phys. Lett. (2004) 85,2208

[127] Kim, G.-T., et al."Simple method to prepare individual suspended nanofibers", Applied Physics Letters. (2002) 80,1815-1817

[128] Lawrence, J. G., et al."Elastic Properties and Morphology of Individual Carbon Nanofibers", ACS Nano. (2008) 2,1230-1236

[129] Zhang, H., et al."High tensile modulus of carbon nanotube nano-fibers produced by dielectrophoresis", Chemical Physics Letters. (2009) 478,230-233

[130] Zussman, E., et al."Mechanical and structural characterization of electrospun PAN-derived carbon nanofibers", Carbon. (2005) 43,2175-2185

[131] Inaba, K., et al."Determination of Young's modulus of carbon nanofiber probes fabricated by the argon ion bombardment of carbon coated silicon cantilever", Carbon. (2011) 49,4191-4196

[132] Ozkan, T., et al."Mechanical properties of vapor grown carbon nanofibers", Carbon. (2010) 48,239-244

[133] Arshad, S. N., et al."Strong carbon nanofibers from electrospun polyacrylonitrile", Carbon. (2011) 49,1710-1719

[134] Zhou, Z., et al."Development of carbon nanofibers from aligned electrospun polyacrylonitrile nanofiber bundles and characterization of their microstructural, electrical, and mechanical properties", Polymer. (2009) 50,2999-3006

[135] Khabashesku, V. N., et al."Fluorination of Single-Wall Carbon Nanotubes and Subsequent Derivatization Reactions", Accounts of Chemical Research. (2002) 35,1087-1095

[136] Khabashesku, V. N. and Pulikkathara, M. X."Chemical modification of carbon nanotubes", Mendeleev Communications. (2006) 16,61-66

[137] Pan, C. and Bao, Q."Well-aligned carbon nanotubes from ethanol flame", Journal of Materials Science Letters. (2002) 21,1927-1929

[138] Ganesan, Y., et al."Development and Application of a Novel Microfabricated Device for the In Situ Tensile Testing of 1-D Nanomaterials", Microelectromechanical Systems, Journal of. (2010) 19,675-682

[139] Lu, Y., et al."A Multi-step Method for <i>In Situ</i> Mechanical Characterization of 1-D Nanostructures Using a Novel Micromechanical Device", Experimental Mechanics. (2010) 50,47-54

[140] Ganesan, Y., et al."Effect of Nitrogen Doping on the Mechanical Properties of Carbon Nanotubes", ACS Nano. (2010) 4,7637-7643

[141] Lu, Y., et al."Cold welding of ultrathin gold nanowires", Nat Nano. (2010) 5,218-224

[142] Endo, M., et al."Vapor-grown carbon fibers (VGCFs): Basic properties and their battery applications", Carbon. (2001) 39,1287-1297

[143] Mangonon, P., *The principles of materials selection for engineering design.*, 1st ed. (PrenticeHall, Upper Saddle River, NJ, 1999).

[144] Suzuki, M."Current-induced breakdown of carbon nanofibers", J. Appl. Phys. (2007) 101,114307

[145] Brown, J. J., et al."Microsystem for nanofiber electromechanical measurements", Sensors and Actuators A: Physical. (2009) 155,1-7

[146] Liu, Y., et al."Functionalization of Carbon Nano-onions by Direct Fluorination", Chemistry of Materials. (2007) 19,778-786

[147] Buongiorno Nardelli, M., et al."Mechanical properties, defects and electronic behavior of carbon nanotubes", Carbon. (2000) 38,1703-1711

[148] Huang, J. Y., et al."Superplastic carbon nanotubes", Nature. (2006) 439,281-281

[149] Chang, C.-C., et al."A New Lower Limit for the Ultimate Breaking Strain of Carbon Nanotubes", ACS Nano. (2010) 4,5095-5100